Yielding, Relaxation, and Recovery in Amorphous Materials

LOCKWOOD, HAL

How to cite:

LOCKWOOD, HAL (2024) *Yielding, Relaxation, and Recovery in Amorphous Materials*, Durham theses, Durham University. Available at Durham E-Theses Online: http://etheses.dur.ac.uk/15429/

Yielding, Relaxation, and Recovery in Amorphous Materials

Henry Adin Lockwood

A Thesis presented for the degree of
Doctor of Philosophy

Durham
University

Department of Physics
Durham University
United Kingdom

March 2024

Yielding, Relaxation, and Recovery in Amorphous Materials

Henry Adin Lockwood

Submitted for the degree of Doctor of Philosophy

March 2024

Abstract: Amorphous materials span a wide range of systems, including foam bubbles, colloidal molecules, and polymer strands. Regardless of their composition, they all share the common feature of structural disorder. This results in universal flow behaviour. The yielding, relaxation and recovery of these systems are relevant to widespread processes, from spreading mayonnaise to flowing magma. Studying their behaviour under rheological shear protocols, by imposing loads and deformations of various forms, reveals fascinating phenomena that challenge the conventional notions of solid and liquid properties. Utilising theoretical mesoscopic models can help in understanding experimentally observed behaviours, and also predict new ones. The work in this thesis consists of three distinct studies into the material responses to imposed shear, and the exploration of their origins and consequences.

The first study researches the stress relaxation of an amorphous material after the imposition of a step strain within two mesoscopic models. The key finding is that a catastrophic shear instability can occur at a long delay time after the initial strain application, under conditions that might intuitively be presumed stable. This failure event is then studied in detail, by analysing its origins in the slow build-up of mesoscopic yield events leading to a shear localisation avalanche, and examining how the delay time before failure occurs depends on the relevant control parameters of the protocol and system.

Following that study, the yielding of an amorphous protein gel under the imposition of a step stress is simulated using a modification, newly introduced in this work, of an established model. More specifically, introducing permanent breaking of the mesoscopic substructures into the model replicates phenomena found experimentally, including the Basquin law of fatigue, Monkman-Grant relation, and three creep regimes. In addition, the study explores the precursors to failure under creep, and how the time of fluidisation can be influenced by the properties of the material and protocol.

The final study investigates the yielding, relaxation, and recovery of an amorphous material under the creep-recovery test protocol through mesoscopic simulation. The primary focus is on recoverable strain, where strain that arises during the stress application can be recovered after the stress is switched off. High levels of strain recovery are predicted, and its dependence on system parameters is explored. An important new discovery is that the recoverable strain in the model system is a result of plastic events, a phenomenon known as reversible plasticity.

Contents

Declaration

The work in this thesis is based on research carried out in the Department of Physics at Durham University. No part of this thesis has been submitted elsewhere for any degree or qualification.

Acknowledgements

Thanks must first go to my supervisor, Prof. Suzanne Fielding, for her scientific guidance throughout my PhD, and without whom none of the work in this thesis would have happened. I am also grateful to my second supervisor Prof. Halim Kusumaatmaja, and my industrial supervisor Dr. Andrew Clarke from Schlumberger Cambridge Research for useful discussions and insights. In addition, my sincere gratitude to all the Fielding group members over the years who have offered thoughts on my work. Finally, I would like to thank my wonderful friends and family, who have been endlessly patient, generous, and supportive.

We can't go over it.
We can't go under it.
We've got to go through it!

— from *We're Going on a Bear Hunt* by M. Rosen

Publications

Manuscripts under review:

H. A. Lockwood, E. S. Carrington and S. M. Fielding, *Ultra-delayed material failure via shear banding after straining an amorphous material.* arXiv preprint arXiv:2305.02144 (May, 2023).

H. A. Lockwood, M. Agar and S. M. Fielding, *Power law creep and delayed failure of gels and fibrous materials under stress.* arXiv preprint arXiv:2311.16778 (Nov, 2023).

Chapter 1

Introduction

Ketchup contained in an open glass bottle will remain so when inverted, and yet upon shaking will douse a meal with its full contents [1, 2]. A sloped region of hard clay soil can be built upon, but then suddenly fail and become a dangerous landslide [3, 4]. Epithelial tissue can form a solid protective layer on the outer surfaces of organs, but then quickly fluidise when cut to facilitate wound healing [5–7]. The remarkable ability of these materials to transition between apparently solid and liquid states is a consequence of their structural disorder, or amorphous nature [1, 5, 6, 8–12].

The study of these amorphous materials is a far-reaching topic of high importance in the modern day, with many reviews outlining the uses and applications of research in this area [8–11]. They appear in many commercial applications, from toothpaste to tarmac [9, 13–16]. Examples can also be found in nature, with geological materials such as magma [17], and in biological systems, such as in blood and collagen [5–7, 18–22]. Therefore, the range and impact of research in this area cannot be understated.

The class of amorphous materials is extremely broad. They range from dense particle suspensions [8, 23–25], to low density cross-linked structures with attractive interactions [26–33]. There are numerous subsets of amorphous materials, variously defined in the literature, such as elasto-plastic [9], visco-elastic [10], paste [34, 35] and yield stress materials [3, 11, 36–40]. There is variation even within amorphous material classes, such as between soft [6, 7, 20, 41–44] and metallic [45–49] glasses, or between micro-gels [36, 50, 51], hydrogels [52–55] and colloidal gels [56–59].

Depending on the imposed load, amorphous materials can display properties that are conventionally considered distinct solid and liquid properties, such as elastic deformation and viscous flow respectively [1,5,6,9,12]. This study of the deformation and flow of soft matter is called rheology [60, 61].

Studying the rheology of amorphous materials reveals the phenomenon of yielding, localised events within the system that function to relax the imposed load [8,9,49,62]. This yielding can be reversible, such as in soft dilute polymer [9, 10] or colloidal glass systems [6, 7, 20, 41–44, 62], or irreversible, such as in dense entangled polymer [9, 10, 22, 33, 63–69] or metallic glass systems [45–49]. It can also result in yielding transitions between solid-like and liquid-like behaviour [9,10,70]. One well established example is the occurrence of a stress overshoot, where a material under a constant rate of deformation experiences an initially solid-like response before a yielding transition under which the system fluidises [9, 11, 71].

Some amorphous materials require a certain minimum load to be able to experience a yielding transition, these are called yield stress materials [3, 11, 36–40]. The development of this yield stress is generally system dependent [11]. For example, in soft colloidal systems, increasing the particle density results in the glass transition, from a viscous suspension to an amorphous solid with glassy dynamics [11, 72]. A similar transition, the jamming transition, which depends on the packing fraction, involves hard particle systems [11, 73]. In polymeric systems, a change in concentration can transition a viscous dilute unentangled solution into a concentrated entangled gel [10]. The development of a yield stress can also occur with the introduction of new mediums. The liquid-like independent components of mayonnaise (egg yolk, oil, and vinegar) form a yield stress emulsion when mixed together [9, 74] and the aeration caused by whipping gas bubbles into cream, a viscous liquid, creates a yield stress material [11, 35, 75].

The details of these amorphous material systems, such as the chemical components, system structures, and thermal properties, can vary significantly. For example, entangled strand-like polymer systems [22, 33, 63–69] appear to be highly distinct from jammed suspensions of colloidal particles [62, 76–80]. However, recent research in this area has reached a remarkable consensus, that despite the variations in system details, there are several unifying features in the way that all amorphous materials behave, suggestive of a common underlying cause [9, 23, 81]. Each system's composition can be described in terms of mesoscopic substructures that, though not universal in size, all display structural disorder and metastability [25, 71, 81]. These substructures generally exist in configurations that are not the state of minimum free energy. However, in many systems the energy barriers to escape these configurations are too large to overcome through thermal motion, halting rearrangement to a state of complete structural relaxation. The material is therefore trapped in a non-equilibrium disordered metastable state [25, 51, 71, 82].

The unifying features of these amorphous materials result in universal physical properties. Particularly significant to the research featured in this thesis is the phenomenon of rheological ageing, which occurs in many amorphous materials [9, 11, 71, 81, 83]. This is where an initially liquid-like sample slowly evolves towards an ever more solid-like state as a function of the time since it was prepared [23]. Ageing can impact many rheological effects, including the occurrence of shear banding [11, 24, 84–86], one of the primary focuses of this thesis.

Shear banding is a heterogeneity in the flow profile of a fluid which takes the form of macroscopic bands of different viscosity within a planar shear cell [9, 25]. This heterogeneous shear-banded flow state often arises when aged materials are subject to an imposed shear flow. Evidence for these localised heterogeneous flows has been found theoretically in many complex fluids under various shear conditions [9,25,84,87–89]. Experimental evidence for shear banding can be found in gels, colloidal glasses, clay suspensions, carbopol microgels, and domestic products (ketchup, mustard, mayonnaise and hair gel) [3, 36–38]. It has also been suggested that landslides are a direct consequence of shear banding [3, 4]. Shear banding can cause systems under shear to fail, fluidise and fracture, which makes it an important phenomenon to study [8–11, 84–86, 90].

This thesis will describe the results of three distinct but related projects completed during the course of the author's PhD.

The first project, the results of which are discussed in Chapter 4, studies the response of an amorphous material to the step strain protocol, where a constant deformation is applied. This project builds upon work completed during the author's Masters project, which found that a catastrophic shear banding instability can arise in a soft glassy material at indefinitely long delay times [91]. This instability occurs even though the material is subjected to no further external deformation, following a sudden shear at a much earlier time. This prior work utilised the Soft Glassy Rheology (SGR) Model [13, 23–25, 71, 81, 92], which has been shown to capture a range of amorphous material rheological behaviour [9, 11, 13, 23, 25, 40, 71, 81, 93].

The work presented in Chapter 4 studies the same step strain protocol as previous work [91], but simulated using a Thermal Elasto-Plastic (TEP) model [9, 94–105], described in Section 2.3. It also expands on the previous work within the SGR model to study the effects of the amplitude of the imposed step strain and the working temperature on the time at which catastrophic banding occurs. Uncovering the predicted phenomenon of highly delayed catastrophic shear banding in two theoretical models, in addition to work by a collaborator on a third fluidity model [91], implies that it may be universal across amorphous materials. It is hoped that the strength of this theoretical prediction will stimulate experimentalists to test this conclusion.

The second project, the results of which are discussed in Chapter 5, modifies the SGR model to expand its influence beyond the 'soft glassy materials' it was originally intended to describe [13]. Disrupting the reformation of elements within the model simulates the process of strand breaking in low density attractive gels. This is reminiscent of behaviour seen in fibre bundle models [9, 106–109], which have had some success in simulating these gels [110]. By modelling a creep protocol that is well documented in the literature, this project aims to understand experimental fluidisation and failure behaviour and by doing so provide an accurate physical model for the simulation of these gels.

Creep is the response to the application of a constant load onto a material. The standard material response is to initially strain slowly, and at a slowing rate over time (hence, ‘creep’) [11,36,87]. In certain cases, creep can end in a sudden fluidisation, fracture or material failure [9,11,19,36,51,111,112]. The study of creep is widespread in the computational and experimental literature on amorphous materials [9, 11, 25, 28, 36, 81, 87, 107–109, 112–116]. Practical applications include studying yield stresses [11, 36, 87], material failure times [9, 107, 114], and even natural disasters such as earthquakes [98,113,117–119]. There are many examples of the effectiveness of mesoscopic models in simulating creep [98,111,117] including in the SGR model [25, 87]. The work in Chapter 5 builds on this success by introducing a new modification to the SGR model to more closely simulate the behaviour of protein gels under the creep protocol. In particular, there will be a focus on comparisons to experimental papers [28,110], which study the deformation of low density protein gels under creep deformation.

The rheological behaviours of protein (or biopolymeric) gels [26–32, 120], such as gelatine, agar and casein gels, are of great interest. They have relevance not only in biology [27–30,32], in areas such as muscle protein [28] and cellular tissue mechanics [27], but also in the processing and texturing areas of the food industry [31, 120–122]. Understanding how, when and why these materials fail is therefore of high significance.

The third project, the results of which are discussed in Chapter 6, explores the strain recovery of an amorphous material under the creep-recovery test protocol. The creep-recovery test features the creep protocol just described, followed by a switch-off of the stress after a certain time. After the stress is switched off, some of the forward strain gained during creep can be recovered in the reverse direction [123]. This protocol has been studied experimentally [50, 53, 77], with some theoretical modelling for specific material systems [124,125]. There is also a wider range of studies on modelling strain recovery in other protocols such as an oscillating shear [126–129]. This work puts forward the SGR model as a candidate that can produce complex strain recovery behaviours applicable to a wider range of materials than that seen before, and also explain how the material response depends on input parameters.

The focus of Chapter 6 is on the recoverable strain, an important property in hydrogels [52–55, 127, 130, 131], shape memory polymers [132–139], and polymer melts [128, 140, 141]. These materials have a wide range of applications [133, 134, 141, 142], for example, shape memory polymers are used in medical tools such as synthetic cardiovascular devices [142]. The recoverable strain of a material allows categorisation of its elastic and viscous properties, and also enables an understanding of its behaviour when approaching fluidisation [53, 129, 143, 144]. Using the SGR model, the mesoscopic response can be studied, and reveals that, perhaps counter-intuitively, recoverable strain can in fact be a result of the plastic events within the material, a concept known as reversible plasticity [58, 135–139, 145–151].

Chapter 6 not only finds significant recoverable strain in these materials for a range of input parameters, but also some interesting non-monotonic strain relaxation. It also elucidates the general dependencies of the recoverable strain on the relevant protocol input parameters, which are comparable to experimental results [57,124,140,152,153]. It sets the foundation for future work in refining the model towards a universal model for the recoverability of amorphous materials.

The outline of this thesis is as follows: Chapter 2 introduces rheology and the models used in this thesis; Chapter 3 outlines their implementation; Chapters 4 to 6 present and discuss the results of the three different projects just described; and Chapter 7 summarises the findings and provides concluding remarks.

Chapter 2

Theory

2.1 An Introduction to Rheology

Rheological studies concern the deformation and flow of soft matter. A common example involves sandwiching a material between two plates, one fixed so that it remains stationary and one experiencing a horizontal force F_x, in a process known as shearing, as shown in Fig. 2.1 [60, 61]. This diagram allows three important macroscopic variables to be defined [61, 154–156]:

(i) The shear stress $\Sigma = F_x/A$.

(ii) The shear strain $\gamma = \Delta x/L_y$.

(iii) The shear strain rate $\dot{\gamma} = d\gamma/dt$.

Throughout this thesis, the 'shear' designation will be dropped because this work will not consider other macroscopic tensorial components such as the normal stress, which measures the intensity of internal forces acting on a material perpendicular to a given cross-sectional area [61, 156]. In addition, the protocols explored in this work will also be restricted to the application of shear, as in Fig. 2.1, and will not consider other imposed stresses such as tensile or compressive stresses [60, 61]. This will therefore in effect ignore any influence of non-shear flow, such as turbulence or rotational flows, or indeed wall slip, where the flow of a material can occur at the point of contact between the rheometer wall and the material [11,66,157,158]. This one-dimensional application of shear will also apply to the fluid elements, which can only strain along the flow direction x_{axis}. This allows the use of a simplified scalar approach [61,154–156].

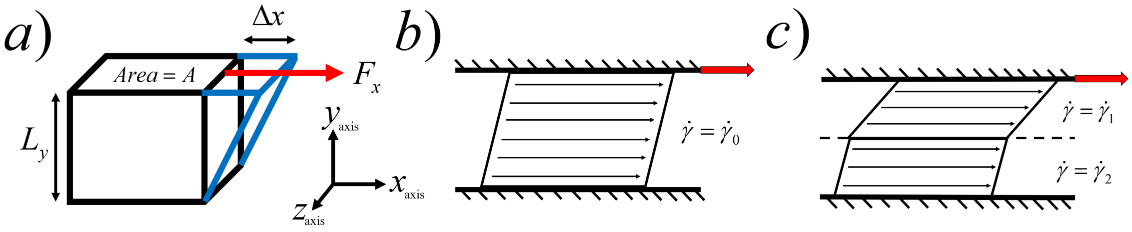

Figure 2.1: *a*) A material sandwiched between two plates of area A separated by distance L_y experiencing a shearing force F_x (red arrow) which has sheared the top plate by a distance Δx. The black lines represent the unsheared material, the blue lines the outline of the sheared material. Also highlighted are the axes representing the flow, x_{axis}, flow-gradient, y_{axis}, and vorticity, z_{axis}, directions.
b) The diagram in (*a*) shown in 2D, in the $x_{\text{axis}} - y_{\text{axis}}$ plane, to highlight the shear flow of a material between two plates. In this case, the shearing is homogeneous, with a constant shear rate across the system, equal to that of the imposed shear rate $\dot{\gamma}_0$.
c) The diagram in (*b*), but the shearing is now heterogeneous, displaying shear banding, where one band has shear rate $\dot{\gamma}_1$ and the other $\dot{\gamma}_2$.

This work also studies variation in the internal stresses and strains of the material. When variation in the flow field is allowed, it is restricted to the flow-gradient direction y_{axis}. Therefore, the internal shear strain can be defined as a function of the flow gradient $\gamma(y)$. When no internal variation is allowed, shear homogeneity across the system is enforced $\gamma(y) = \gamma$. Both approaches assume the flow to be uniform along the flow direction x_{axis} and along the vorticity direction z_{axis} [61,154–156].

In computational simulations one notionally considers the dimensions in which the length is not specified as infinite (in the case of Fig. 2.1, the x_{axis} and z_{axis} directions) which is clearly not possible in experiments. In addition, the one-dimensional horizontal geometry in the parallel plate protocol, though easier to model theoretically, is less practical in a laboratory scenario. Therefore, it is more common to see the Taylor-Couette protocol, where the material is located between concentric cylinders [10, 159]. However, this does not invalidate the parallel plate geometry presented here: in the limit of large cylinder radius relative to the plate spacing, the parallel plate geometry is recovered. This approximation is common in theoretical simulations [6, 9, 67, 160, 161].

Parts (b) and (c) of Fig. 2.1 show the difference between homogeneous shear flow and shear banding, as introduced in Chapter 1. Homogeneous shear flow, as in part (b), features one macroscopic strain rate $\dot{\gamma}_0$, which is universal across the system. When shear banding occurs, as in part (c), the shear flow becomes heterogeneous, with the example in Fig. 2.1 showing two bands of different strain rates $\dot{\gamma}_1$ and $\dot{\gamma}_2$. Experimental evidence for shear banding can be seen in a range of amorphous materials, from colloids to clays [3, 36–38], and has been shown in some systems to result in catastrophic failure [8–11, 84–86, 90, 110].

Measuring stress Σ and strain γ variables over multiple experiments/simulations allows the plotting of the steady state relationship between the stress and strain rate, known as the flow curve [61, 162]. This relationship can be seen for different materials in the top panels of Fig. 2.2, where the resultant steady state strain rate from an applied constant shear stress has been sketched. Note that it is also possible to apply a constant strain rate and measure the resultant steady state stress, in the simple example materials presented in Fig. 2.2 the result will be the same regardless of the method. Below the flow curves in Fig. 2.2 are example strain-time plots for a specified constant stress application.

The first part (a) of Fig. 2.2 displays the behaviour of a viscous Newtonian fluid, where the flow curve (top panel, black line) is linear $\Sigma_0 = \eta\dot{\gamma}$, where η is the Newtonian viscosity. The viscosity of a material is defined as the gradient of its flow curve, or equivalently, the resistance to deformation at a given strain rate [61, 67, 70,

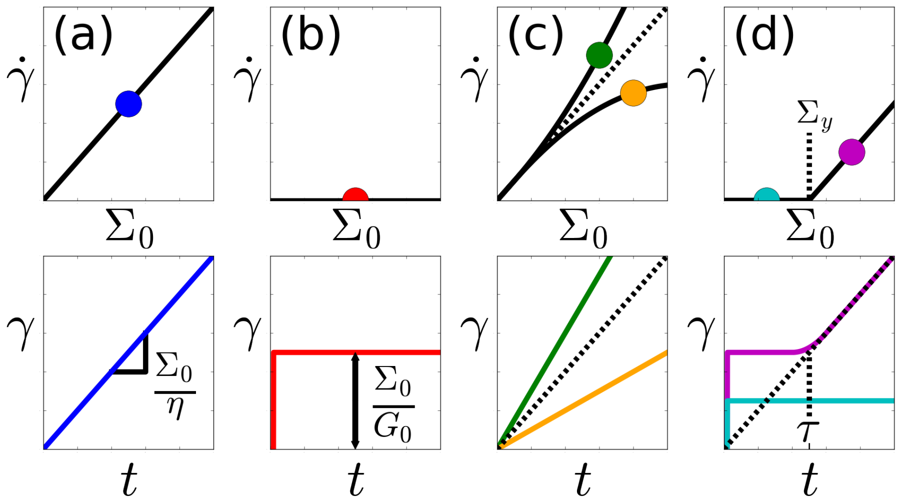

Figure 2.2: Schematic of the rheological behaviour of four different idealised materials: (a) Newtonian fluid, (b) Hookean solid, (c) shear thickening (yellow) and thinning (green) fluids, (d) visco-elastic fluid.
The top panels show the steady state flow curves of the material (black lines), the relationship between the steady state strain rate $\dot{\gamma}$ and the applied stress Σ_0, along with selected stresses (coloured circles) which correspond to single experiments/simulations where the selected stress has been held constant from time $t = 0$. The bottom panels show the strain response as a function of time of these selected points on the flow curve. Also highlighted in (d) are the yield stress of the material Σ_y and the relaxation timescale of the purple line response τ.

154]. The strain response over time is plotted in the bottom panel of (a) following the imposition at time $t = 0$ of a constant stress of amplitude indicated by the blue circle in the top panel. This response shows a constant strain increase, with gradient Σ_0/η. Therefore, a Newtonian fluid is defined by a constant strain rate proportional to a constant applied stress. Although no fluid is truly Newtonian, common liquids such as water can be assumed to be Newtonian in many circumstances [61, 162].

Part (b) of Fig. 2.2 displays the curves for the opposite extreme: an elastic Hookean solid. The flow curve (top panel, black line) has zero steady state strain rate $\dot{\gamma} = 0$ for all values of the imposed stress Σ_0. This can be understood by observing the strain as a function of time (bottom panel, red line), as the strain is constant at equilibrium. Thus, a Hookean solid initially shears an amount proportional to the imposed stress $\gamma = \Sigma_0/G_0$, with the shear modulus G_0 acting as the constant of proportionality. After this, it maintains that constant strain, resulting in an equilibrium strain rate of zero $\dot{\gamma} = 0$. The linear Hookean approximation only works experimentally at small stresses in elastic materials such as rubber [61, 162].

Many real soft materials do not follow either of these extremes, and they are classified as non-Newtonian fluids [61,163]. For example, the assumption of a constant viscosity in Newtonian liquids does not hold for the curves shown in part (c) of Fig. 2.2, which display shear thickening/thinning behaviour, in which the apparent material viscosity increases/decreases as the imposed stress increases [63, 76, 164–166].

There are also non-Newtonian materials that express very different behaviours depending on the imposed stress and the timescale that the material response is measured over. An example can be seen in part (d) of Fig. 2.2, which represents a simple visco-elastic material. The material appears to be solid up to a certain stress Σ_y and a liquid above it. This value is called the yield stress Σ_y. At imposed stresses below Σ_y the material behaves as an elastic solid, as can be seen from the cyan line strain response. Above the yield stress (the purple line strain response) the behaviour is more complex, initially reflecting that of a solid, elastically shearing to a constant strain. However, after a relaxation time τ, unable to hold the stress any longer, the material fluidises to a viscous liquid state (hence the term visco(us)-elastic) [9,60,167,168]. Bingham and Herschel-Bulkley fluids are two examples of yield stress materials [11,39,40].

There are, of course, a huge number of other non-Newtonian fluid behaviours not discussed here, and rarely do any materials conform to these ideal limiting cases. For example, there are generally a range of relaxation times in a system, rather than one τ as in the example above [169,170]. The deviation from idealised behaviour is particularly relevant when discussing amorphous materials, which display a level of structure, but lack the long-range order of crystalline solids [34,167,168]. This intrinsic disorder leads to many interesting phenomena that expand beyond the somewhat simplified behaviours described above. One example of complex amorphous material behaviour relevant to the work in this thesis is the phenomenon of rheological ageing and annealing [9,11,71,81,83].

The concept of ageing, where an initially liquid-like sample slowly evolves towards an ever more solid-like state as a function of the time since it was prepared [23], was introduced in Chapter 1. Ageing generally occurs in a sample at rest, where a material is aged for a certain time before the application of shear [13,23,51,83,93]. How the ageing process affects materials is system dependent. For example, if there are unresolved strains within a soft system, then ageing can allow the time for these defects to resolve [11,48]. Defects can function as weak points through which the system can more easily fail [28,110]. Therefore, ageing in this context results in a strengthened system. In a polymeric system, ageing can allow the system to increase connectivity, which reinforces the cross-linked network over time [10,51,53,66,157].

Annealing also causes the solidification of amorphous systems, but through a different process [9]. An amorphous material is initially equilibrated at a high temperature, generally causing the system to be liquid-like. Then the temperature is reduced, decreasing particle energy, slowing the system down, and causing the material to become increasingly solid-like [9,103,104,171]. Similar to ageing, the annealing process can affect the distribution of strain throughout the material through defects

[9, 11, 48, 103, 171]. It can also affect the relaxation times present in amorphous materials [169, 170]. The annealing process is common in glassy systems, where a change in temperature can affect the glass transition [11, 72, 73], as discussed in Chapter 1. Experimentally, the degree of annealing can be tuned by the size of the temperature difference and the rate at which the temperature is changed, for example in the annealing of metallic glasses [48, 169–171].

Complex amorphous material behaviours like ageing and annealing require theoretical models more advanced than the simplified examples presented above. The rest of this chapter is dedicated to describing the models that are used in this work.

2.2 The Soft Glassy Rheology (SGR) Model

2.2.1 With Enforced Homogeneity in Shear

First proposed by Sollich and others in 1997 [92], the Soft Glassy Rheology (SGR) model [13, 23–25, 71, 81, 92, 172] is a powerful tool in investigating the behaviour of a range of amorphous materials, such as colloidal dispersions and gel networks [13, 24, 173]. It forms the foundation upon which the simulations of this thesis are built.

It is a trap model [9, 11] that considers splitting the material into a number, $m = 1 \dots M$, of local mesoscopic 'elements' whose size fit the following criteria [71]:

(i) Small enough to allow the macroscopic behaviour to be described by an average over multiple elements.

(ii) Large enough so that deformations on the scale of an element can be described by local continuum elastic strain and stress variables (average over a single element).

Note that this division into mesoscopic elements is a largely conceptual tool and should not be thought of as corresponding to tightly defined physical areas or boundaries of a material. However, each element may notionally be thought of as representing a cluster of particles or molecules. For example, a few droplets in an emulsion or colloidal system, or several hundred metallic glass particles [49, 62]. In the simulation, the elements have no spatial dependence on each other, and are all restricted to move only in the flow direction x_{axis}.

The SGR model takes inspiration from Bouchaud's glass model [174, 175], which considers an ensemble of elements that explore an energy landscape of traps of various depths. These elements can 'hop' between traps via an activation process. These hops can be considered as a plastic rearrangement of the cluster of particles or molecules. Localised rearrangements have been seen experimentally to occur on the scale of a group of a few colloidal [62] or several hundred metallic [49] glass particles. Bouchaud assumed that the activation of these hops was caused by thermal fluctuations. However, the trap depths in the materials the SGR model generally simulates are large compared to $k_B T$, so this is unlikely to be the cause in this case [82]. The SGR model instead attributes the activation to interactions between elements; a rearrangement takes place somewhere in the material which can then propagate and cause rearrangements elsewhere [71]. This coupling between elements is represented by a constant effective noise temperature x, which provides the activation energy for elements to hop [8, 71, 92].

The SGR model incorporates strain degrees of freedom into this glass model to explore the consequences of deformation and flow [71]. Each element (with index m) is assigned a local strain l_m, elastic constant k (the same for all elements), corresponding stress kl_m, and stored elastic energy $E_{\mathrm{el}}(l_m) = \frac{1}{2}kl_m^2$. These qualities describe deformation away from some local position of unstressed equilibrium relative to neighbouring elements [81]. Each element is also placed in an energy well of depth E_m.

Following the insight from Bouchaud [174], the model can capture a glass transition if the prior distribution $\rho_0(E)$ of element trap depth energies E across the landscape follows the exponential form

$$\rho_0(E) = \frac{1}{x_{\mathrm{g}}} \exp\left(-\frac{E}{x_{\mathrm{g}}}\right) , \tag{2.2.1}$$

where the glass transition occurs at noise temperature $x = x_{\mathrm{g}}$ [71, 174]. The effects of structural disorder are modelled by assuming trap depth energies follow this distribution [71]. $\rho_0(E)$ represents the distribution of E across the landscape that the elements explore. It is labelled the 'prior' distribution due to the fact that elements are initialised with energy well depths taken from this distribution. However, the distribution of energy well depths across elements will change when elements start experiencing yield events, because yield events result in hops to new energy wells.

A yield event occurs when an element under a strain l_m releases its stored elastic energy $E_{\mathrm{el}}(l_m)$ through a spontaneous local rearrangement that reduces the element's stress. The probability that, within a time interval Δt, a given element yields, has previously been given as

$$p(E_m, l_m) = r(E_m, l_m)\Delta t = \Gamma_0 \exp\left[-\frac{(E_m - E_{\mathrm{el}}(l_m))}{x}\right]\Delta t\,, \tag{2.2.2}$$

where $r(E_m, l_m)$ is the yielding rate of element m with energy well depth E_m and strain l_m. Γ_0 represents the attempt frequency. Eq. (2.2.2) envisages the trap that the element experiences as an exponential harmonic well [71, 81, 92].

This research utilises a slight variation on the yielding probability, where an upper limit is placed on the rate of yielding [91]

$$p(E_m, l_m) = r(E_m, l_m)\Delta t = \begin{cases} \Gamma_0 \exp\left[-\frac{(E_m - E_{\mathrm{el}}(l_m))}{x}\right]\Delta t, & \text{if } E_{el}(l_m) < E_m \\ \Gamma_0 \Delta t, & \text{if } E_{\mathrm{el}}(l_m) \geq E_m \end{cases}. \tag{2.2.3}$$

This alteration implies that once the stored elastic energy becomes larger than the trap depth energy - essentially once the element has 'escaped' the trap - the probability of yielding is constant with increasing strain, rather than rising indefinitely as in the original form in Eq. (2.2.2) [91]. This previous definition in Eq. (2.2.2) also requires an infinitely small timestep to ensure that all probabilities of yielding are less than one, which is not necessary in the alternate version. Regardless, elements rarely explore strains that are large enough to probe this difference, so results should be similar irrespective of the modelling of yielding probabilities at extreme strains.

For a newly prepared, undeformed sample, it is assumed that $l_m = 0$ for each element [71, 81]. Although in a real experimental study it is possible that there could be a distribution of local strains within the material before shear, it can be argued that the disorder caused by these defects and impurities are modelled in this case by the distribution of energy well depths E [71, 81, 174].

The subsequent application of a macroscopic stress or strain will initially deform each element elastically from its local equilibrium configuration, giving rise to a non-zero local strain $l_m \neq 0$. This will result in a non-zero stored elastic energy $E_{\text{el}}(l_m) = \frac{1}{2}kl_m^2 > 0$ which will increase the probability of yielding according to Eq. (2.2.3). At some point, determined by a stochastic process described further in Section 3.1.3, the element will yield, rearranging itself to a configuration in which it is no longer deformed, thus relaxing stress and returning l_m to 0 [92].

This yield event is modelled as a hop to a new trap. Note that this yield event can occur without any strain imposed, as $r(E_m, l_m)$ in Eq. (2.2.3) is non-zero even when $l_m = 0$ for $x > 0$. This is because an element's yielding process can be activated either through an imposed strain as described above, or caused by interactions with other yielding elements represented by x. The SGR model treats both cases in a unified fashion via Eq. (2.2.3). This concept will be discussed further in Section 3.1.1, where element hopping between energy wells in a system under no strain results in rheological ageing.

A key assumption of this model is that, after yielding, the energy depth of the new trap is completely independent of the old one, randomly chosen from the prior trap depth energy distribution $\rho_0(E)$ specified in Eq. (2.2.1) [71, 81, 92]. The process of selecting a new trap is assumed to be instantaneous, and therefore the timescale for element reformation τ_{reform} can be considered to be zero, $\tau_{\text{reform}} = 0$. See Fig. 2.3 for a diagram representing the process of element straining, rearrangement, and hopping into a new well.

It is assumed, informed by the literature [71, 91, 92], that the behaviour of elements between yield events represents elastic deformation. Therefore, the local element strain rate is equal to the macroscopic strain rate $\dot{l}_m = \dot{\gamma} \; \forall \; m$, meaning the shear rate is homogeneous throughout the material and equal to the imposed strain rate. This restriction enforces homogeneous shear within the system, as discussed in Section 2.1. This means that there is no variation in the flow profile across the flow gradient direction y_{axis}.

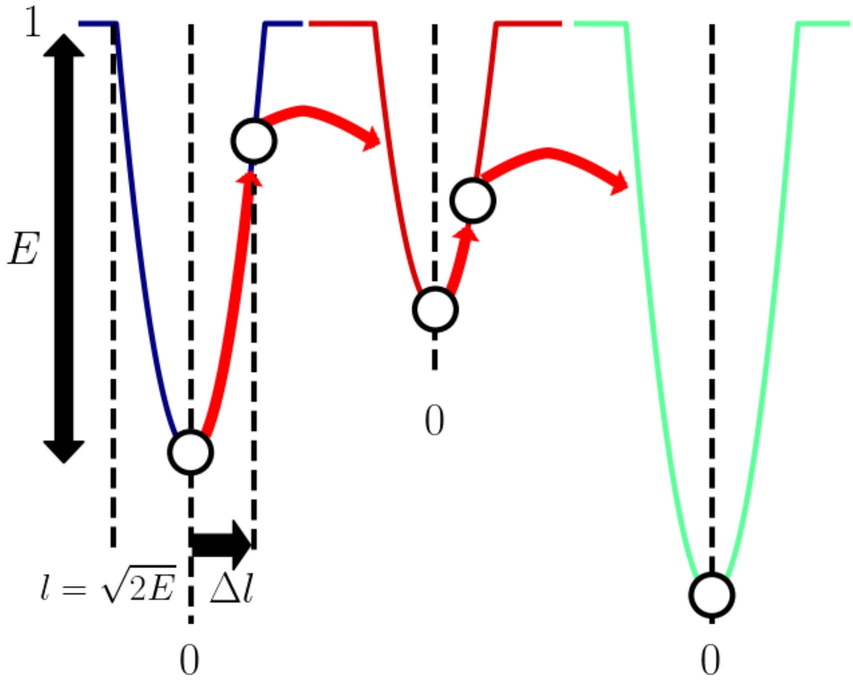

Figure 2.3: A diagram outlining the behaviour of the elements in the SGR model, which hop between energy wells of depth E. Increasing the element strain l pushes the element up the well, increasing its probability of yielding per unit time according to Eq. (2.2.3). By random noise activation, the element can yield, resetting its strain to $l = 0$ and choosing a new energy well. This process is shown in the red arrows, with the red and green wells examples of new wells that might be chosen from the prior distribution $\rho_0(E)$ of element trap depth energies.

The macroscopic total visco-elastic stress σ is assumed to be the average of all the individual element stresses

$$\sigma = \frac{k}{M} \sum_{m=0}^{M} l_m \,. \tag{2.2.4}$$

The total macroscopic stress Σ is then assumed to be the sum of the visco-elastic stress σ and the Newtonian viscous stress of the background solvent, the solvent viscosity η multiplied by the macroscopic strain rate $\dot{\gamma}$ [64, 71, 81, 92]

$$\Sigma = \sigma + \eta\dot{\gamma} \,. \tag{2.2.5}$$

The background solvent is present to enable the calculation of the strain rate $\dot{\gamma}$, otherwise the system will have the capacity for unphysical infinite strain rates where the total stress Σ changes instantaneously with the visco-elastic stress σ. However, the behaviour of this Newtonian background solvent that the mesoscopic elements exist within is not the primary interest of these simulations, so its viscosity η is generally given a small value to minimise the impact of the solvent [67, 70]. Removing the solvent entirely, by setting the viscosity to zero, $\eta = 0$, requires a different algorithm, which is introduced in Section 2.2.3.

The SGR model, even with enforced homogeneity in shear, is powerful in the sense that it accurately captures many phenomena displayed by amorphous materials, including ageing, yield events, yield stresses, and a stress overshoot under shear startup [71, 93]. However, due to the enforcement of homogeneous strain rate throughout the material, it cannot display the macroscopic shear heterogeneity that arises in shear banding [13, 24, 25]. Despite this, the work in this thesis will utilise the model as just described where the assumption of homogeneity in shear is valid, and additionally as a control tool to compare with the heterogeneous shear case.

2.2.2 With Allowed Heterogeneity in Shear

The extension of the SGR model to allow for heterogeneity in shear, and therefore shear banding, is sketched in Fig. 2.4 [13, 24, 25].

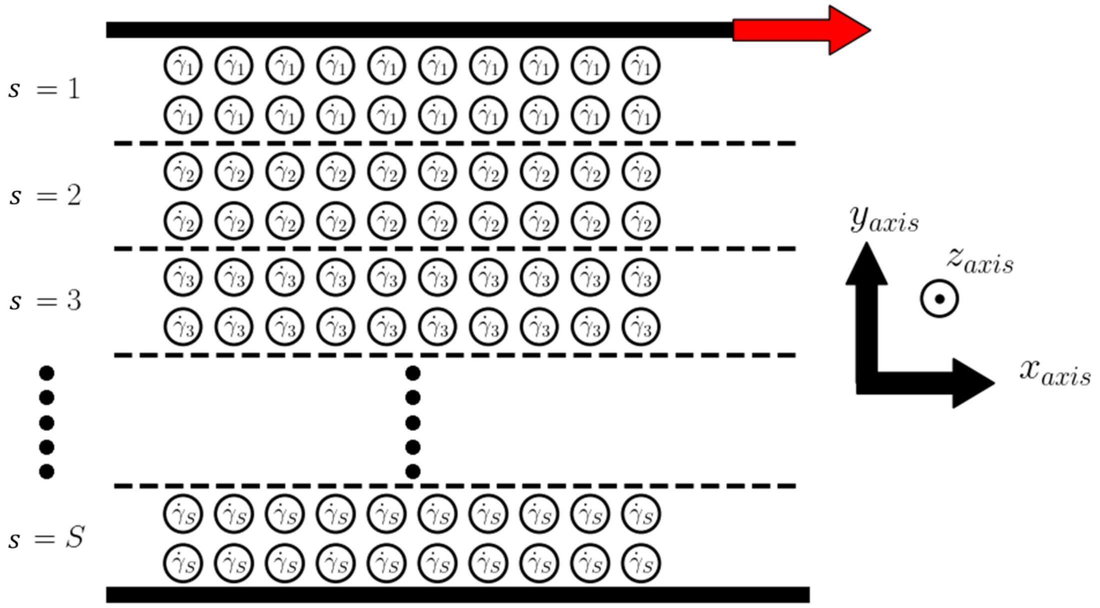

Figure 2.4: A diagram to outline the element distribution in the SGR model, where elements are organised into S ($s = 1 \ldots S$) number of streamlines, with M elements per streamline. All elements on a streamline have the same strain rate $\dot{\gamma}_s$, which is allowed to vary across streamlines. Homogeneous shear can be enforced by setting the number of streamlines to $S = 1$. There is no spatial dependence between elements within streamlines, the two rows and regular order per streamline are simply for visual purposes. Additionally, the top and bottom plates are purely diagrammatic, as the models presented in this thesis use periodic boundary conditions. The application of strain is shown through the red arrow.

The flow-gradient coordinate y_{axis} is discretised into S ($s = 1 \ldots S$) streamlines, equally spaced by distance $\Delta_y = L_y/S$, where L_y is the width of the sample in the y_{axis} direction, equal to the distance between the two plates, see Fig. 2.1 and Fig. 2.4 [13, 24, 25].

Each streamline is then assigned M ($m = 1 \ldots M$) SGR elements which, within each streamline, follow the behaviour described in Section 2.2.1. This means that, within each streamline s, the elements have a distribution of trap depth energies E_{sm}, and experience the straining and yielding described in Section 2.2.1. Indeed, they are all forced to experience the same strain rate of their streamline $\dot{l}_{sm} = \dot{\gamma}_s \; \forall \; m$. Accordingly, the SGR model with homogeneous shear enforced is recovered by simulating the entire material as one streamline, by setting $S = 1$.

Importantly, to allow shear heterogeneity, the streamline strain rate $\dot{\gamma}_s$ can vary across streamlines. The model is thus capable of capturing heterogeneous flow, with streamlines shearing at different rates. This extension allows spatial variation in the flow-gradient direction y_{axis}, with translational invariance still assumed in the flow x_{axis} and vorticity z_{axis} directions [25]. Note that there is still no spatial dependence between elements within streamlines. Periodic boundary conditions are used, with the assumption that all fields are smooth at the edge of each sample [160,161,176]. This removes any influence external to the material or edge effects, such as wall slip [42,66,157,158].

The process of allowing shear heterogeneity into the SGR model enables almost all of the physics described in the previous section to stay the same with just a few modifications. The total visco-elastic stress in Eq. (2.2.4) is now the streamline visco-elastic stress σ_s with the total visco-elastic stress σ now represented by the average $\bar{\sigma}$ of the streamline visco-elastic stresses

$$\sigma = \bar{\sigma} = \frac{1}{S}\sum_{s=0}^{S} \sigma_s \, , \qquad \sigma_s = \frac{k}{M}\sum_{m=0}^{M} l_{sm} \, . \tag{2.2.6}$$

Force balance imposes continuity in total stress across the flow-gradient direction y_{axis}. Therefore, the average $\bar{\Sigma}$ and streamline Σ_s total stresses can be equated

$$\bar{\Sigma} = \bar{\sigma} + \eta\bar{\dot{\gamma}} \, , \qquad \Sigma_s = \sigma_s + \eta\dot{\gamma}_s \, , \qquad \bar{\Sigma} = \Sigma_s \, . \tag{2.2.7}$$

Rearranging then provides an equation for the streamline strain rate

$$\dot{\gamma}_s = \bar{\dot{\gamma}} + \frac{\bar{\sigma} - \sigma_s}{\eta} \,. \tag{2.2.8}$$

In a shear protocol where the strain or strain rate is controlled, the total average strain rate $\bar{\dot{\gamma}} = \frac{1}{S}\sum_{s=0}^{S} \dot{\gamma}_s$ is specified by the imposed strain rate $\bar{\dot{\gamma}} = \dot{\gamma}_0$. For a stress-controlled protocol, it is the total stress that is specified by the imposed stress $\Sigma = \Sigma_0$.

With allowed shear heterogeneity, the SGR model has been shown to capture many phenomena in the heterogeneous flows of dense amorphous materials [13, 24, 25].

2.2.3 With Zero Viscosity

In the work in this thesis, the SGR model with zero solvent viscosity $\eta = 0$ is only utilised under a stress-controlled protocol and with homogeneity enforced. Hence, the theory under these conditions will be the focus in this section.

In Eq. (2.2.5), the solvent viscosity η allows the calculation of the strain rate $\dot{\gamma}$ of the system, and removes the potential for infinite strain rates. However, it is possible to implement zero viscosity $\eta = 0$ through a change to the calculation of the macroscopic strain rate $\dot{\gamma}$ [16, 177].

When viscosity is non-zero $\eta > 0$, the amount of yielded strain through element rearrangement events defines the visco-elastic stress σ, as in Eq. (2.2.4), which then defines the macroscopic strain rate $\dot{\gamma}$ through Eq. (2.2.5). When viscosity is set to zero $\eta \to 0$ in this scenario, the strain rate tends to infinity $\dot{\gamma} \to \infty$ [16, 177]. To allow zero viscosity without a divergence in $\dot{\gamma}$, the system must effectively predict the amount of yielded strain within a timestep by taking the average of the element yield rates $r(E_m, l_m)$ multiplied by their strain l_m [177]

$$\dot{\gamma} = \frac{1}{M}\sum_{m=0}^{M} r(E_m, l_m) l_m \,. \tag{2.2.9}$$

This variant of the SGR model has been presented with shear homogeneity enforced through only one streamline $S = 1$, as that is the only context under which it is used in this thesis. It can however be adapted to allow shear heterogeneity by making the calculation in Eq. (2.2.9) equal instead to the streamline strain rate $\dot{\gamma}_s$.

2.2.4 Limitations

One limitation of the SGR model is the lack of a comprehensive or universal physical interpretation for the effective noise temperature x or attempt frequency Γ_0 in Eq. (2.2.3). Both parameters have been considered as constant in much of the literature [13, 24, 71, 81, 92], though some studies have considered a dependence on the imposed shear or state of the system [71,92]. There has also been some discussion on whether x can be considered a thermal temperature for systems where the energy depths of the mesoscopic elements are on the scale of k_bT [70, 178]. Nonetheless, to date, x and Γ_0 remain phenomenological parameters that cannot be derived from first principles [13, 24, 71, 81]. However, the wide-ranging success of the SGR model in simulating the behaviour of amorphous materials, even when x and Γ_0 are taken to be constant [24, 71, 81, 92], is sufficient to justify its use.

A feature of the SGR model often lauded as an advantage but that could also be seen as a limitation is the fact that its mesoscopic physics is highly generic. The generic nature of the model makes it versatile, and it can be used for a large number of different material applications. However, the lack of specificity means there is little indication of how the parameters of the model should be varied to address different classes of physical systems [13]. Part of the motivation for using alternative models and modifications of the SGR model, as in the first two projects of this thesis and described in the following two sections, is to explore how increasing the specificity of the SGR model can strengthen it as a tool for modelling amorphous materials.

2.3 The Thermal Elasto-Plastic (TEP) Model

2.3.1 Element-Based Model

Thermal Elasto-Plastic (TEP) models cover a huge range of mesoscopic models [9, 11, 94–105, 171]. They are widely discussed in literature, particularly in the statistical physics community, as simple and effective models for simulating amorphous materials [9, 111, 117]. The TEP model used in this project is in fact very similar to the SGR model. However, the energy landscape of traps for elements and the lengthy ageing process are removed and replaced with physics more representative of annealing.

The primary difference between this TEP model and the SGR model is that the distribution of element energy depths E_{sm} in Eq. (2.2.1) is removed. Instead, each element trap is assumed to have the same energy depth $E_{sm} = 1$, effectively nullifying the influence of this variable. Also, upon a yielding event, a new energy depth is no longer chosen from Eq. (2.2.1), the element simply hops to a new well that has the same depth $E_{sm} = 1$.

This change to the energy depth distribution will interrupt the ageing process that was present in the SGR model, which relies on the changing of energy depths (further discussed in Section 3.1.1). It is replaced with an initialisation of the system with a distribution $P_0(l_{sm})$ of element strains l_{sm} randomly chosen from a normalised Gaussian

$$P_0(l) = \frac{1}{\sqrt{2x_0\pi}} \exp\left(-\frac{l^2}{2x_0}\right) , \tag{2.3.1}$$

prior to the application of shear [9, 103, 104]. This initial distribution of element strains for different values of x_0 can be seen in the left panel of Fig. 2.5. Note that in the SGR model, the equivalent initial distribution of element strains is a delta function $P_0(l) = \delta(l)$, where all elements have $l_{sm} = 0$.

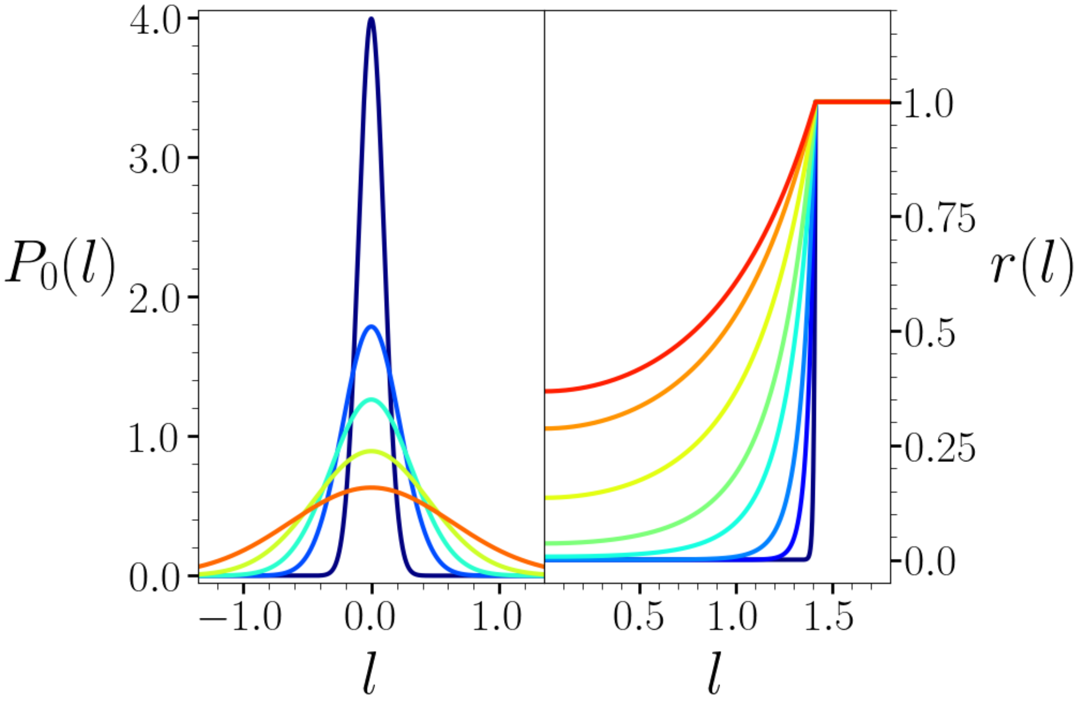

Figure 2.5: **Left panel**: The initial distribution of element strains $P_0(l)$ in strain space l, a Gaussian with width defined by the pre-shear equilibrium temperature x_0, as in Eq. (2.3.1). The different colours represent different values of $x_0 = [0.01, 0.05, 0.1, 0.2, 0.4]$ (from the thin and tall Gaussian in dark blue to the shorter wider Gaussian in orange).

Right panel: The yielding rate function $r(l)$ in strain space l for different values of the working temperature $x = [0.01, 0.05, 0.1, 0.2, 0.3, 0.5, 0.8, 1.0]$ (from the steep function in dark blue to the shallow function in red).

The width of the Gaussian in Eq. (2.3.1), x_0, models the preshear equilibrium temperature, and dictates the effective annealing of the material. In this case, the smaller values of x_0 correspond to a better annealed material, because the strain distribution is more uniform across the system [171]. In this work, the polar form of the Box-Muller Transform [179] is used to select randomly from this distribution.

The replacement of the distribution of energy depths with a universal one $E_{sm} = 1$ also means that the yielding rate $r(E_{sm}, l_{sm})$ (Eq. (2.2.3)) no longer depends on the element energy depth E_{sm}

$$r(E_{sm}, l_{sm}) = r(l_{sm}) = \begin{cases} \Gamma_0 \exp\left[-\frac{(1-E_{\mathrm{el}}(l_{sm}))}{x}\right], & \text{if } E_{el}(l_{sm}) < 1 \\ \Gamma_0, & \text{if } E_{\mathrm{el}}(l_{sm}) \geq 1 \end{cases} . \tag{2.3.2}$$

This function is plotted in the right panel of Fig. 2.5 for different values of the working temperature x, which defines the slope of the yielding rate $r(l_{sm})$ below the $E_{\mathrm{el}}(l_{sm}) = \frac{1}{2}l^2 = 1$ (or equivalently, $l = \sqrt{2}$) threshold.

Aside from the above changes, the simulation proceeds as described in the SGR model, elements in streamlines elastically deforming ($l_{sm} \to l_{sm} > 0 \implies E_{\mathrm{el}}(l_{sm}) > 0$), plastically yielding ($l_{sm} \to 0$), and rearranging/reforming to repeat the process.

2.3.2 Fokker-Planck Equation

It is possible to describe the TEP model through continuum equations rather than considering individual elements. With all elements in the TEP model in identical traps $E_{sm} = 1$, the only difference between elements is in the element strain l_{sm}. Therefore, the distribution of the element strains on a streamline $P(l_{sm})$, initially a Gaussian distribution $P_0(l_{sm})$ as in Fig. 2.5 and Eq. (2.3.1), is equivalent to a probability density function of the strain of that streamline $P(l_{sm}) \simeq P_s(l)$ in strain space l. This approximation is valid in the limit of large number of elements $M \gg 1$.

$P_s(l)$ has an equation of motion given by the Fokker Planck equation [180, 181]

$$\frac{dP_s(l,t)}{dt} = -\underbrace{r(l)P_s(l,t)}_{\text{`death'}} + \underbrace{Y_s P_0(l)}_{\text{`rebirth'}} - \underbrace{\dot{\gamma}_s \frac{dP_s(l,t)}{dl}}_{\text{advective streamline strain rate}} , \tag{2.3.3}$$

where

$$Y_s = \int r(l)P_s(l,t)\, dl\,, \tag{2.3.4}$$

$$\sigma_s = \int lP_s(l,t)\, dl\,, \tag{2.3.5}$$

$$1 = \int P_s(l,t)\, dl\,. \tag{2.3.6}$$

The first term on the right hand side of Eq. (2.3.3) implements yielding, or the 'death', of the strain distribution $P_s(l,t)$, the multiplication of the yielding rate function $r(l)$ (Eq. (2.3.2)) and $P_s(l,t)$ denoting the level of yielding. The second term models the reformation, or 'rebirth', of $P_s(l,t)$ after yielding. The third term outlines the effect of the strain rate, encoding which way the streamline is straining and how the resultant value of $P_s(l,t)$ changes.

With a definition for the visco-elastic streamline stress σ_s in Eq. (2.3.5), the rest of the calculations required for the continuum simulation are identical to that of the element model, using Eq. (2.2.6) and Eq. (2.2.8) for the stress and strain rates respectively.

This method is marginally more efficient numerically than evolving an ensemble of elements. However, the results produced are identical to the element model within numerical error, so either can be used in practice.

2.4 Modification to the SGR Model to Address Gel Fracture

The SGR model has been applied to a wide range of materials, such as foams, emulsions, colloidal glasses and suspensions [9, 13, 23–25, 71, 92]. Indeed, the materials studied to date with the SGR model are mostly densely packed jammed and glassy systems, which tend to rejuvenate under shear [9, 13, 23–25, 71, 92]. Localised yield events that relax strain involve the rearrangement of a cluster of particles or molecules which are subsequently capable of straining again [6, 7, 9, 10, 20, 41–44, 62]. In the SGR model, this process is simulated through plastic element yield events followed by reformation [71, 81, 92]. An element yield event models a local rearrangement that results in the relaxation of stress but also the reformation of the element with a new energy depth E, as described in Section 2.2.1. The timescale for this reformation is zero, $\tau_{\text{reform}} = 0$, the process of reformation post-yield is instantaneous. This reformation allows reversible yielding transitions between solid-like and fluid-like states which applies to a range of soft materials [9, 10, 27, 70].

This reversibility does not, however, apply to protein gels. These low-density polymer gels can be described as ‘brittle-like soft solids’ that experience irreversible rupture [110]. Numerous literature studies, experimental and theoretical, have shown that when strong interparticle bonds are involved, as in protein gels, soft solids develop fractures and irreversibly break under stress [27, 110, 182–184]. In addition, these fractures are due to the build-up of plastic deformations within individual gel strands [182, 183]. Fibre bundle models, which simulate a group of fibres that can irreversibly ‘snap’, have had some success in modelling protein gels [106, 110]. Clearly, the SGR model requires a modification if it is to accurately simulate these protein gels [19, 27, 59, 182].

The modification, new to the field, takes the framework of the standard SGR model but considers a permanent ‘breaking’ of elements, similar to the ‘snapping’ of fibres in fibre bundle models [9, 106]. Within the framework of the SGR model, this irreversible snapping of fibres is modelled by prohibiting the post-yield reformation of elements. To do this, the timescale for reformation is set to infinity, $\tau_{\text{reform}} = \infty$. In practice this means that, when an element yields, its modulus is set permanently to zero. The element is therefore ’broken’, and can no longer contribute to the stress within the system.

The consequence of this modification is to limit the lifetime of the material. An element that experiences a yield event breaks irreversibly and can no longer sustain an elastic stress. Once all the elements have yielded, all that remains is the background Newtonian solvent. As will be discussed in Chapter 5, the gel component is considered to have ‘broken’ at this point.

The other aspects of the SGR model, beyond the reformation of elements, do not require modification. The mesoscopic structure of elements is reminiscent of the globular nature of protein gels [184], and the stochastic structure of protein gels is similar to the random-number based computational processes present in the SGR model [183]. In addition, protein gels have been found to contain a wide range of bonds with different energies and lifetimes, comparable to the range of element energy wells E [28]. Therefore, with just the modification described above, the SGR model becomes a prime candidate for simulating protein gels.

2.5 Shear Protocols

2.5.1 Step Strain

The step strain protocol is the focus of Chapter 4. It was one of the shear protocols in an early SGR paper [71], where the response to this protocol was explored with shear homogeneity enforced.

A step strain is modelled in this work as follows: after any ageing processes, a strain of amplitude γ_0 is instantaneously applied at $t = 0$ and is held constant until the end of the simulation time. One can represent this mathematically as a Heaviside step function for strain $\gamma(t) = H(t)\gamma_0$, corresponding to a Dirac delta function for strain rate $\dot{\gamma}(t) = \delta(t)\gamma_0$. The applied strain and a typical stress response are sketched in the top panel of Fig. 2.6.

Of course, reproducing this idealised step strain experimentally is physically impossible, because any real rheological device is limited by inertia. However, it can be argued that within the time scales relevant to the material, particularly for a well-aged material, a swiftly applied step strain can be modelled effectively as an instantaneous one. This process of an experimental 'rapid strain ramp' has been explored in literature, for example in polymer melts [66, 185–187].

In preparation for the work presented here, the process of applying a rapid strain ramp was tested for both the SGR and TEP model simulations and it is found that as long as the material maintains a fully elastic reaction to the strain over the duration of its application, the strain application can be considered instantaneous. In other words, there is negligible difference between simulations with an instantaneous step in the strain and those with a rapid strain ramp, as long as the ramp is fast compared to the intrinsic relaxation timescales of the material [188].

This statement can be understood by considering a strain ramp of rate $\dot{\gamma}_0$ that stops once it reaches the target strain γ_0. Recall the fact that outside of yield events the elements behave elastically $\dot{l}_{sm} = \dot{\gamma}_0$, meaning the element strain rate is equal to the imposed ramp strain rate. As long as no element has experienced a yield event by the end of the ramp (i.e. the strain ramp has been fast enough), all elements will have a resulting strain $l_{sm} = \gamma_0$. This is equivalent to simply setting this condition at the start of the simulation, as done in the instantaneous step strain protocol.

From this work and others [24, 25, 91, 185, 186], it should be possible to calculate how these conditions can be met experimentally by studying the response to a constant strain rate, of which the rapid strain ramp will be an extremely steep and temporary version.

2.5.2 Step Stress

The step stress protocol is the focus of Chapter 5. It has been widely studied, both in the SGR model [25, 87] and for a range of amorphous materials [9, 11, 28, 36, 43, 81, 107–109, 112–116], for example in protein gels [28, 110, 189].

A step stress is modelled in this work as follows: after any ageing processes, a stress of amplitude Σ_0 is instantaneously applied at $t = 0$ and is held constant until the end

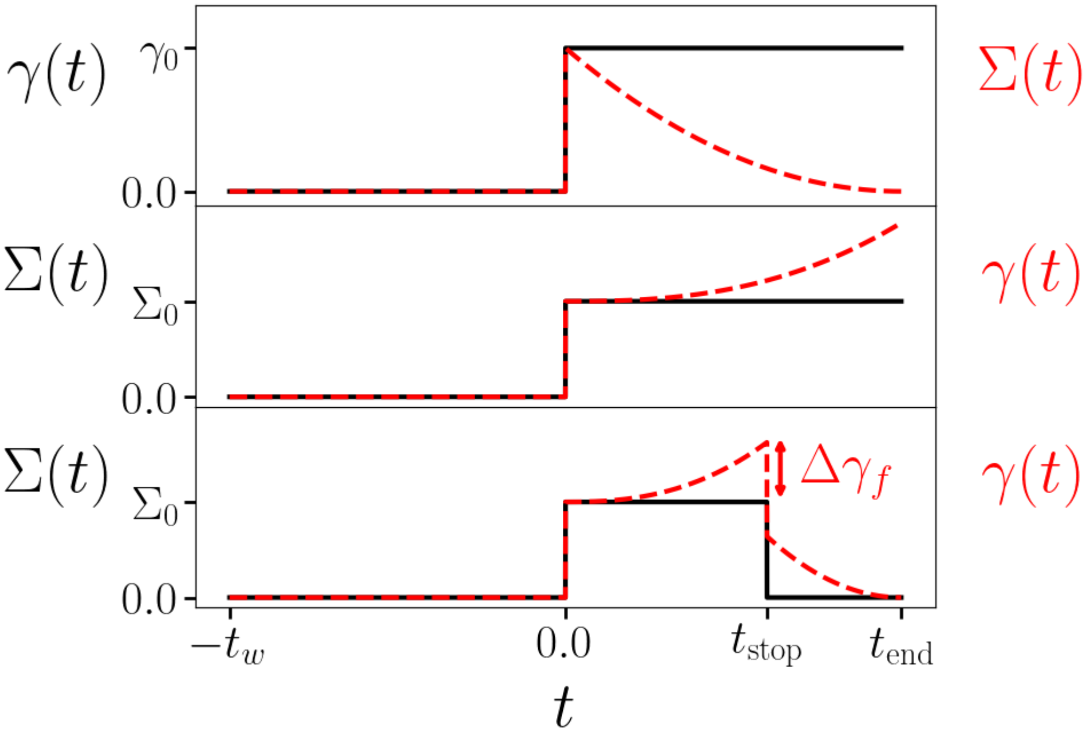

Figure 2.6: Diagrams showing the three shear protocols studied in this thesis as a function of time. The imposed variable is shown in the solid black line, and an example measured material response is shown in the dashed red line.
Top panel: The step strain protocol. A constant strain of amplitude γ_0 is applied at time $t = 0$ and held constant until the end of the simulation $t = t_{\text{end}}$. An example stress response $\Sigma(t)$ to the protocol is shown in the red dashed line.
Middle panel: The step stress protocol. A constant stress of amplitude Σ_0 is applied at time $t = 0$ and held constant until the end of the simulation $t = t_{\text{end}}$. An example strain response $\gamma(t)$ to the protocol is shown in the red dashed line.
Bottom panel: The creep-recovery test protocol. A constant stress of amplitude Σ_0 is applied at time $t = 0$ and held constant until a time $t = t_{\text{stop}}$, where the stress is switched off and remains at zero until the end of the simulation $t = t_{\text{end}}$. The switch-off time is defined as the time at which the strain reaches a certain value $t_{\text{stop}} = t(\gamma = \gamma_0 + \Delta\gamma_f)$. An example strain response $\gamma(t)$ to the protocol is shown in red dashed line.

of the simulation time. One can represent this mathematically as a Heaviside step function for stress $\Sigma(t) = H(t)\Sigma_0$. The applied stress and a typical strain response are sketched in the middle panel of Fig. 2.6. In experimental practice, this protocol also requires a ramp up to the required stress, but this process is more established than the rapid strain ramp described in Section 2.5.1 [36, 51, 59].

At low stresses around the yield stress Σ_y of the material (see Section 2.1), the standard response is that of a strain that increases at an ever-decreasing rate, hence the common term for this protocol 'creep'. In practice, when $\Sigma_0 < \Sigma_y$, the system creeps indefinitely [36, 87, 157]. However, when $\Sigma_0 > \Sigma_y$, this creep regime can end with a failure event in which the strain rate suddenly increases dramatically [9, 19, 28, 36, 51, 110–112].

2.5.3 Creep-Recovery Test

The creep-recovery protocol is the focus of Chapter 6. It has been studied experimentally for a range of amorphous materials [50, 53, 77, 123–125, 140, 141, 190, 191], and modelled theoretically for materials such as cold-set gels and concrete [124, 125].

The creep-recovery test is initially identical to that of the step stress: after any ageing processes, a stress of amplitude Σ_0 is instantaneously applied at $t = 0$ and held constant. However, at a time $t = t_{\text{stop}}$, the stress is switched off, and the system is allowed to relax. The applied stress and a typical strain response are sketched in the bottom panel of Fig. 2.6. The time at which the stress is switched off, t_{stop}, is defined in this work as the time at which the strain reaches $\gamma = \gamma_0 + \Delta\gamma_f$, where γ_0 is the initial strain immediately after the imposition of the step stress, and $\Delta\gamma_f$ is the controlled forward strain. The dependence of t_{stop} on strain allows the control of the amount that the system strains forward under the step stress $\Delta\gamma_f$. The strain recovered after the stress switch-off can then be measured and compared to $\Delta\gamma_f$.

An alternative would be to instead impose a given stress switch-off time t_{stop}, which has been utilised experimentally [123]. However, the results must be presented with some caution, because the amount the system has strained forward $\Delta\gamma_f$ over the fixed time t_{stop} will be different for, say, different values of the imposed step stress Σ_0. This can be managed by plotting the recoverable strain relative to the forward strain $\Delta\gamma_f$, as presented in this work. Either method for defining t_{stop} will produce the same results, provided the change in strain is accounted for.

A typical strain response to this protocol is that, during the step stress, the system creeps forward with a small-scale increasing strain as described in the above section. When the stress is switched off, the strain drops by some amount, and the system begins to relax [123]. The size of the subsequent strain relaxation defines the recoverable strain.

2.6 Stress Diffusion

Stress diffusion is the process through which a localised yield event somewhere in the material affects behaviour elsewhere [192]. This concept was introduced in the SGR model through the noise temperature x in which noise in the system is generated by the propagation of stress from yield events [8, 71, 92] (Section 2.2.1). However, x functions as a temperature and does not explicitly simulate the diffusion of stress from specific yield events. In the absence of non-local stress diffusion, shear banding in systems has been shown to become history dependent and less reproducible with respect to noise [84, 192, 193]. Therefore, it has been suggested that a realistic model depiction of banded flow as strongly inhomogeneous regions should contain stress diffusion [192].

Although there is no exact stress diffusion in the models as described above, there is a diffusive effect from yield events already embedded within the foundations of the models through the force balance described in Section 2.2.2 and Eq. (2.2.7). When an element in a streamline yields, it relaxes its local element strain, causing the streamline visco-elastic stress σ_s, equal to the average element strain on that streamline as in Eq. (2.2.6), to fall. By imposing force balance, as in Eq. (2.2.7) and Eq. (2.2.8), the fall in σ_s causes the streamline strain rate $\dot{\gamma}_s$ to increase. This will in turn cause the other elements in that streamline to experience a larger strain rate, and therefore make them more likely to yield. Hence, the relaxation of stress from the element yielding event propagates through the streamline to other elements. The effect of a changing $\dot{\gamma}_s$ will also affect other streamline strain rates through force balance (Eq. (2.2.7) and Eq. (2.2.8)). However, these diffusion-like processes either affect just one streamline, or all streamlines equally. This means that there is no spatial corelation to the diffusion. Therefore, an explicit stress diffusion should be introduced into the model.

To implement a definitive stress diffusion into the models described above, a stochastic straining of elements is implemented on neighbouring streamlines after each yield event, as seen in other mesoscopic model simulations [24, 177]. Suppose element m on streamline s with local strain $l_{sm} = l^*$ yields, this causes an adjustment in the strain of three randomly chosen elements on each of the adjacent streamlines $s \pm 1$ by $l^* w\,(-1, 2, -1)$. The stress diffusion factor w dictates what fraction of the strain that the yielded element has lost l^* is diffused to these randomly selected elements in neighbouring streamlines.

This 1D approximation of the Eshelby stress propagator couples adjacent streamlines together, meaning heterogeneous shear effects occur in spatially localised regions [160, 194]. Physically, this stress-diffusion term has been compared to the Brownian movement of polymer chains in response to a nearby rearrangement event [192].

2.7 Conclusion

This chapter has introduced the rheological concepts that form the foundation of this work, outlining essential macroscopic variables and shear protocol geometry. It has described the Soft Glassy Rheology (SGR) model, which is the primary simulation tool used in this thesis, where mesoscopic elements strain and yield on streamlines that allow heterogeneity in shear. Finally, it has provided a description of two modifications of the SGR model. The first, a simplification of the energy well landscape which results in a simple Thermal Elasto-Plastic (TEP) model, which can be solved either as a discrete element model or as a Fokker-Planck equation. The second, new to the field, prohibits the reformation of elements, and in doing so becomes a candidate for simulating protein gels. These models form the theoretical base for understanding the behaviour of amorphous materials in this thesis.

Chapter 3

Methodology

3.1 Computational Method

When the mesoscopic models described in Chapter 2 were first introduced, constitutive equations were derived and solved analytically [71, 92]. More recently, hopping algorithms have been introduced [13, 24, 25, 81] to solve the equations numerically. The details of the computational methods used in this thesis are outlined below.

3.1.1 Ageing and Annealing

Ageing in the SGR model is simulated as follows. Before the material is subject to any strain, it is allowed to age undisturbed for a waiting time t_w. The sample is initialised at $t = -t_\mathrm{w}$ as a fresh sample by process of a 'deep quench', meaning the distribution of element trap depth energies E corresponds to the prior distribution $\rho_0(E)$ of Eq. (2.2.1). It is further assumed that all element strains are equal to zero $l_{sm} = 0 \ \forall \ m, s$ [81]. The distribution of trap depth energies E for a freshly prepared $(t_\mathrm{w} = 0)$ sample can be seen in the dark blue line at the left of the top panel of Fig. 3.1 which shows the distribution of element energy well depths $P(E)$, equal to the prior distribution $\rho_0(E)$.

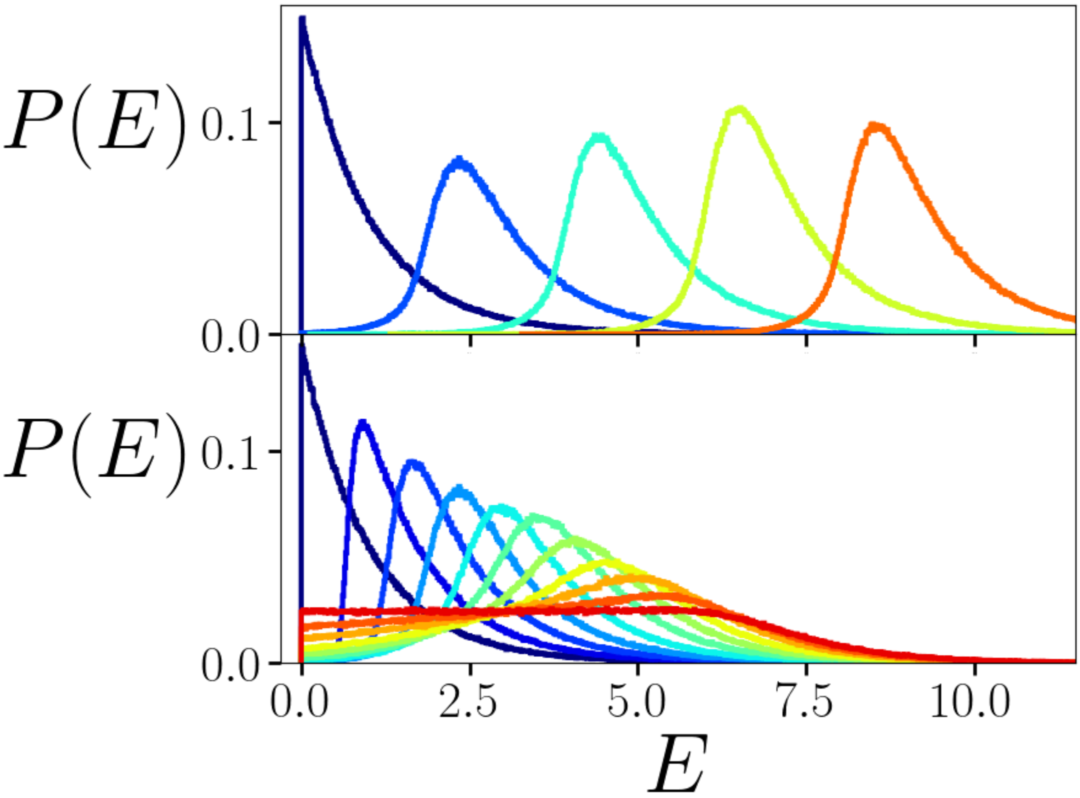

Figure 3.1: The normalised distribution $P(E)$ of element trap depth energies E after waiting time t_{w} at noise temperature x in the SGR model. The dark blue lines on the left represent a distribution equal to the prior distribution $\rho_0(E)$ of Eq. (2.2.1).
Top panel: At fixed noise temperature $x = 0.3$ and a range of waiting times $t_{\mathrm{w}} = [0, 10^3, 10^6, 10^9, 10^{12}]$ (from dark blue to orange or left to right). Note that the average trap depth energy increases with increasing t_{w}.
Bottom panel: At fixed waiting time $t_{\mathrm{w}} = 10^3$ and a range of noise temperatures $x = [0.0, 0.1, ..., 1.0]$ (from dark blue to red or tall function to flat function). Note that the distribution of trap depth energies becomes broader with increasing x.

Throughout the ageing process, for time $-t_{\mathrm{w}} < t < 0$ the system experiences no imposed stress or strain but its elements are still able to hop between traps through mechanical noise activation, as modelled via the effective noise temperature x in Eq. (2.2.3). Note the choice of starting time $t = -t_{\mathrm{w}}$ is defined such that the shear protocol begins at $t = 0$.

To implement the ageing described above, a Waiting Time Monte Carlo (WTMC) algorithm [195–198] is used to predict when a particular element will next yield [13, 24, 25]. The time at which the element will next yield, the yielding time t_Y, is stochastically chosen from the distribution

$$Y(t_Y) = \exp\left[-r(E,0)t_Y\right] , \tag{3.1.1}$$

which depends on the yielding rate $r(E_{sm}, l_{sm})$ in Eq. (2.2.3) at zero element strain $l_{sm} = 0$. Recall that $r(E_{sm}, 0) \propto \exp(-E_{sm}/x)$ in Eq.(2.2.3), meaning an element with a larger value of E_{sm} has a smaller yielding rate during ageing $r(E_{sm}, 0)$. Therefore, through Eq. (3.1.1), a larger trap depth energy E_{sm} also implies a longer yielding time t_Y.

Once the element's yielding time has been calculated, the algorithm then skips to this time, yields the element and gives it a new energy well E_{sm} selected from the prior distribution $\rho_0(E)$. It then uses Eq. (3.1.1) again to select its next yielding time with its new energy well E_{sm}. This process is repeated until the total elapsed time for ageing is equal to the waiting time t_{w}. Note that it is possible to treat elements independently during the ageing process, because there is no consequence of element yield events on surrounding elements as all element strains are zero $l_{sm} = 0$.

In practice, this means that for longer waiting times t_{w} the elements will, on average, have evolved into deeper traps. Recalling that elements in deeper traps have a lower probability of yielding per unit time when experiencing a certain strain, as in Eq. (2.2.3), the longer the material is given to age, the more solid-like the material [13, 23, 83, 93]. It can also be considered as increasing the average relaxation time within the systems, reflecting annealing in metallic glasses [169,170] or increased connectivity in polymer melts [66]. The increase in average element energy well depth with increasing waiting time t_{w} is shown in the top panel of Fig. 3.1.

Because the yielding rate also depends on the noise temperature $r(E_{sm}, l_{sm}) \propto \exp(-1/x)$, as in Eq.(2.2.3), the ageing process will also depend on x. This can be seen in the bottom panel of Fig. 3.1, where the distribution of energy well depths $P(E)$ after a fixed waiting time $t_{\mathrm{w}} = 10^3$ is shown for a range of noise temperatures x. It can be seen that the distribution of energy depths $P(E)$ spreads out as the noise temperature x increases. The extreme of this behaviour is at the largest temperature $x = 1.0$, where $P(E)$ is almost an even distribution between $0 < E \lesssim 8$. The large temperature allows the elements to explore the full energy well landscape during ageing.

At the opposite extreme of zero noise temperature $x = 0$, the prior distribution $\rho_0(E)$ of Eq. (2.2.1) is obtained. This is because all elements have zero strain during ageing $l_{sm} = 0 \; \forall \; m, s$, and the yielding rate goes to zero $r(E_{sm}, 0) \propto \exp(-1/x) \to 0$ as $x \to 0$. Therefore, at $x = 0$, no yield events happen during ageing, and consequently no ageing occurs, regardless of the waiting time t_{w}. The athermal limit $x = 0$ will be discussed further in Section 3.1.4.

Note that this ageing process relies on elements yielding and reforming. When setting the timescale for reformation to infinity $\tau_{\mathrm{reform}} = \infty$ as in the gel modification of the SGR model described in Section 2.4, this ageing process will actually result in a weaker material. This is because as elements yield at their yielding time t_Y they will not reform with a new energy well and will instead be permanently broken. For this reason, during the ageing process the timescale for reformation is always set to zero $\tau_{\mathrm{reform}}(t < 0) = 0$. Though this results in a discontinuous change in τ_{reform} when the shear protocol starts at $t = 0$, the process of forming gels can be extremely complicated and also specific to the type of gel [28,53,59,112,120,131,153,157]. In keeping the standard ageing process found in the SGR model, the model maintains its generality to apply to all low-density gels, and also keeps the focus on what happens to the materials after ageing when under shear. Exploring how to simulate the gelation process in mesoscopic models deserves its own study.

Where the annealing of a material is pre-imposed by a variable, as with the pre-shear equilibrium temperature x_0 in the TEP model described in Section 2.3, there is no need to go through the ageing process [103, 104, 171]. Instead, the material is initialised at $t = 0$ with the Gaussian strain distribution $P_0(l)$ given by Eq. (2.3), with width defined by the pre-shear equilibrium temperature x_0, and then subsequently simulated at working temperature x. This can be considered physically as a material initially equilibrated at a temperature represented by x_0, causing a distribution of strains within the material. The system is then suddenly quenched to the working temperature x at $t = 0$ and the shearing protocol is started. Note that a smaller value of x_0 corresponds to a better annealed system, because this results in a more consistent distribution of strains. Because of the difference in process between the ageing and annealing in the SGR and TEP models, the parameters x_0 and t_{w} are only loosely comparable.

The process of implementing ageing and annealing experimentally depends on the material. For example, the degree of annealing can be tuned for metallic glasses [48, 169–171], but is more difficult to vary for softer materials such as emulsions [48]. Other studies have replicated the waiting time t_{w} described above, by allowing a microgel to relax for a given time t_{w} after pre-shearing [51]. Ageing can also be considered comparable to system connectivity, an important parameter in polymeric materials [53, 66, 157].

The theoretical work in this study is intended to model a range of systems, from entangled polymers to densely packed colloidal particles [9]. Therefore, to produce predictions for this wide span of materials the models used must be highly generic. The ageing and annealing processes in this work are consequently oversimplifications of a complex and diverse process [13, 24, 71, 81, 92]. However, these models have shown great success in simulating the behaviour of a range of amorphous materials under shear, with the ageing and annealing described above well established in the literature [13, 24, 25, 103, 104, 171]. The work in this thesis will focus primarily on material behaviour under shear, with the degree of ageing or annealing an influencing variable.

3.1.2 Seeding Shear Heterogeneity

As discussed in Chapter 1, shear banding corresponds to heterogeneous flow behaviour within the material, with varying shear rates across the flow gradient direction y_{axis}. In experimental studies, banding is seeded by disorder and noise within the material. These instabilities within the system then become amplified by the imposition of shearing, resulting in shear banding [11, 67, 112, 199, 200]. In theoretical studies, this disorder is partly modelled through stochastic processes, where the random probabilities inherent to the model cause a variance in streamlines across the flow-gradient direction y_{axis}. However, in the limit of a large number of elements per streamline $M \to \infty$ (further discussion on the choice of M can be found in Section 3.2), the average behaviour of elements across streamlines becomes uniform. Consequently, the stochastic nature of the simulations is nullified by averaging over a large number of elements.

Therefore, in this regime of large M, an additional contribution is required to model the initial disorder inherent to amorphous materials. This takes the form of a perturbation that seeds shear heterogeneity within the material. Options in the existing literature include perturbing the initial visco-elastic stress of each element l_{sm} [24, 172], or the waiting time t_{w} [25, 87]. The effect of the two methods is similar. Therefore, where the waiting time is a relevant parameter, as in the SGR model and its extensions, this work will follow the latter example. The waiting time t_{w} is perturbed across the flow-gradient of the material, such that the waiting time that elements on streamline s experience, is given by

$$t_{\text{w}s} = t_{\text{w}} \left[1 + \epsilon \cos\left(2\pi s \Delta_y\right)\right] . \tag{3.1.2}$$

The strength of the perturbation is represented by ϵ, which determines what fraction of the overall waiting time t_{w} is added/removed as a perturbation. The consequence of this perturbation is that, prior to the application of the shear protocol, some streamlines are better aged than others. This creates an intrinsic heterogeneity in the element energy depth distributions between streamlines which will provide the initial seed for the formation of shear bands. The visual representation of the effect of Eq. 3.1.2 on t_{ws} can be found in Fig. 3.2.

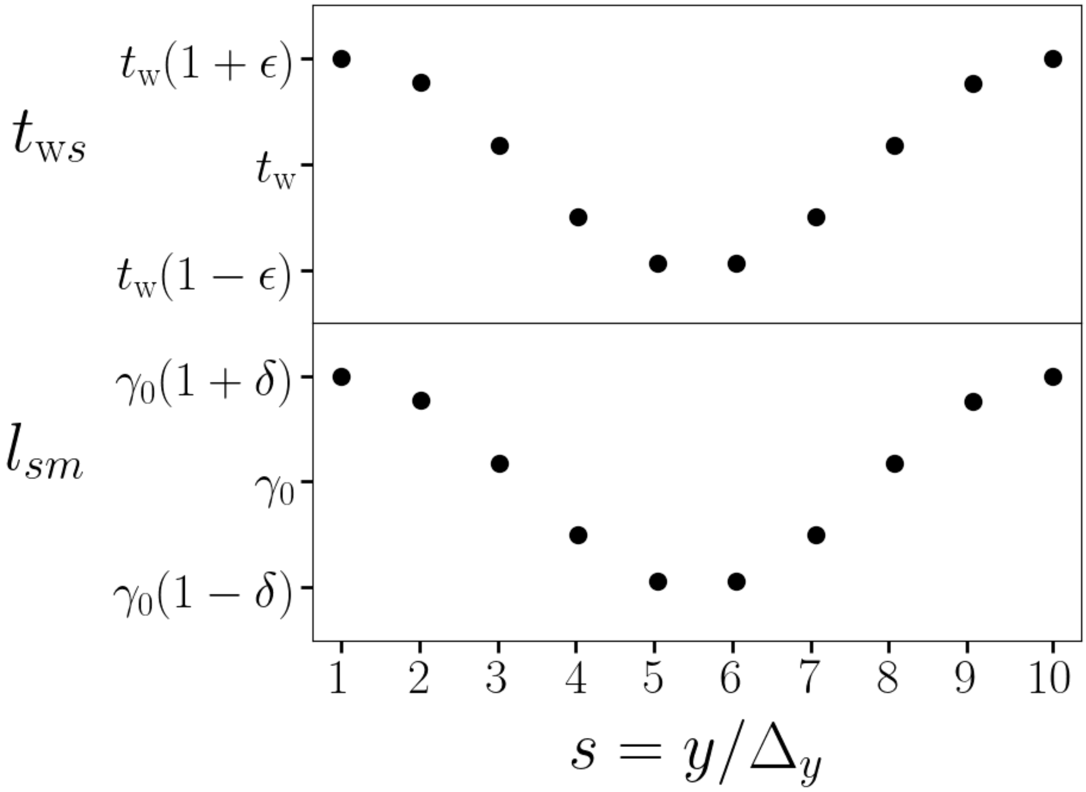

Figure 3.2: **Top panel**: The perturbed streamline waiting time $t_{\mathrm{w}s}$ as a function of the streamline number s for total number of streamlines $S = 10$, as specified by Eq. (3.1.2). **Bottom panel**: The perturbed element strain l_{sm} as a function of the streamline number s for total number of streamlines $S = 10$, as specified by Eq. (3.1.3).

Alternatively, in simulations where t_{w} is not a relevant parameter, as in the TEP model, the initial visco-elastic stress of each element l_{sm} is perturbed instead. This is implemented in a similar way

$$l_{sm} = \gamma_0 \left[1 + \delta \cos\left(2\pi s \Delta_y\right)\right] \,, \tag{3.1.3}$$

where the size of the perturbation is given by the strain heterogeneity factor δ, which determines what fraction of the initial strain γ_0 is added/removed as a perturbation. There is no element m dependency in Eq. (3.1.3), so all elements on a streamline will have their local strain perturbed by the same value. This creates an intrinsic heterogeneity in the average element strain between streamlines, which will provide an initial small seed for the formation of shear bands. Note that this perturbation is in addition to the Gaussian initialisation of the element strain in the TEP model, outlined in Eq. (2.3.1), which is used to model the effect of annealing rather than to seed the formation of shear bands. The perturbation in Eq. (3.1.3) effectively shifts the centre of this Gaussian for different streamlines.

In physical terms, the perturbations just discussed are intended to model the thermal and mechanical noise of an experimental sample. There are many circumstances under which real samples are seeded with intrinsic heterogeneities, such as in imperfections in rheometer devices or residual defects that remain following sample preparation [67]. Indeed, the importance of sample preparation on behaviour under shear is gaining recognition in the literature [161, 201–203], and these perturbations (along with their associated ageing processes) show how variations in sample preparation can be modelled theoretically.

3.1.3 Simulating Shear

Fixed Timestep

The simulations in this thesis use a time discretisation method during the imposition of shear, after the initial ageing. For a fixed timestep, the time during which measurements are taken $0 < t < t_{\text{end}}$ is discretised into N timesteps, each of length Δt. At each timestep the relevant model dynamics are implemented, determining which elements yield and what effect that has on the rheological properties of the material.

For the element-based algorithms, this involves the following processes:

(i) Implementing the elastic straining of elements by their streamline's strain rate $\dot{l}_{sm} = \dot{\gamma}_s$ using the explicit Euler Method $l_{sm}\,(t + \Delta t) = l_{sm}\,(t) + \dot{\gamma}_s \Delta t$ [67, 204].

(ii) Deciding which elements yield using a random number generator and the probability of yielding p in Eq. (2.2.3). If a random number R, selected from a top hat distribution between $0 < R < 1$, is smaller than p for a given element, then that element yields. The stress diffusion from the yield event described in Section 2.6 is implemented. The element then reforms on the timescale for reformation τ_{reform}. If the model contains a distribution of energy wells E, the element transitions to a new energy well when it reforms, randomly chosen from the prior distribution $\rho_0(E)$ of Eq. (2.2.1). Otherwise, the element hops to a well with identical energy depth to its previous well. This process is then repeated for all elements.

(iii) Evaluating the subsequent element/streamline/material stresses and strain rates through force balance, as discussed in Section 2.2. The total and streamline visco-elastic stresses are calculated using Eq. (2.2.6), and the strain rates using Eq. (2.2.8). The macroscopic stress or strain rate can then be calculated using Eq. (2.2.5). When viscosity is zero $\eta = 0$, the macroscopic strain rate is instead given by Eq. (2.2.9).

The time is then advanced by Δt and the process is repeated.

For the Fokker-Planck equation solution to the TEP model described in Section 2.3.2, the distribution of the element strains on a streamline $P(l_{sm})$ is modelled as a probability density function of the strain of that streamline $P(l_{sm}) \simeq P_s(l)$ in strain space l. Numerically, a change of variables to the co-shearing frame can be used $l = \tilde{l} + \gamma_s$, which effectively centres the strain space l on the average strain for that streamline. The differential equations are then solved by discretising the strain space on a grid of M values of l, spaced linearly between $l = -l_{\text{max}}$ and $l = +l_{\text{max}}$. The value of l_{max} is chosen to be large enough such that the entire strain distribution $P(l)$ is encompassed.

The simulation per timestep then involves the following processes:

(i) Implementing the Fokker-Planck equation in Eq. (2.3.3) using the explicit Euler Method $P_s(l, t + \Delta t) = P_s(l, t) + \frac{dP_s(l,t)}{dt}\Delta t$ [67, 204].

(ii) Evaluating the average yielding rate Y_s, visco-elastic stress σ_s, and strain rate for each streamline using Eqs. (2.3.4), (2.3.5) and (2.2.8). The macroscopic stress or strain rate can then be calculated using Eq. (2.2.5).

The time is then advanced by Δt and the process is repeated.

Adaptive Timestep

It is possible to simulate the systems studied in this thesis using an adaptive timestep [13, 24, 25]. This features a similar concept to that used during ageing, discussed in Section 3.1.1, where time during which no yielding is predicted can be skipped to improve efficiency. However, a Waiting Time Monte Carlo algorithm like that used for ageing, which considers each element individually for the whole time, is not appropriate under shear, as yield events of elements with non-zero strain will affect the predicted yielding time of other elements. Instead, the average predicted yielding time over all elements must be calculated

$$\Delta t_{\text{ad}} = \Delta t / r_{\text{av}} \, , \qquad\qquad r_{\text{av}} = \frac{1}{M} \sum_m r(E_m, l_m) \, , \tag{3.1.4}$$

where r_{av} is the average yielding rate over the entire system.

At the end of each time iteration, the new timestep Δt_{ad} is calculated using Eq. (3.1.4), and it is by that timestep that time is advanced before the process repeats. Aside from this change, all calculations follow the steps provided for the fixed timestep. Using an adaptive timestep is more computationally efficient [13, 24, 25], but can produce inaccuracies when modelling the short timescales introduced by heterogeneous flows [197, 198]. For this reason, an adaptive timestep will only be used in this thesis when shear homogeneity is enforced.

3.1.4 Athermal Limit

The SGR and TEP models presented here are both thermal models, in the sense of having thermally activated hopping of elements between energy wells. The original interpretation of the origin of the working temperature x in the SGR model was in noise from other rearrangements, but it acts as an effective temperature [13, 24, 71, 81, 92]. In practice, the working temperature x is modelled in the same way for all simulations in this thesis, through Eq. (2.2.3). It is possible to explore the athermal limit of these models by taking $x \to 0$ [70, 94, 101, 177, 203].

The probability of yielding p in Eq. (2.2.3), when evaluated at $x = 0$, becomes a step function [8, 9]

$$p(E_m, l_m) = r(E_m, l_m)\Delta t = \begin{cases} 0, & \text{if } E_{\text{el}}(l_m) < E_m \\ \Gamma_0 \Delta t, & \text{if } E_{\text{el}}(l_m) > E_m \end{cases} . \tag{3.1.5}$$

The work in this thesis predominantly simulates thermal systems, with some exploration of the athermal limit.

3.2 Parameter Values

As in almost all studies that utilise the SGR model [13,23–25,71,81,92], this work will choose, without loss of generality, units of length, time and stress in which $L_y = 1$, $\Gamma_0 = 1$ and $k = 1$. In addition, the glass transition temperature is given as $x_g = 1$. Although these choices are purely a matter of convention [24, 71, 81, 172], the choice should be kept in mind when interpreting results and is the reason why all reported quantities are dimensionless. This means that the element strain l is defined in such a way that an element, drawn at random from the prior distribution, will yield at strains of order one on timescales of order one. It is therefore important to acknowledge that where key behaviour occurs at strains of a certain scale, this is relative to the material specific element strain, which the model does not specifcy [71, 81].

Any numerical results obtained with the fixed timestep method described in Section 3.1.3 should be converged to the limit of $\Delta t \to 0$. Likewise, results should also be converged with increasing number of elements $M \to \infty$, or equivalently with increasing number of discretisation points in strain space in the continuum version $M \to \infty$, as described in Section 2.3.2. Indeed, the adaptive timestep method described in Section 3.1.3 should also be converged with the variation of its minimum Δt. These true limits are of course not computationally achievable, but efforts have been made to ensure that the results presented in this thesis are as accurate as possible within computational limits. To that end, the following parameters have been used:

- The numerical time discretisation step is set to $\Delta t = 0.01$.
- The number of discretisation points in strain space is set to $M = 10^5$.
- The number of elements per streamline is set to $M = 10^5$.

As outlined in Appendix A, simulations with $\Delta t = 0.005$ and $M = 10^6$ produced negligibly more accurate results, verifying good convergence with respect to these quantities.

As mentioned previously, in the limit of large M, heterogeneity in shear between streamlines arising from stochasticity is lost, and a perturbation must be implemented to seed heterogeneity. This process is described in Section 3.1.2, where the perturbation size is defined by ϵ or δ. Small amplitudes of $\epsilon = 0.1$ and $\delta = 0.05$ were chosen, similar to values in the literature [25, 87, 91, 176].

Convergence analysis also found that the difference in measurement errors between number of streamlines $S = 10$ and $S = 100$ simulations is effectively negligible, and therefore for computational ease $S = 10$ was chosen.

3.3 Measured Quantities

3.3.1 Macroscopic Variables

The most common quantity that is measured in rheological studies is the macroscopic rheological variable. This will depend on the imposed protocol:

(i) For protocols that impose a strain, such as step strain, the subsequent evolution of the stress Σ is measured.

(ii) For protocols that impose a stress, such as step stress and the creep-recovery test, the subsequent evolution of the strain γ, or the time-differential of this quantity, the strain rate $\dot{\gamma}$, is measured.

These measurements form the foundation of most studies in rheology, recordable both experimentally and computationally, and give a clear overview of the overall behaviour of the material over time.

3.3.2 Degree of Banding

One of the advantages of computational simulations is the ability to look inside the system and take mesoscopic measurements that may be difficult to achieve experimentally. Experimental practice has made significant advances in recent years with techniques such as ultrasonic imaging [27, 110], confocal microscopy [30, 205], and light scattering [72, 112, 206, 207]. Simulation results that look at internal system behaviour can help understand the results provided by these techniques. The mesoscopic models used in this work have the ability to describe the element behaviour within the material. In particular, simulations can track the degree to which the flow or deformation profile is shear banded across the flow gradient direction y_{axis}. One of the common ways of doing this is to measure the standard deviation of the strain and strain rate across the flow-gradient y_{axis} direction

$$\Delta\gamma(t) = \sqrt{\frac{1}{S}\sum_{s=0}^{S}\left(\gamma_s(t) - \gamma(t)\right)^2}\,, \tag{3.3.1}$$

$$\Delta\dot{\gamma}(t) = \sqrt{\frac{1}{S}\sum_{s=0}^{S}\left(\dot{\gamma}_s(t) - \dot{\gamma}(t)\right)^2}\,, \tag{3.3.2}$$

where $\gamma_0(t)$ and $\dot{\gamma_0}(t)$ represent the average strain and strain rate across the material at time t. These quantities report how far away, on average, from the macroscopic strain γ and strain rate $\dot{\gamma}$ the individual streamline strains γ_s and strain rates $\dot{\gamma_s}$ are. In doing so, they effectively measure the degree of strain and strain rate banding across the sample, and allow the locating, analysing and quantifying of the shear banding process.

3.3.3 Displacement Profile

It is possible to visualise the shear banding process by looking at the intrinsic behaviour of the material across the shear profile over time. This can be done by utilising the integral of the strain with respect to the distance along the flow gradient direction

$$U(y,t) = \int \gamma\, dy = \iint \dot{\gamma}\, dt\, dy\,, \tag{3.3.3}$$

where $y = s\Delta_y = sL_y/S$ is the distance along the flow gradient direction y_{axis}. This gives the profile of the displacement across the flow-gradient direction y_{axis}, equal to the velocity profile integrated over time.

3.3.4 Yielding Integral

As mentioned in Sections 2.2.3 and 2.3.2, the rate of yielding in the system, represented by the last component in Eq. (2.3.3), is equal to the average of the yielding rate function $r(l)$ across the strain distribution $P(l)$. This is also true when defined in terms of elements $P(E_m, l_m)$, even when they have different energy wells E_m and therefore different yielding functions $r(E_m, l_m)$.

For this reason, the yielding integral can be used to study the yielding within the simulations:

$$I = \int r(l)P(l)l\, dl\,, \tag{3.3.4}$$

where the integral is taken over the strain space l. This integral measures the average strain relaxation across the system caused by yielding by taking the overlap of $P(l)$ and $r(l)$, given by the multiplication of the two functions, and taking the average value integral over the strain space l.

Alternatively, in terms of elements, the integral can be considered as a summation:

$$I = \frac{1}{M}\sum_{m} r(E_m, l_m)l_m\,, \tag{3.3.5}$$

where the summation is taken over all elements $m = 1 \dots M$.

This is an important variable in understanding how systems yield, and will be used to analyse the quantity of strain relaxation occurring in the system at different times. Recall that, in all the models introduced in Chapter 2, material behaviour is dictated by two processes: elastic straining and plastic yield events. Without plasticity, the system would simply behave as an elastic solid as described in Section 2.1. It is the localised yielding in the system that gives amorphous materials complex behavioural properties [8, 9, 49, 62]. The yielding integral I quantifies the strain relaxation from these local yield events, and therefore provides a measure of the yielding that dictates material behaviour.

3.4 Conclusion

This chapter has outlined how the theoretical models used in this work can be implemented computationally to simulate amorphous materials. It has described in detail the simulation algorithms, from pre-shear ageing to the application of a perturbation to seed shear heterogeneity to the calculations under shear. Finally, the parameter input and measurement output variables were discussed, summarising how the simulations presented are initialised, and also how they are subsequently analysed. The contents of this chapter, combined with the theoretical understanding provided by Chapter 2, should provide the reader with all the requisite knowledge to understand and interpret the following results chapters.

Chapter 4

Delayed Shear Banding and Material Failure After Imposition of Step Strain

4.1 Introduction

This chapter studies the behaviour of amorphous materials under the step strain protocol outlined in Section 2.5.1. In particular, there will be a focus on the occurrence of a delayed dramatic shear banding instability causing material failure, a long time after the initial imposition of the strain.

The work presented here can be found in a pre-print [188], which features alongside work done by Emily Carrington on a Fluidity Model under step strain. Also in the publication is work completed by the author during his Masters year at Durham University under the supervision of Prof. Suzanne Fielding, which also has a pre-print [91]. That work explored the how the time and degree of banding varies with the age of the material in the Soft Glassy Rheology (SGR) model. No work completed during that time features in this chapter, but references will be made to it due to the connections between the two studies.

Shear banding, as outlined in Chapter 1, has been widely studied, both experimentally [3,8–11,36–38] and theoretically [9,13,23,25,47,87], and has been shown to result in the failure of a range of amorphous materials [8–11, 84–86, 90]. The occurrence of this shear localisation phenomenon has been studied under protocols such as shear startup (where a constant strain rate $\dot{\gamma}_0$ is applied) [9, 67, 71, 87], step stress (where a constant stress Σ_0 is applied) [9, 11, 25, 28, 36, 81, 87, 107–109, 112–116], and cyclically repeating shear (where an oscillating strain $\gamma = \gamma_0 \cos(\omega t)$ or stress $\Sigma = \Sigma_0 \cos(\omega t)$ is applied) [41, 159, 208–211]. Generally, a shear localisation instability involves the build-up of plastic yield events during the imposed shear, which eventually avalanche into shear banding and material failure [9, 11, 28, 36, 67, 70, 71, 87, 110, 111, 171, 212]. In shear startup, the stress tends to initially increase linearly with time before the system fluidises to a steady state stress. The stress can overshoot the steady state stress before fluidisation [9, 11, 71], and it has been predicted through linear stability analysis that the occurrence of shear banding between the overshoot and the steady state may occur generically [67, 87]. Under step stress, a protocol which will be explored in detail in Chapter 5, shear banding during failure is also well established [9, 28, 36, 110, 111]. Delayed shear banding has also been studied under oscillatory shear protocols, where changing the protocol parameters can significantly affect the delay time [70, 171, 212], similar to behaviour seen in the step strain protocol in this work.

Step strain is a less commonly studied protocol than those described above. It has been studied within the SGR model, but only with enforced shear homogeneity which is unable to simulate shear banding [71, 81]. Other theoretical studies have explored shear rate heterogeneity during stress relaxation after a step strain similar to that found in this work [67, 69, 87, 213]. However, these studied generally focus on the appearance of banding within short timescales in contrast to the highly delayed banding found in this work. Experimental studies into the step strain protocol, through the ‘rapid strain ramp’ discussed in Section 2.5.1 [185, 186], can be found in polymer melts [65, 66, 185–187], where again the focus is generally on short timescale banding that arises almost immediately after the application of the step strain. One of these studies found that the banding could be delayed, creating experimental results comparable to those presented here [66]. This study also discussed the need for a physical model based on yielding to describe the effect, which the work here presents, because the tube theory generally associated with polymer melts is unable to provide a full description of the delayed physics [66]. In addition, one experimental study on hydrogels has found preliminary evidence for the highly delayed fracture under step strain outlined in this work [214]. However, the step strain protocol remains generally less explored in the literature than other protocols, a situation which this work hopes to motivate to change.

Given the absence of any final flowing state (as in shear startup) or repeating strain (as in oscillatory shear) in the step strain scenario, it has perhaps been assumed that stress relaxation after the imposition of strain will take place in an uncomplicated way, with the material slowly returning to a homogeneous relaxed state. On the contrary, the central contribution of this work will be to show that, for a range of parameters, an amorphous material will instead suffer a dramatic internal shear banding instability. The strain field suddenly becomes highly heterogeneous across the flow-gradient, leading to a precipitous stress drop and catastrophic material failure. Crucially, this instability can be delayed for an arbitrarily long time through changes to the protocol and system.

The finding of catastrophic material failure arising at a potentially indefinitely long time after a material was last (externally) deformed is somewhat counter-intuitive. Indeed, an observer lacking knowledge of the strain history could not predict the occurrence of this instability, with far reaching consequences for material processing and performance [158]. This could have implications for the manufacture and use of the wide range of amorphous materials that can be simulated with these models, such as condiments, gels and clays [3, 9, 13, 23–25, 37, 71, 92]. This research aims to predict and explore theoretically how this failure occurs in amorphous materials under the step strain protocol, and motivate further experiments to test these conclusions.

All results presented in this section are from simulations using the Thermal Elasto-Plastic (TEP) model and the Soft Glassy Rheology (SGR) model, outlined in Sections 2.3 and 2.2 respectively. They are simple mesoscopic models, which use the straining and yielding of elements to simulate the physics of amorphous materials. To provide an understanding of the key physics at play, the shear banding discovered will be analysed through the bulk rheological properties and internal strain fields that can be computed in these simulations. These measured properties are:

- The bulk shear stress Σ response to the strain-controlled protocol.
- The standard deviation in the strain across the system $\Delta\gamma$. This is a measure of the scale of the heterogeneity in the strain field $\gamma(y)$ across the shear-gradient direction y_{axis}, and effectively measures the magnitude of strain banding across the system. This value is only non-zero when heterogeneity in shear is allowed, or equivalently, when the number of streamlines $S > 1$, see Section 2.2.2.
- The displacement profile $U(y)$, equal to the integral of the strain $\gamma(y)$ along the shear-gradient direction y_{axis}, which gives a visual representation of the internal state of the material.

There will also be some discussion, when analysing the TEP model results, on how the distribution $P(l)$ of local element strains l interacts with the yielding rate function $r(l)$, parameters described in Section 2.3.2.

These measurements will be explored as a function of the relevant input parameters for these models under the step strain protocol, which are as follows:

- The amplitude of the imposed step strain γ_0.
- The age of the material, or the extent of annealing. Defined by the waiting time t_{w} in the SGR model and the pre-shear equilibrium temperature x_0 in the TEP model.

- The working temperature of the system x, generally called the noise temperature in the SGR model and the post-shear equilibrium temperature in the TEP model, but implemented in the same way.

Unless specified otherwise, the following parameter values will be applied across all the simulations in this chapter:

- Working temperature $x = 0.01$ in the TEP model and $x = 0.3$ in the SGR model.
- Number of streamlines $S = 10$ when heterogeneity across the flow gradient is allowed, and $S = 1$ when homogeneity is enforced.
- Solvent viscosity $\eta = 0.05$.
- Perturbation size, $s_{het} = 0.05$ in the TEP model (where the element strain l is perturbed) and $\epsilon = 0.1$ in the SGR model (where the waiting time t_{w} is perturbed).
- Numerical time step $\Delta t = 0.01$.
- Range of element strains from $l_{\min} = -10.0$ to $l_{\max} = 10.0$ (TEP model only).
- Number of discretisation points in strain space $M = 10^5$ (TEP model only).
- Number of elements per streamline $M = 10^5$ (SGR model only).

All of the parameters listed above are explained in more detail in Chapter 3.

The TEP model for $x > 0$ is discussed first in Section 4.2, followed by a discussion in the athermal ($x = 0$) limit in Section 4.2.6. A comparison of these findings to results obtained for the SGR Model, additional to those in [91], will be explored in Section 4.3. The chapter will finish with some concluding remarks and comments on avenues for future work in Section 4.4. This project shows the generality and strength of the conclusions reached previously by the author within the protocol of step strain [91]. It also expands on that work by exploring a much larger parameter space, most notably the variation in behaviour with temperature and magnitude of imposed strain. This research finds that an amorphous material, subject to an imposed step strain protocol, can exhibit catastrophic banding, a long delay time after the initial strain imposition.

4.2 The Thermal Elasto-Plastic Model

4.2.1 Stress Decay and Strain Response

The step strain protocol, in which a strain of amplitude γ_0 is applied and held constant, was simulated within the TEP model, solved using the Fokker-Planck method as outlined in Section 2.3.2. Results for a fixed strain amplitude $\gamma_0 = 1.2$ and a range of preshear equilibrium temperatures $x_0 = [0.01, ..., 0.02]$ are plotted in Fig. 4.1.

The measured stress decay Σ is plotted in the top panel of Fig. 4.1. The solid lines show the results of calculations in which the strain field $\gamma(y)$ is allowed to become heterogeneous across the shear-gradient direction y_{axis}. The dashed lines show the results of calculations in which it is artificially constrained to remain homogeneous, $\gamma(y) = \gamma_0$, independent of y. The stress at $t = 0$ is equal to the imposed step strain $\Sigma(t = 0) = \Sigma_0 = \gamma_0 = 1.2$, because the material displays purely elastic behaviour at the instant the strain is imposed (where $\Sigma_0 = G_0\gamma_0$ and $G_0 = 1$ in this work). The stress decay is then extremely slow for some time, before a deviation occurs between the behaviour of the model with allowed shear heterogeneity ($S = 10$ - solid lines), where stress drops dramatically, and that with enforced homogeneity ($S = 1$ - dashed lines), where stress continues to decay slowly. The shape of this stress decay closely corresponds with that in the aforementioned experimental discovery of delayed fracture in a hydrogel after the imposition of a step strain [214]. This sudden drop in stress indicates the formation of shear bands.

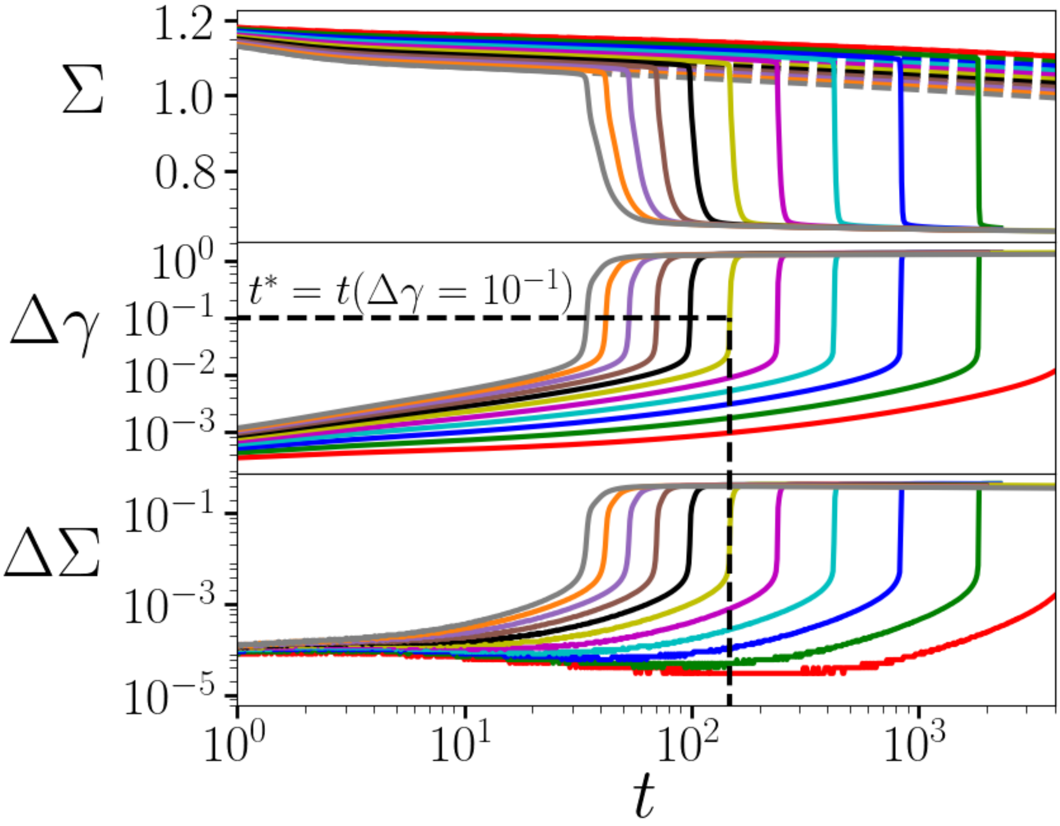

Figure 4.1: **Top panel**: Stress decay Σ as a function of time t after the imposition of a step strain of amplitude $\gamma_0 = 1.2$, as simulated within the Thermal Elasto-Plastic model, for a range of pre-shear equilibrium temperatures x_0=[0.02, 0.019, ..., 0.01] (in order from grey to red or left to right in the sudden stress drop). Simulations with allowed shear heterogeneity ($S = 10$ - solid lines) as well as with enforced homogeneity ($S = 1$ - dashed lines) are shown.
Middle panel: Standard deviation in the strain across the sample $\Delta\gamma$, as a function of time. This measures the degree to which the sample is strain banding. The banding time t^*, defined as the time where the strain standard deviation reaches the value $\Delta\gamma = 0.1$, is highlighted.
Bottom panel: The size of the stress difference between the homogeneous and heterogeneous simulations $\Delta\Sigma$ as a function of time.
Key result: Dramatic drop in Σ and increase in $\Delta\gamma$ and $\Delta\Sigma$ implies a delayed banding event after the imposition of a step strain.

The presence of shear banding in this work is confirmed by the response of the standard deviation in the strain $\Delta\gamma$ (effectively measuring the degree of strain banding across the sample) for the simulations with heterogeneity allowed, plotted in the middle panel of Fig. 4.1, which rises sharply during this stress drop. The bottom panel of Fig. 4.1 plots another measure of the magnitude of shear banding $\Delta\Sigma$, equal to the size of the stress difference between the homogeneous and heterogeneous simulations. This value also rises sharply during the stress drop.

Fig. 4.2 provides further evidence for the presence of shear banding. It plots the displacement profile $U(y)$ (see Section 3.3.3) for a single simulation in Fig. 4.1 at different values of time t since the step strain was applied. At the start of the simulation (the dark blue line), the displacement profile is homogeneous: a straight line between $U(0) = 0$ and $U(L_y) = U(1) = \gamma_0 = 1.2$. By the end of the simulation (the dark red line) the profile is highly heterogeneous, evidence of a catastrophic shear banding instability. Therefore, the formation of shear bands in amorphous materials under step strain is predicted in the TEP model, as predicted within the SGR model in previous work by the author [91].

The shape of this localised heterogeneity in Fig. 4.2 is a consequence of the shape of the small perturbation used to seed heterogeneity at the start of the simulations, outlined in Section 3.1.2. In the TEP model, the initial element strains are perturbed by a cosine function across streamlines (along the flow gradient direction y_{axis}), as in Fig. 3.2. This means that the elements in the streamlines on the edge of the material are on average further strained than those in the middle. This creates an increased probability that the banding will occur on the edge of the material, as it does in Fig. 4.2. The shape of this banding is similar to that seen in a polymer melt when banding under the application of a step strain [65], and can also be seen in simulations of short timescale banding under step strain [69]. The form of the banding in Fig. 4.2 is reminiscent of wall slip, where the failure of the material occurs at the point of contact between the rheometer wall and the material. Although wall slip is an important consideration in experimental studies [11,66,157,158], this model does not

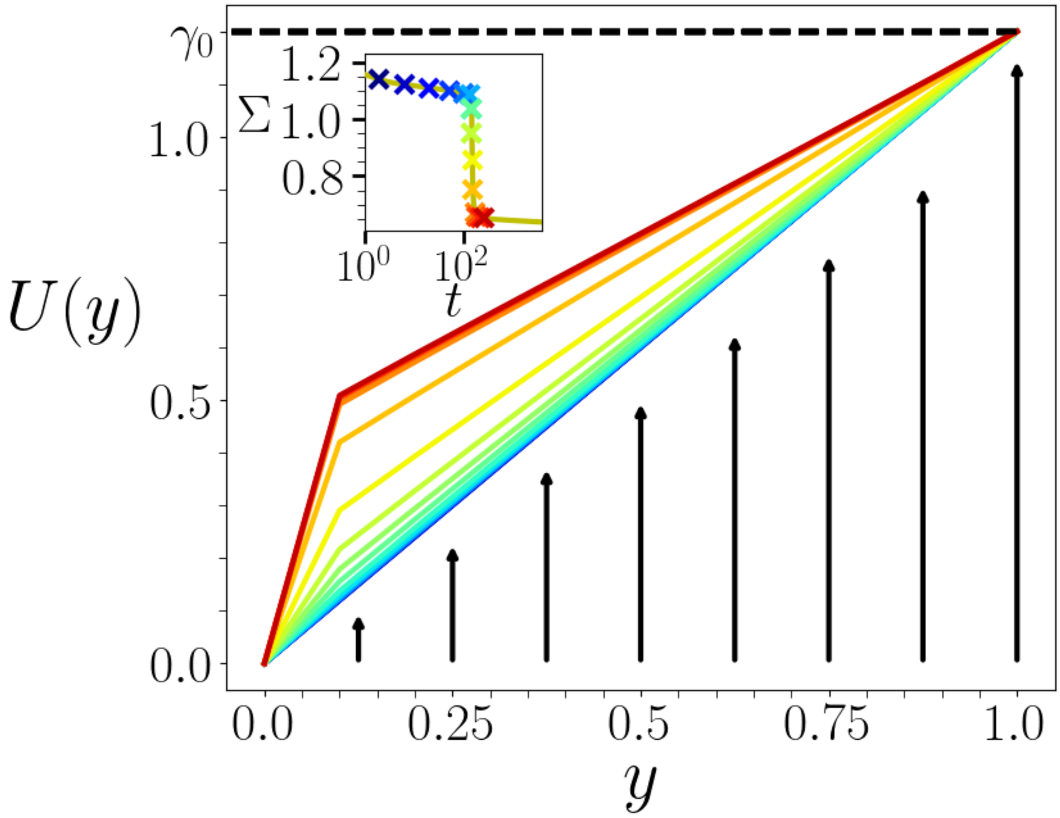

Figure 4.2: The displacement profile $U(y)$ as a function of the distance along the flow gradient y. The colour change of blue to red signifies increasing time, with the selected times indicated by crosses in the inset. The simulation corresponds to that in Fig. 4.1 with pre-shear equilibrium temperature $x_0 = 0.015$ and step strain amplitude $\gamma_0 = 1.2$. Highlighted by the black arrows is the flow direction x_{axis}.

Bottom panel: Stress decay Σ as a function of time t after the imposition of a step strain of amplitude $\gamma_0 = 1.2$, as simulated within the Thermal Elasto-Plastic model, for a single pre-shear equilibrium temperatures $x_0 = 0.015$ and with allowed shear heterogeneity ($S = 10$). Also highlighted are a selection of times with coloured crosses (from blue to red in increasing time) for a single simulation where $x_0 = 0.015$ and $\gamma_0 = 1.2$, for which the displacement profile $U(y)$ is plotted in the main figure.

Key result: Shape of $U(y)$ evidence of catastrophic banding.

take into account its effects. However, the shape of the banded profile just described does highlight the importance of sample preparation in experimental and theoretical studies, an issue that is gaining recognition in the literature [161, 201–203].

The behaviour of the strain distribution $P(l)$ during the stress relaxation can be seen in Fig. 4.3. The inset is a reminder of the influence of the input variables outlined in Section 2.3. This can be summarised as follows:

- The amplitude of the imposed step strain γ_0 determines the mean of the initial strain Gaussian $P_0(\gamma_0, x_0)$.
- The pre-shear equilibrium temperature x_0 determines the width of the initial strain Gaussian $P_0(\gamma_0, x_0)$.
- The working temperature of the system x determines the slope of the yielding rate $r(l)$.

The effect of these input variables will be crucial to understanding the complex behaviour exhibited by the TEP model systems in this work.

The main plot in Fig. 4.3 outlines the general behaviour of the strain distribution under the step strain protocol. The example simulation used in Fig. 4.3 is the same as that seen in Fig. 4.2, with the colours corresponding to times consistent across the plots. The dark blue line shows the initial strain Gaussian $P_0(\gamma_0, x_0)$, and the black line represents the yielding rate function $r(l)$. The overlap of these functions is highlighted in yellow. As discussed in Section 2.3.2, this overlap represents what fraction of the strain distribution will contribute to yielding.

As this part of the distribution on a particular streamline yields, its visco-elastic stress σ_s, equal to the integral of $lP_s(l)$ (see Section 2.3.2), will decrease. Considering the force balance outlined by Eqs. (2.2.7) and (2.2.8) and the imposition of a macroscopic strain rate of zero $\dot{\gamma} = 0$, this will cause an increase in the streamline strain rate $\dot{\gamma}_s$ so that the total shear stress remains uniform across streamlines. Hence, that streamline starts straining forward, seen in the forward movement of the strain

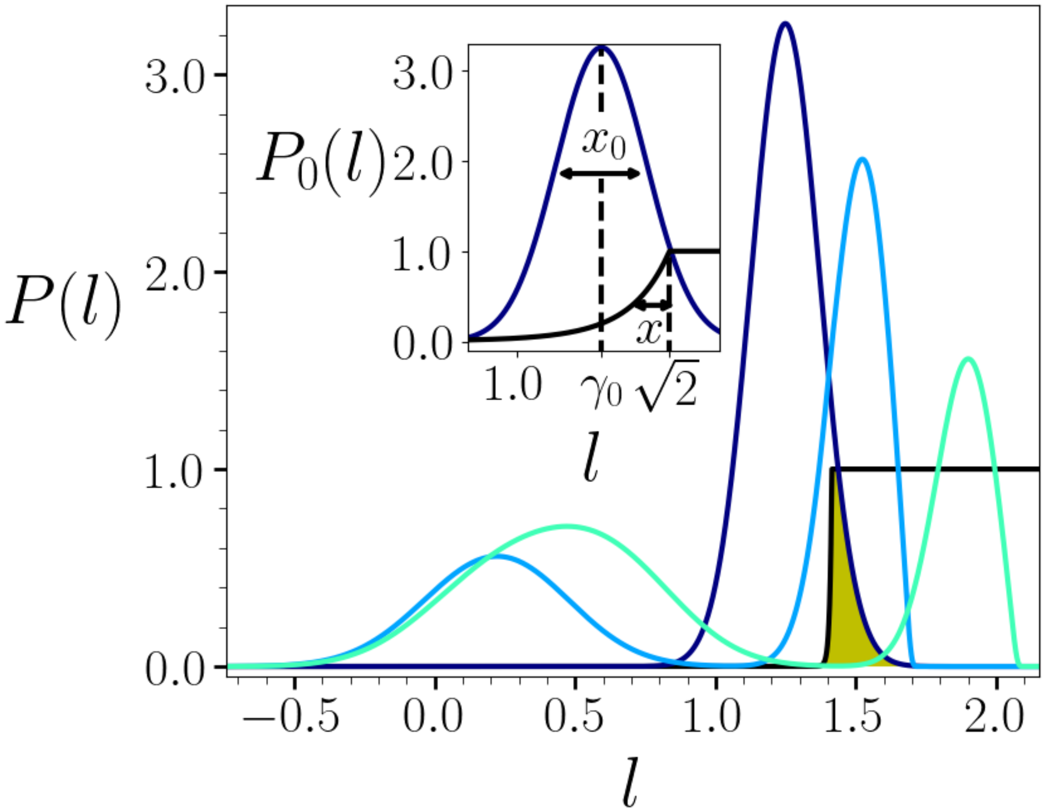

Figure 4.3: The response of the strain distribution $P(l)$ of a streamline to a step strain of amplitude $\gamma_0 = 1.2$ with pre-shear equilibrium temperature $x_0 = 0.015$ and working temperature $x = 0.01$, as simulated by the TEP model. The initial Gaussian distribution of strain $P_0(\gamma_0, x_0)$ at time $t = 0$ is plotted (dark blue, tallest peak), then $P(l)$ at $t = 148$ (light blue, second tallest peak) and at $t = 153$ (light green, right-most peak). The colours represent the times that correspond to the crosses in the same simulation in Fig. 4.2. Also plotted is the yielding rate function $r(l)$ (black line). Shaded in yellow is the area where the multiple $r(l)P_0(\gamma_0, x_0)$ will be non-zero, corresponding to the region of strain that contributes to the initial yielding integral $I(t = 0)$ in Eq. (4.2.4).
Inset: The initial strain distribution probability density Gaussian function $P_0(\gamma_0, x_0)$ as a function of strain l for the above simulation. Also plotted is the yielding rate function $r(l)$ for a larger working temperature $x = 0.15$ than in the above simulation to highlight its shape on a visible scale relative to the width of $P_0(\gamma_0, x_0)$. This inset is intended to highlight the effects of the imposed step strain amplitude γ_0 (the mean of the Gaussian), the pre-shear equilibrium temperature x_0 (the width of the Gaussian), and the working temperature x (the penetration of the yielding rate function).
Key result: Banding event after step strain dependent on initial parameters γ_0, x_0 and x.

distributions from the blue to the green line in Fig. 4.3. Note that the yielding of this part of the strain distribution causes an increase in the strain distribution around zero, as part of the 'rebirth' after yielding discussed in Section 2.3.2, which can be seen in Fig. 4.3.

Recall in Section 2.2.2, the macroscopic strain rate is equal to the average of the streamline strain rates $\overline{\dot{\gamma}} = \frac{1}{S}\sum_{s=0}^{S}\dot{\gamma}_s = 0$, therefore the other streamlines compensate for this forward straining streamline by straining backwards. In these backwards straining streamlines, the bulk of the distribution of local strains remains below the threshold for local yielding, leading to a predominantly elastic response. These streamlines do not contribute to yielding and so the discussion will henceforth only focus on the streamline that is straining forward, and it is this streamline strain distribution that is plotted in Fig. 4.3.

The forward strain rate on this key streamline just identified causes the region of the initial strain Gaussian $P_0(\gamma_0, x_0)$ that previously had a negligible yielding rate $r(l \ll \sqrt{2}) \approx 0$ to move into values of strain where the rate of yielding is significant $r(l \approx \sqrt{2}) > 0$ (the light blue line in Fig. 4.3), which then begins to yield. This consequent yielding accelerates the forward strain rate on this important streamline, pushing even more of the initial strain Gaussian into values of strain with a non-zero yielding rate (the green line in Fig. 4.3). This process then repeats, resulting in an accelerating avalanche of yielding, leading to shear banding. The final strain distribution (green line) in Fig. 4.3 highlights the moment where the entirety of the remaining original distribution is over the yielding threshold, and is therefore likely to yield on a small timescale. The time that this distribution is taken is at the point of banding, as can be seen by the corresponding coloured cross in Fig. 4.1.

The general process just described above is universal across all the simulations seen in this chapter. The differences in simulation results are therefore entirely a consequence of the input parameters.

Having demonstrated the formation of shear bands and explained its origin, it is logical to next analyse its extent and delay time. Previous work by the author on the SGR model [91] suggests that these instabilities occur on a catastrophic scale, and can happen after a long delay time. Corroboration of this with the TEP model results would lend this finding greater weight.

4.2.2 Degree of Shear Banding

One way to quantify the degree of shear banding is $\Delta\Sigma$, defined as the difference in the stress response between the simulation with enforced shear homogeneity ($S = 1$) and that with allowed heterogeneity ($S > 1$) [91]. Results for this quantity are plotted as a function of time in the bottom panel in Fig. 4.1. While results from the SGR model found no upper limit to the degree of banding [91], the results here for the TEP model show a convergence to a constant degree of banding. This effect can also be seen in the standard deviation in strain $\Delta\gamma$ in the middle panel of Fig. 4.1, which produces another measure of the degree of strain banding in the material.

It is surprising that the degree of shear banding that develops is roughly independent of the degree of sample annealing prior to shear. This contrasts with comparable simulations in previous work by the author [91] on the SGR model, which showed an increase in the magnitude of banding with increased age of the sample prior to shear. This implies that it is a consequence of the TEP model, but it is not exactly clear how the model settles on this consistent value.

Despite this, Fig. 4.1 shows that the scale of this banding is large relative to the imposed parameters. The stress drop in Σ and the rise in the standard deviation in the strain $\Delta\gamma$ are on the order of the size of the imposed step strain γ_0. This means that the instability is pronounced enough to be visible and cause material failure. A stress drop on a similar scale to that seen here in an experimental scenario caused complete material fracture [214]. Due to the consistency in degree of banding, the rest of this study will focus on the time at which shear banding takes place.

4.2.3 Banding Time t^* and the Imposed Step Strain γ_0

The banding time t^* at which these shear banding instabilities occur is defined as the time at which the standard deviation in the strain $\Delta\gamma$ reaches 0.1 (as highlighted in Fig. 4.1). This corresponds to the degree of strain banding across the sample reaching roughly 10% of the overall imposed step strain (as the imposed step strain values range between $1-1.3$). As seen in Fig. 4.1, this definition captures the time at which the standard deviation in strain increases rapidly. Previous studies have used different definitions for the banding time, such as the time of the peak in the strain rate standard deviation $\Delta\dot{\gamma}$ [91]. The definition used in this study captures a similar time to these definitions, but due to the small amount of noise present in $\Delta\dot{\gamma}$, defining the banding time relative to its integral $\Delta\gamma$ is more consistent.

The banding time t^* is plotted as a function of the amplitude of the imposed step strain γ_0 in Fig. 4.4 for a range of pre-shear equilibrium temperatures x_0. These curves show a clear trend: the banding time increases dramatically as the size of the step strain decreases for all values of x_0 explored. This general behaviour corresponds with step strain experiments on a polymer melt which found the induction time for a shear banding event increases with decreasing step strain amplitude [66]. Within the scope of the TEP model: for smaller γ_0, the distribution of local strains $P(l)$ will initially be located at strains where the yielding rate $r(l)$ is smaller. This means less initial yielding, and so the avalanche effect of shear banding described above will take longer to occur. With values of t^* up to 10^4 in Fig. 4.4, the TEP model has found highly delayed shear banding under the step strain protocol, in addition to that found previously in the SGR model [91].

The behaviour in Fig. 4.4 is particularly interesting because the banding time t^* appears to be diverging at a non-zero step strain amplitude γ_0. The shape is reminiscent of the divergence in relaxation time τ at the glass transition temperature T_0 as modelled by the Vogel-Fulcher-Tamman (VFT) law [72, 215–218], which has

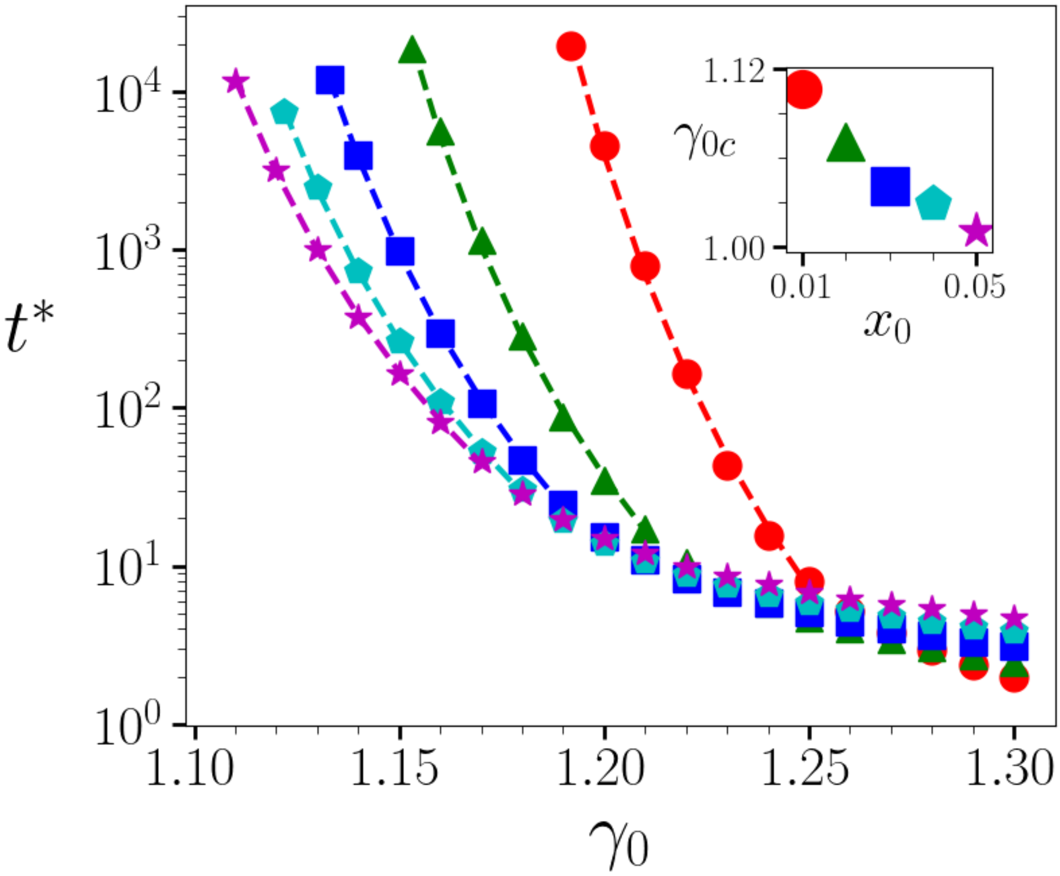

Figure 4.4: The banding time t^* as a function of the imposed step strain γ_0 for a range of pre-shear equilibrium temperatures x_0=[0.05, 0.04, ..., 0.01] (in order from purple to red or stars to circles). The dashed lines correspond to fitting to an exponential function of the form given in Eq. (4.2.2). The inset shows how the value of the critical strain γ_{0c} in the fitting varies with x_0.
Key result: t^* increases exponentially with decreasing γ_0.

the following form

$$\tau = Ae^{\frac{B}{T_0 - T}} , \tag{4.2.1}$$

where the relaxation time diverges as temperature T approaches T_0. Although the VFT law was originally designed to describe divergence with temperature, it has been adapted by other studies. Some studies have replaced the temperature with other variables, such as the packing fraction [218], and others have used the VFT relaxation time τ to model the stress and strain responses to shear protocols [217].

This work takes inspiration from VFT, and fits the banding time to a similar exponential function, now as a function of imposed strain

$$t^* = Ae^{\frac{B}{\gamma_0 - \gamma_{0c}}} , \tag{4.2.2}$$

where γ_{0c} is the critical step strain below which no banding occurs, and A and B are fitting parameters. This is an extrapolation of the original VFT law, but it can be argued that the banding time t^* diverging is comparable to the VFT law's relaxation time τ in the system diverging. In both scenarios, the material is unable to relax stress following the application of strain.

The dependence of the critical step strain amplitude γ_{0c} on the pre-shear equilibrium temperature x_0 can be seen in the inset of Fig. 4.4. As x_0 decreases, γ_{0c} increases. Recall that x_0 defines the width of the initial strain Gaussian $P_0(\gamma_0, x_0)$, and γ_0 defines its mean location. For banding to occur, the initial overlap of the strain Gaussian $P_0(\gamma_0, x_0)$ with the yielding rate function $r(l)$ must be large enough such that some yielding is probable within the computational limits of the simulation. In the instance that the width of the Gaussian, x_0, is chosen to be small, the location of that Gaussian, γ_0, must be large to maintain that initial overlap and vice versa. Hence the dependence of the critical step strain amplitude γ_{0c} on x_0.

The fitting in Eq. (4.2.2) implies that the banding time diverges at a non-zero step strain γ_{0c}. This can be understood within the model as follows: the yielding rate function $r(l) \propto \exp(-\frac{1-l^2}{x})$ at small values of l is very close to zero for small x. If the centre of the initial Gaussian strain distribution $P_0(\gamma_0, x_0)$, given by the mean of the distribution γ_0, is small enough, the overlap of the distribution $P_0(\gamma_0, x_0)$ with the yielding rate function $r(l)$ is equal to zero within computational accuracy. Therefore, there is zero probability of yielding for all elements and consequently, there is no banding. A similar non-zero divergence for the banding time at a critical amplitude was found under the Large Amplitude Oscillatory Strain protocol for a similar TEP model [70, 212], with a fitting directly comparable to the results found here.

With increasing computational accuracy, the overlap of $P_0(\gamma_0, x_0)$ and $r(l)$ would actually be non-zero; the banding time may therefore only strictly diverge at a step strain of zero. Indeed, it is impossible to fully establish if the banding time is curving up to reach a constant gradient (and therefore divergent at zero), because simulation times exceeding $t^* = 10^4$ cannot be accessed computationally. It would also be difficult to test whether this non-zero divergence is a physical effect, because these exponentially increasing banding times would quickly fall outside sensible experimental timescales. As such it is concluded that, within measurable timescales, the banding time increases exponentially with decreasing step strain.

4.2.4 Banding Time t^* and the Pre-shear Equilibrium Temperature x_0

A similar divergence to that found in Section 4.2.3 is encountered when studying the variation of the banding time t^* with the pre-shear equilibrium temperature x_0. This is plotted in Fig. 4.5 for a range of step strain amplitudes γ_0. Recall that an increase in $1/x_0$ is comparable to increasing the degree of annealing of the material [9, 171], and this can be seen to result in an exponential increase in the banding time for small x_0 in Fig. 4.5. This correlates with results found in previous work by the author in the SGR model, where increasing the age of the material increased the banding time without limit [91]. The degree of annealing can be tuned for some amorphous materials, such as metallic glasses [48, 169–171], but is more difficult to vary for others, such as emulsions [48]. An experimental study on a polymer melt found that the induction time for shear banding under a step strain increased with increasing number of connected polymer chains, which is comparable as a consequence of an increased age or annealing [66].

Recalling the divergence in the banding time t^* at non-zero step strain γ_0 in Section 4.2.3, where γ_0 sets the mean location of the initial Gaussian distribution of local strains $P_0(\gamma_0, x_0)$, a divergence in t^* at non-zero x_0, which defines the width of $P_0(\gamma_0, x_0)$, might also be expected. Indeed, a similar exponential function to Eq. (4.2.2) is found to fit the behaviour in Fig. 4.5. This again takes inspiration from Vogel-Fulcher-Tamman (VFT) law [72, 215–218], by fitting to the form

$$t^* = Ae^{\frac{B}{x_0^{-1} - x_{0c}^{-1}}}, \tag{4.2.3}$$

where x_{0c} is the critical pre-shear equilibrium temperature at which the banding time diverges, and A and B are fitting parameters. This use of a VFT-like fitting more closely resembles the original VFT law, because x_0 represents a temperature. Indeed, x_0 has been used in this context for metallic glasses [170]. The main comparison is the same as in Eq. (4.2.2), the relaxation time τ diverging in the original VFT law is comparable to the banding time t^* diverging here. In both scenarios, the material is unable to relax stress following the application of strain.

The dependence of the critical pre-shear equilibrium temperature x_{0c} on the step strain amplitude γ_0 can be seen in the inset of Fig. 4.5. These results correlate with the dependence of the critical step strain amplitude γ_{0c} with x_0 in Fig. 4.4, discussed in Section 4.2.3. As γ_0 decreases, x_{0c} increases, and vice versa.

The divergence in t^* at a non-zero value of x_0 contrasts with the earlier work done by the author on the SGR model, which found a divergence in t^* with the waiting time t_w at $t_\mathrm{w} \to \infty$ [91]. Although the preshear-equilibrium temperature x_0 in the TEP model is not directly comparable to the waiting time t_w in the SGR model, the difference in divergence is interesting, and will be discussed further when analysing the SGR model results in Section 4.3.

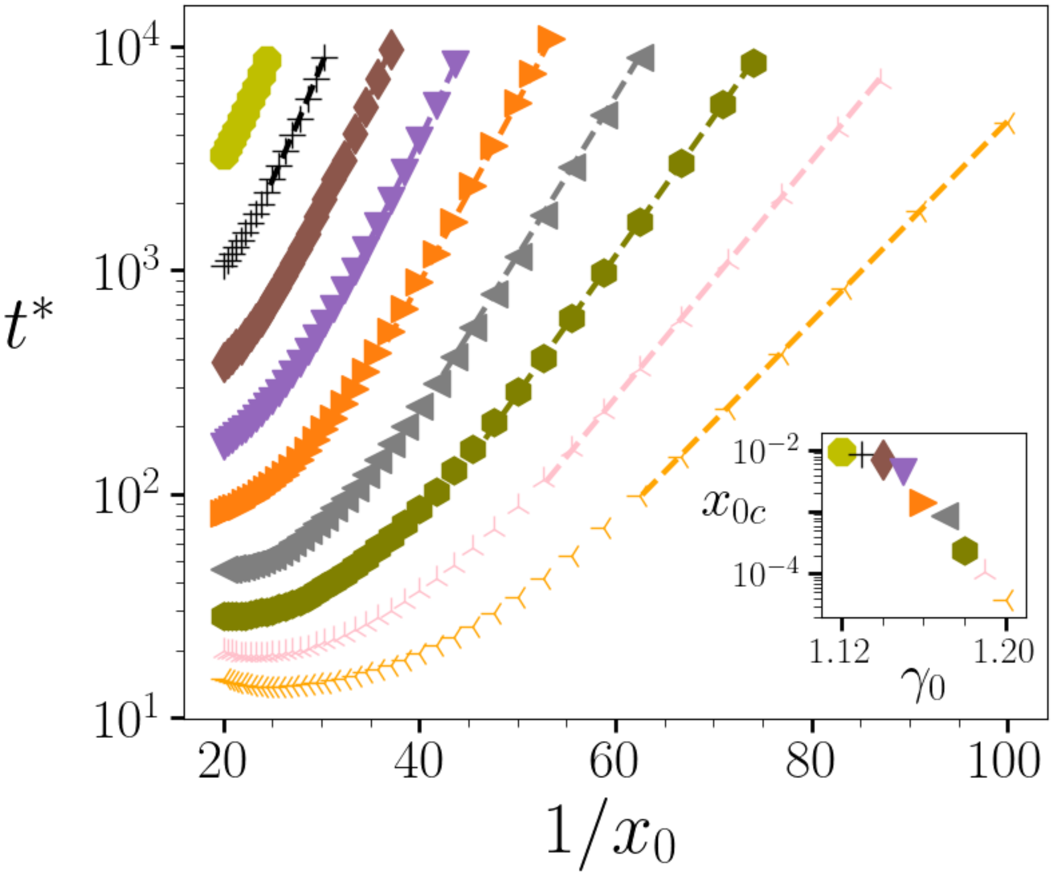

Figure 4.5: The banding time t^* as a function of the inverse of the preshear equilibrium temperature x_0 for a range of imposed strain amplitudes γ_0=[1.12,1.13,...,1.2] (in order from mustard to orange or hexagons to left-facing tri-lines). The dashed line corresponds to fitting to an exponential function as in Eq. (4.2.3). The inset shows how the value of the critical preshear equilibrium temperature x_{0c} in the fitting varies with γ_0. Note that the plotting against the inverse of x_0 is used to show the increase in banding time t^* with increasing degree of sample annealing prior to shear, as characterised by $1/x_0$.
Key result: t^* increases exponentially with $1/x_0$.

It can be argued that the curves in Fig. 4.5 appear to be linear, where a constant gradient would suggest a divergence at $x_0 \to 0$. Certainly, as γ_0 increases, the critical x_{0c} drops logarithmically towards zero. However, the VFT-like fitting in Eq. (4.2.3) produces a more accurate fit than a simple exponential (where $t^* \propto e^{1/x_0}$) for the values found in Fig. 4.5. In addition, the divergence in Eq. (4.2.3) is similar to the disappearance of banding found in a similar TEP model under shear startup at a critical level of annealing, represented by x_0 in this model [171].

As noted above, it is not feasible computationally to access times above $t^* \approx 10^4$. Therefore, any true divergence is difficult to establish. Regardless, the divergence is an interesting feature of the TEP model and must be considered when using this model for any extreme timescale studies.

4.2.5 Banding Time t^* and Temperature x

The dependence of the banding time t^* on the working temperature x is plotted in Fig. 4.6. An exponential increase in t^* with $1/x$, as seen in the variation with pre-shear equilibrium temperature x_0, may be expected because both x and x_0 are forms of temperature. This is present in the small values of $1/x$, where the banding time t^* increases exponentially with $1/x$. However, for values of the step strain amplitude $\gamma_0 > 1.225$, the increase in t^* with increasing $1/x$ is seen to taper off, before decreasing, eventually resolving to a consistent value at large $1/x$.

For large values of $1/x$, the banding time t^* is constant for simulations with $\gamma_0 > 1.225$, despite changes in x. The cause of this effect is that x is so small ($x \approx 10^{-5}$), that it is effectively zero under computational accuracy. Recall from Eq. (2.2.3) that the yielding rate $r(l)$ is dependent on $\exp(-(1 - l^2/2)/x)$. Therefore, changing the working temperature x at these small values has no impact on the banding time. The behaviour of individual simulations must be examined to understand how the banding time t^* is affected by the change from finite x to zero within computational accuracy.

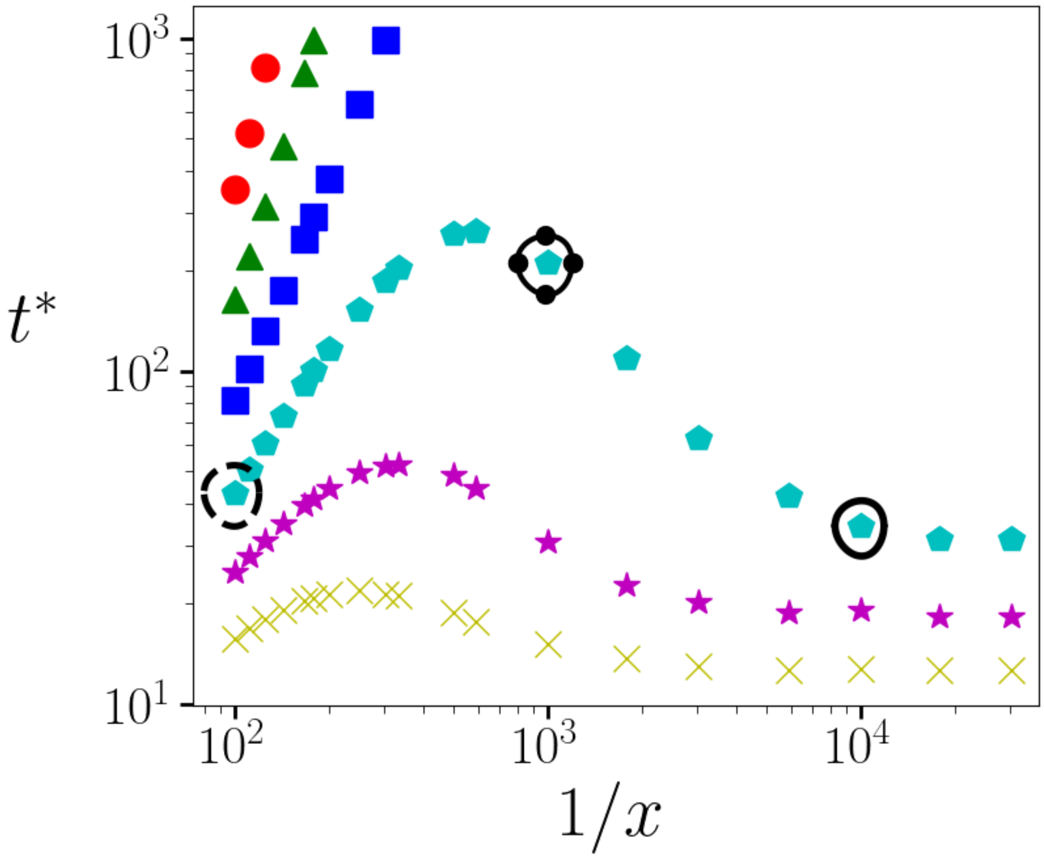

Figure 4.6: The banding time t^* as a function of the inverse of the temperature x for a single pre-shear equilibrium temperature $x_0 = 0.01$ and a range of step strain amplitudes γ_0=[1.215,1.22,...,1.24] (in order from red to yellow or circles to crosses). Highlighted by circling the relevant t^* value are three simulations studied further in Fig. 4.7 and Fig. 4.9, where $x = 10^{-2}$ (black dashed line), $x = 10^{-3}$ (black line with circles) and $x = 10^{-4}$ (black solid line).
Key result: t^* displays an unexpected non-monotonic relationship with x.

To explore this in more detail, simulations for three different values of the working temperature x have been selected to focus on. These are highlighted by circling the relevant value of t^* in Fig. 4.6 at a step strain amplitude of $\gamma_0 = 1.23$ and pre-shear equilibrium temperature $x_0 = 0.01$. These summarise the behaviour in the three regimes of x:

- Large x ($x = 10^{-2}$ – Dashed line in Fig. 4.6) where the banding time is small due to x being large.
- Medium x ($x = 10^{-3}$ – Line with circles in Fig. 4.6) where the decrease in x has caused an increase in the banding time.
- Small x ($x = 10^{-4}$ – Solid line in Fig. 4.6) where the decrease in x has caused a decrease in the banding time.

The top panel of Fig. 4.7 shows the scale of strain banding across the material (the standard deviation in strain $\Delta\gamma$) as a function of time t for each of these three values of x. The overall behaviour appears to be very similar for the three values of x that are explored. Initially, the scale of strain banding $\Delta\gamma$ is small, it then slowly increases as the system yields and the strain field becomes more heterogeneous. The slow increase in $\Delta\gamma$ concludes in a sudden avalanche of yielding causing a dramatic increase in $\Delta\gamma$, which corresponds to a catastrophic shear banding instability. The similar behaviour in the three simulations in Fig. 4.7 indicates that there is no difference in the overarching behaviour leading up to banding. Instead, the variation in x changes the rate at which this behaviour occurs.

As discussed previously, the banding time t^* is strongly connected to the overlap of the strain distribution $P(l)$ and the yielding rate function $r(l)$. For this reason, the yielding integral can be used to gain further insight. Recall that

$$I = \int r(l)P(l)l\,dl\,, \tag{4.2.4}$$

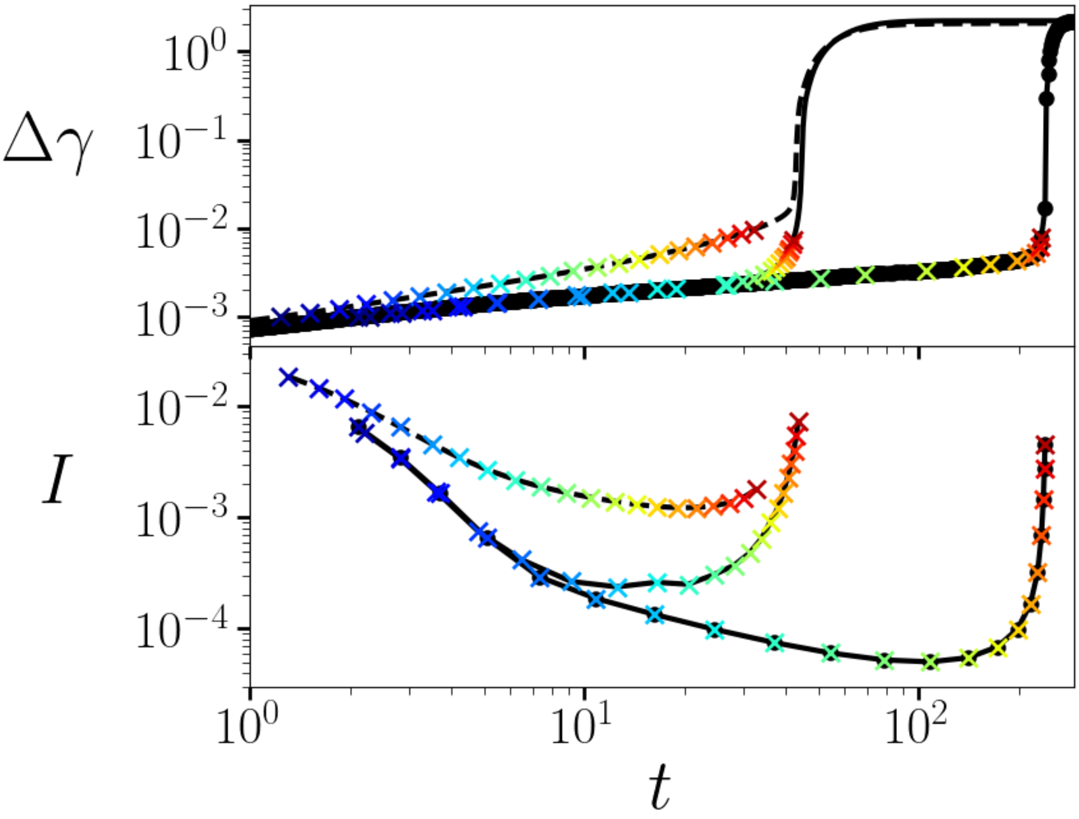

Figure 4.7: **Top panel**: The standard deviation in strain across the sample $\Delta\gamma$ as a function of time t for three simulations highlighted in Fig. 4.6, where $x = 10^{-2}$ (dashed), $x = 10^{-3}$ (circles) and $x = 10^{-4}$ (solid) ($\gamma_0 = 1.23$ and $x_0 = 0.01$).
Bottom panel: The corresponding yielding integral I (Eq. (4.2.4)) over time. The coloured crosses are taken at logarithmically equal spaces in $\Delta\gamma$ between 10^{-3} and 10^{-2} for each simulation, corresponding to the lines in Fig. 4.9.
Key result: The behaviour of $\Delta\gamma$ is intrinsically connected to the behaviour of I.

where the integral is taken over the strain space l, as described in Section 3.3.4. This integral measures the average rate of stress relaxation across the system by computing the average of $lr(l)$ across the distribution $P(l)$.

The behaviour of this yielding integral I as a function of time is plotted in the bottom panel of Fig. 4.7. Again, the overall behaviour is the same for the three simulations considered: initially, I is large, followed by a decrease as the material begins to yield, before finally rising as shear banding occurs. This can be understood in more detail by returning to Fig. 4.3 and studying the behaviour of the strain distribution over time.

Initially there is some fraction of the Gaussian of strain values $P_0(\gamma_0, x_0)$ overlapping the region of non-zero yielding rate $r(l)$ (shaded in yellow), giving a non-zero yielding integral $I > 0$. As this fraction progressively yields and resets to $l = 0$, this overlap decreases and therefore so does the yielding integral I. However, because the average strain across streamlines is held constant in a step strain simulation, this yielding causes a forward strain rate on the streamline which is perturbed forward the most. This combined effect is shown in the decreased height and positive strain of distributions at later times (light blue and green lines). As discussed previously, this analysis will only focus on the forward straining streamline relevant to banding.

The forward strain rate on this key streamline causes the overlap between the strain distribution $P(l)$ and the yielding rate function $r(l)$ to increase, leading to a larger value for the yielding integral. Therefore, the behaviour of the yielding integral can be summarised by the competition between two effects:

(i) The yielding of the strain distribution $P(l)$ that overlaps with the yielding rate function $r(l)$ will cause I to decrease.

(ii) The forward strain rate caused by the yielding in (i) will result in more of the strain distribution $P(l)$ being pushed into regions where the yielding rate function $r(l)$ is significant, causing I to increase.

While the overall process leading to shear banding is universal across the simulations, Fig. 4.7 highlights the differences between the three simulations.

The first indication of differences between these three simulations appears in the top panel of Fig. 4.7, where the gradient of the aforementioned slow increase is clearly larger for the large value of $x = 10^{-2}$ (dashed line). This can be understood physically, by recognising that the larger available thermal energy allows more yielding leading to an earlier banding event.

This behaviour is also clear in the bottom panel of Fig. 4.7. The $x = 10^{-2}$ (dashed line) simulation starts with a large yielding integral I which, despite following the overall behaviour described above, does not decrease to a significant minimum. This implies that there is a large initial rate of yielding which causes a large forward strain rate. Then, over the time building up to banding, this strain rate provides a regular supply to the system of yielding, leading to a large acceleration, and consequently a short time before banding. This can be seen in Fig. 4.3, where the initial overlap between the strain distribution $P(l)$ and the yielding function $r(l)$ (the yellow shading), and consequently the yielding integral I, is large. The strain distribution at a later time (the green line) has dropped in height due to the large amount of yielding and has also consequently strained forward significantly. In the aforementioned competition between the two effects, the forward strain rate in (ii) dominates over the yielding in (i) for the $x = 10^{-2}$ (dashed line) simulation.

Note that the initial strain distribution $P_0(\gamma_0, x_0)$ is the same for all three values of x, because the step strain amplitude γ_0 and pre-shear equilibrium temperature x_0 are the same. However, the yielding function $r(l)$ is different, with a broader distribution for large x. As x decreases, there is less overlap between the initial strain Gaussian $P_0(\gamma_0, x_0)$ and the yielding function $r(l)$, and therefore less initial yielding. This leads to a smaller forward strain rate, and should consequently cause the avalanche effect to be delayed. However, in the bottom panel of Fig. 4.7, when $x = 10^{-4}$ (black solid line), the value of the yielding integral I increases to the banding event at an earlier time than when $x = 10^{-3}$ (black line with circles), despite having a smaller initial forward strain rate. This implies there is another effect dominating when x is small.

This is further explored in Fig. 4.8, whose top panel replots the data in the bottom panel of Fig. 4.7 relative to steps in the strain standard deviation $\Delta\gamma$ instead of time. The $x = 10^{-4}$ (black solid line) simulation is unable to attain as small a value of I as the $x = 10^{-3}$ (black line with circles) simulation. Therefore, despite the slower initial forward strain rate, at the turning point where the yielding integral reaches its minimum I_{min}, there is a larger amount of yielding occurring for the small x.

The reason for this is plotted in Fig. 4.9. These show the strain distribution $P(l)$ on the forward straining streamline at different times in the simulation. For the $x = 10^{-3}$ simulation in the bottom panel of Fig. 4.9, the two effects discussed previously occur simultaneously:

(i) A fraction of the strain distribution $P(l)$ with a non-zero yielding rate $r(l) > 0$ yields, decreasing in size.

(ii) The yielding in part (i) causes the streamline to strain forward with an accelerating strain rate.

Initially (the blue to the green lines in the bottom panel of Fig. 4.9), the effect described in (i) dominates, which makes the distribution look as if it is receding. This is because the initial forward strain rate is small relative to the rate of yielding. The effect described in (ii) only becomes clear in the later times (the yellow to the red lines in Fig. 4.9) where the strain distribution $P(l)$ has an accelerating strain rate which then dominates over the rate of yielding causing the distribution to strain forward. This acceleration leads to an avalanche of yielding which corresponds to the catastrophic banding event.

There is a very different picture when observing the $x = 10^{-4}$ distributions in the top panel of Fig. 4.9. The critical difference is the effect described in (i). In the $x = 10^{-3}$ simulation in the bottom panel of Fig. 4.9, the yielding of the effect described in

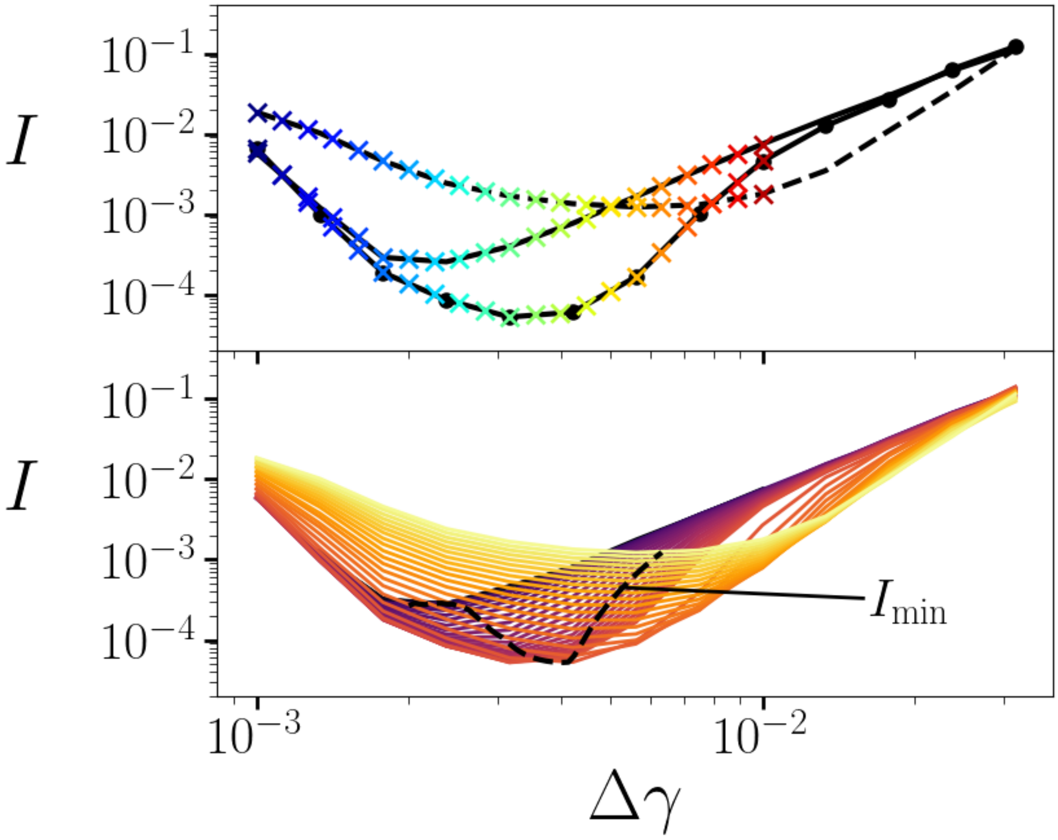

Figure 4.8: The yielding integral I (Eq. (4.2.4)) as a function of the standard deviation in strain across the sample $\Delta\gamma$ for the simulation where $\gamma_0 = 1.23$ and $x_0 = 0.01$.
Top panel: The three simulations that are highlighted in Fig. 4.6, where $x = 10^{-2}$ (dashed), $x = 10^{-3}$ (circles) and $x = 10^{-4}$ (solid). The coloured crosses are taken at logarithmically equal spaces in $\Delta\gamma$ between 10^{-3} and 10^{-2} for each simulation, corresponding to the lines in Fig. 4.9.
Bottom panel: A range of working temperatures $x = [10^{-5}, 10^{-4.9}, ..., 10^{-2}]$ (in order from dark blue to yellow). Highlighted by the dashed line is the minimum value of the yielding integral I_{min} for each value of x.
Key result: The behaviour of I is dramatically changed by the variation in x.

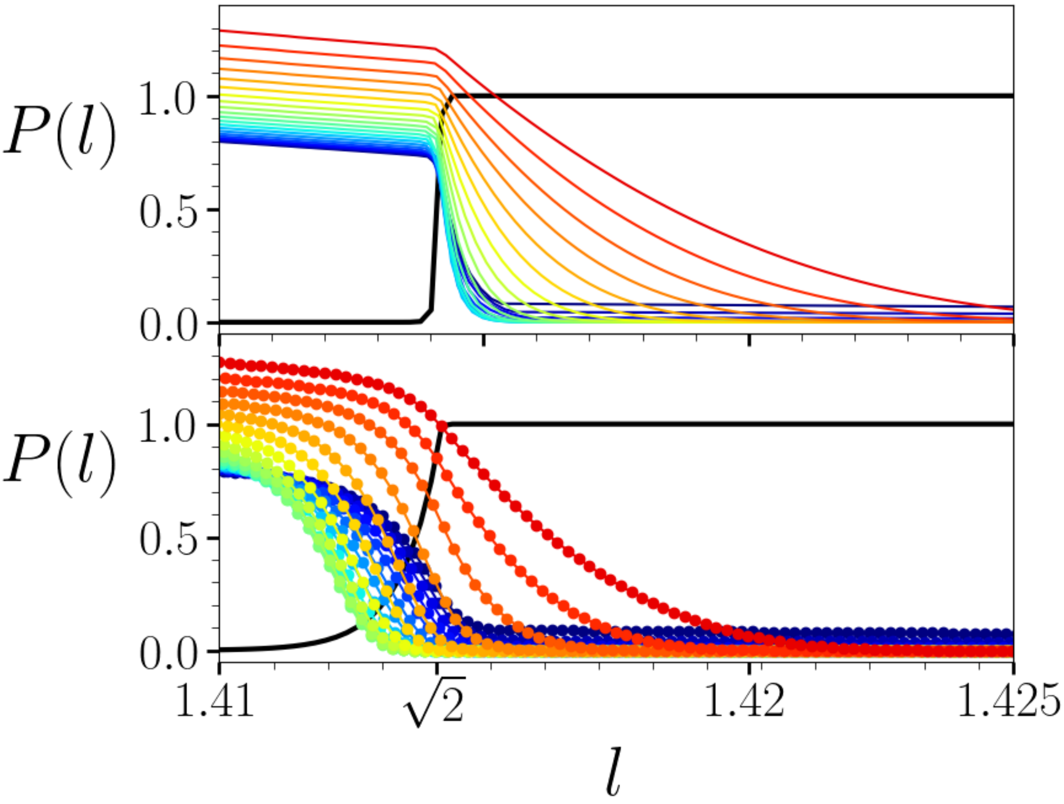

Figure 4.9: The probability density function $P(l)$ of local strain l for several values of time for a small $x = 10^{-4}$ (top panel) and medium $x = 10^{-3}$ (bottom panel). Time increases from blue to red (from the sharp drop-off to the broader distribution in the top panel), with the colours corresponding to the crosses in Fig. 4.7 and Fig. 4.8. Plotted in the black line is the yielding rate function r. The horizontal axis has been focussed as to highlight the behaviour around the threshold for yielding ($l = \sqrt{2}$). **Key result**: The behaviour of $P(l)$ close to the threshold $l = \sqrt{2}$ is key to understanding the variation of t^* with x.

(i) caused a smooth distribution to appear to recede. In the $x = 10^{-4}$ simulation in the top panel of Fig. 4.9, the yielding of the strain distribution in effect (i) instead causes the strain distribution to form a steep drop off at the yielding rate threshold of $l = \sqrt{2}$ (the blue to green lines). Consequently, as the distribution strains forward, the fraction of the distribution being pushed into a non-negligible yielding rate is large. This large amount of yielding accelerates the effect described in (ii), and therefore the banding happens earlier.

This means that, despite the small initial strain rate at such a small x, the shape of the forward straining distribution is such that the amount of yielding is relatively high. This yielding causes an acceleration in the forward strain rate which causes the time before banding to decrease.

This effect can be summarised by the two competing factors that govern the behaviour of the banding time t^* with x:

- A smaller x results in a smaller initial yielding integral $I(t = 0)$, meaning a smaller initial forward strain rate which increases the time for the eventual banding avalanche t^*.
- A smaller x causes the shape of the yielding strain distribution to be steeper. This means, despite the small initial forward strain rate at small x in the point above, there is a larger yielding integral I over time as the distribution strains forward. This results in an increased acceleration which decreases the time for the eventual banding avalanche t^*.

These competing factors effectively control what fraction of the strain distribution is yielding and therefore accelerating the forward strain rate. This fraction is equal to the overlap of the strain distribution $P(l)$ and the yielding rate function $r(l)$, and therefore the average strain relaxation given by the yielding integral I provides a measure for this as well as an important statement: **The smaller the value of I, the less yielding is occurring, and therefore the longer that the eventual banding is delayed**.

This conclusion is clear from the top panel of Fig. 4.7, where the most delayed banding simulation ($x = 10^{-3}$ - line with circles) is also the one that achieves the lowest value of I. The cause of the small minimum value of I in this simulation can be seen in the green lines of the bottom panel of Fig. 4.9, where the overlap between the strain distribution $P(l)$ and the yielding rate $r(l)$ is small.

This argument can be expanded to look at how the variation of I as a function of $\Delta\gamma$ changes with more gradual x variation, as plotted with the dashed line in the bottom panel of Fig. 4.8. Here, the overall shape changes continuously in x, the minimum of the yielding integral I_{min} is initially large with large x, decreases with decreasing x, and then begins to increase again.

The variation of this minimum I_{min} with x can be compared to the variation in t^*, as plotted in Fig. 4.10. This provides the clearest connection between the mesoscopic behaviour intrinsic to the system (I) and the macroscopic effect (t^*). It is clear that the banding time is a direct consequence of the size of the minimum yielding integral I_{min} that the simulation can achieve.

The analysis above has outlined the origins of the unexpected variation of the banding time t^* with the working temperature x. In addition, the exploration of the yielding integral I has made it possible to quantify an earlier statement on the non-zero divergence in the banding time t^* with the step strain amplitude γ_0 and pre-shear equilibrium temperature x_0. Previously, this was explained as the overlap between the strain distribution $P(l)$ and the yielding rate function $r(l)$ going to zero within computational accuracy. This divergence can be equivalently described as where the yielding integral I reaches zero.

The work in this section has also highlighted wider issues on the effective range of TEP models more generally. When exploring extreme timescales and temperatures, TEP model systems become extremely sensitive to small value calculations. This can result in surprising behaviours, such as the non-zero divergences in t^* with γ_0 and x_0, or the non-monotonic dependence of t^* on x. They can also be limited by computational capacity, as in the case of x being so small ($x \approx 10^{-5}$), that

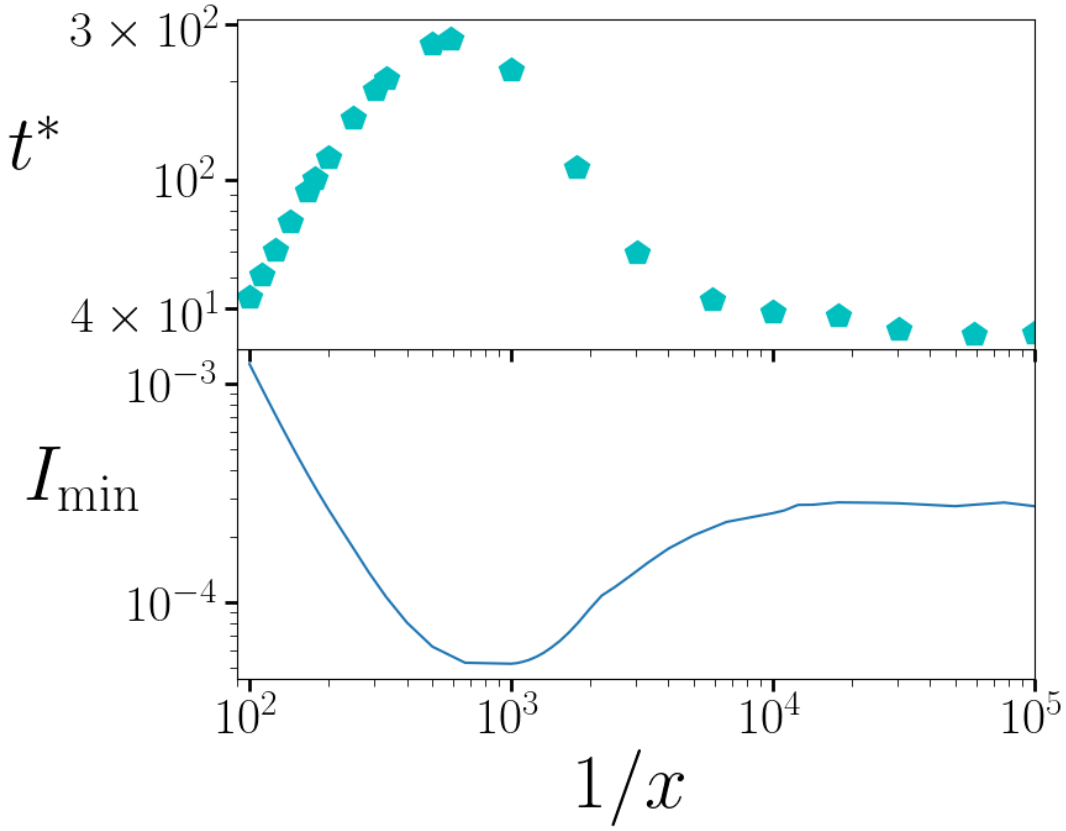

Figure 4.10: **Top panel**: The banding time t^* as a function of the inverse of temperature x for a pre-shear equilibrium temperature $x_0 = 0.01$ and step strain amplitude $\gamma_0 = 1.23$ (the colour and marker correspond to the same data plotted in Fig. 4.6).
Bottom panel: The minimum value of the yielding integral $I_{\rm min}$ for each of the above simulations.
Key result: The behaviour of t^* directly correllates with that of $I_{\rm min}$.

it is effectively zero. These factors must be taken into account when simulating amorphous material behaviour using TEP models.

4.2.6 The Athermal Limit

The results in the TEP model for the variation of temperature x presented in Fig. 4.6 indicate that, in the athermal limit $x = 0$, the highly delayed banding after imposition of a step strain seen when $x > 0$, is not possible. There are two behaviours present in Fig. 4.6. For the smaller values of γ_0 explored, t^* increases exponentially with increasing $1/x$, before becoming larger than can be explored numerically. For the larger values of γ_0, the dependence of t^* on $1/x$ is non-monotonic, resolving to a small banding time $t^* < 10^2$ as x becomes small. These results imply that in the athermal limit $x = 0$, the banding time will either be infinite, or small and finite.

Outside the athermal limit (for any finite but small x), highly delayed banding is dependent on a small but non-zero overlap between the strain distribution $P(l)$ and the yielding rate function $r(l)$, both of which are sloping functions. In the athermal limit, the yielding rate becomes a step function, as in Eq. (3.1.5) [9], so a long lasting small but non-zero overlap between these functions becomes impossible. In this scenario, the banding either occurs early, or not at all. This effect can be seen in the top panel of Fig. 4.11, where no banding times t^* beyond 10^2 are found, despite the exploration of a range of imposed step strains γ_0. Note that this is not an upper limit based on computation time, below a certain value of γ_0 for a given x_0, the system does not show any stress relaxation at all because the entire simulated strain distribution $P(l)$ is below the yielding rate function threshold and therefore where $r(l) = 0$.

Consequently, similar to the divergences of the banding time t^* outside the athermal limit with γ_0 (Fig. 4.4) and x_0 (Fig. 4.5), the divergence in t^* in the athermal limit can be seen as where the value of the yielding integral I reaches zero within computational accuracy. This corresponds to the overlap of the strain distribution

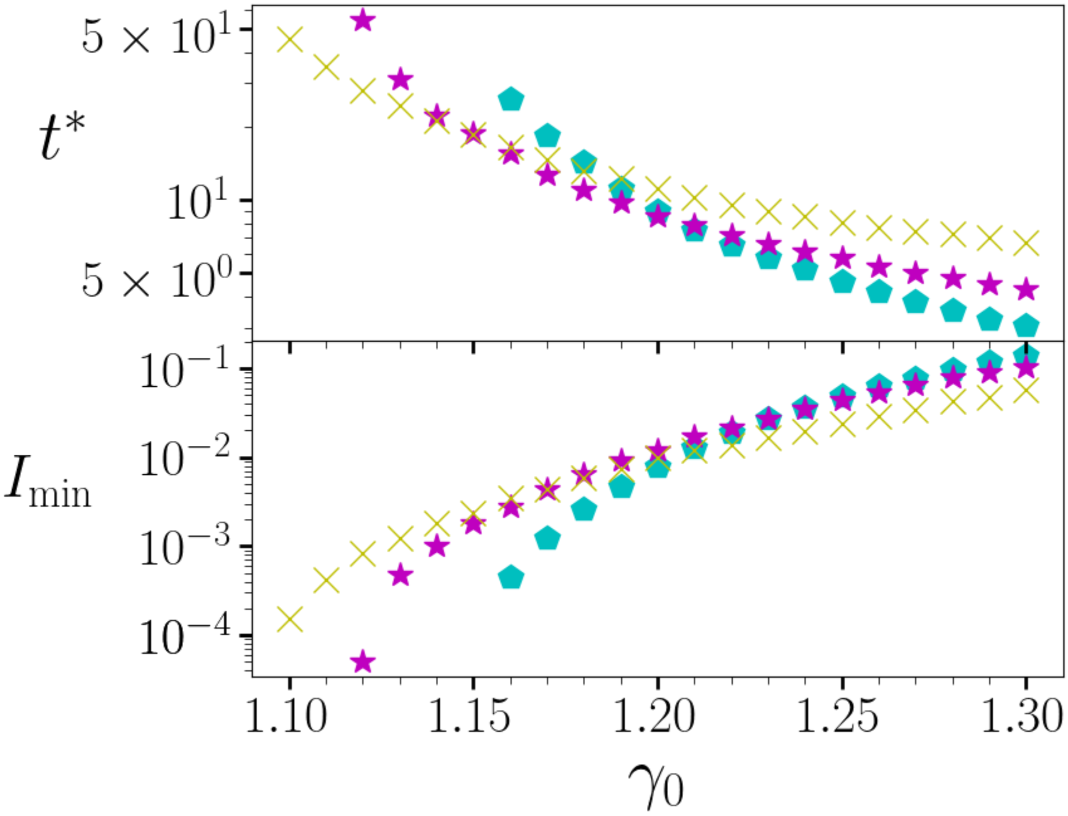

Figure 4.11: **Top panel**: The banding time t^* as a function of the imposed step strain γ_0 for the TEP model in the athermal $x = 0$ limit for a range of preshear equilibrium temperatures x_0=[0.03 (blue hexagons), 0.05 (purple stars), 0.08 (yellow crosses)].
Bottom panel: The minimum value of the yielding function I_{min} for each of the above simulations.
Key result: A significantly delayed t^* is not possible in the athermal $x = 0$ limit and the divergence in t^* correllates with I_{min} reaching zero.

$P(l)$ and the yielding rate function $r(l)$ reaching zero. This is confirmed by the bottom panel of Fig. 4.11, where the minimum value of the yielding integral I_{min} drops exponentially towards zero as the corresponding banding time t^* reaches its upper limit.

A critical strain under which no banding is seen is not surprising, as multiple studies into athermal systems under an oscillatory shear protocol find shear banding only above a certain critical strain amplitude [46,212,219]. In addition, other studies have also shown critical points for shear banding in the athermal limit above finite shear strengths [47,104,220]. Despite this, with greater computational accuracy, even for very small x_0 and γ_0 there will be a non-zero overlap causing a non-zero yielding integral I. However, the timescales associated with these scenarios fall way outside the scale of any real systems, so this becomes a philosophical question as opposed to a physical one.

Regardless, real athermal systems are often comprised of macroscopic granular particles that tend to be dominated by frictional forces [9,80,199,219,221]. When a mesoscopic cluster of molecules or particles (represented in models by an element) yields, the system isn't able to redistribute the strain change caused by the rearrangement without creating a huge avalanche of yield events which is more reminiscent of brittle fracture rather than fluidisation [161].

This can be considered within the framework of the TEP model, where all the energy depths of the elements are equal and shallow ($E = 1$). Therefore, when one element yields, it causes a dissipation throughout the material which causes other elements to yield that might not have done so if they had a larger energy depth $E \gg 1$.

In the athermal limit, the banding event is followed by no subsequent stress relaxation (unlike that found outside the athermal limit). This reflects a fractured material, unable to relax any further, as opposed to a thermal material that is able to fully relax. This work predicts that, in the athermal limit where frictional forces dominate, the slow rearrangement events building to an eventual avalanche that would produce delayed banding are less likely than either the material failing quickly or not at all.

4.3 Comparisons to the SGR Model

As mentioned in Section 4.1, earlier work by the author found a linear increase in the banding time t^* under step strain with increasing age, as characterised by the waiting time $t_{\rm w}$, within the SGR model [91]. However, that study did not explore the variation in t^* with the other important variables in the SGR model: the initial imposed step strain amplitude γ_0 and the noise temperature x. The first of these can be seen in Fig. 4.12, where the variation of t^* with γ_0^2 is plotted for a range of waiting times $t_{\rm w}$. These results are qualitatively comparable to the TEP model (Fig. 4.4): as the size of the step strain decreases, the banding time increases exponentially. However, whereas in the TEP model t^* appears to diverge at a non-zero step strain amplitude γ_0, the SGR model appears to obey a simpler relationship, fitting to

$$t^* = ce^{-m\gamma_0^2}\,, \tag{4.3.1}$$

where m and c are parameters fit to the gradient and intercept respectively of the straight line when displayed logarithmically, as in Fig. 4.12.

The difference in range of imposed step strain amplitudes between Fig. 4.4 and Fig. 4.12 is a consequence of the models, with the range of energy depths E in the SGR model allowing a wide range of large step strain amplitudes to be explored. In the TEP model, all energy depths are restricted to $E = 1$, meaning any step strain significantly larger than $\gamma_0 > 1$ will cause the system to fail almost instantly, as no element will be able to sustain that strain without rapidly yielding.

The variation of t^* with $1/x$ in the SGR model is plotted in Fig. 4.13, which is comparable to Fig. 4.6 in the TEP model. The SGR model shows a Boltzmann dependence [8, 222] of t^* on temperature, with t^* diverging as $x \to 0$, fitting to the plot

$$t^* = ce^{m/x}\,, \tag{4.3.2}$$

where m and c are parameters fit to the gradient and intercept respectively of the straight line when displayed logarithmically, as in Fig. 4.13. A smaller range of $1/x$

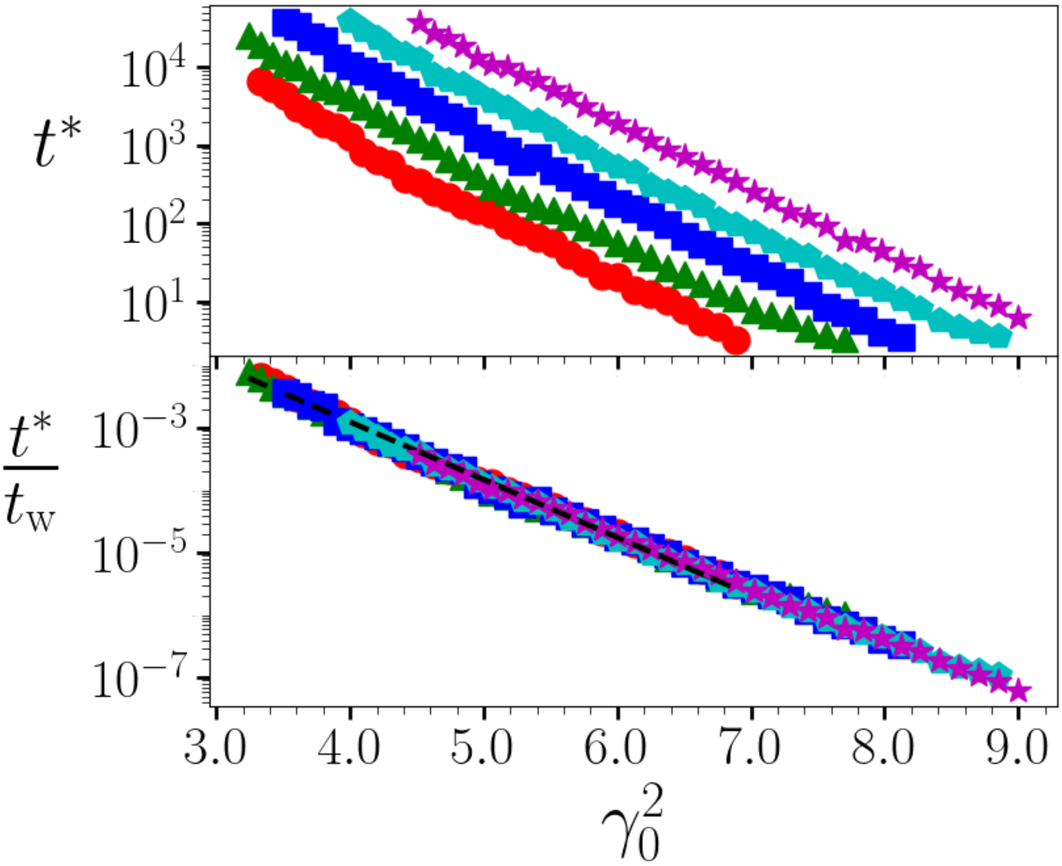

Figure 4.12: **Top panel**: The banding time t^* as a function of the square of the imposed step strain amplitude γ_0 for a working temperature $x = 0.3$, and a range of waiting times t_w=[10^6,$10^{6.5}$,...,10^8] (in order from red to purple or circles to stars).
Bottom panel: The same data, scaled by the waiting time t_w. The dashed line shows the fit to an exponential function as in Eq. (4.3.3).
Key result: t^* increases exponentially with decreasing γ_0.

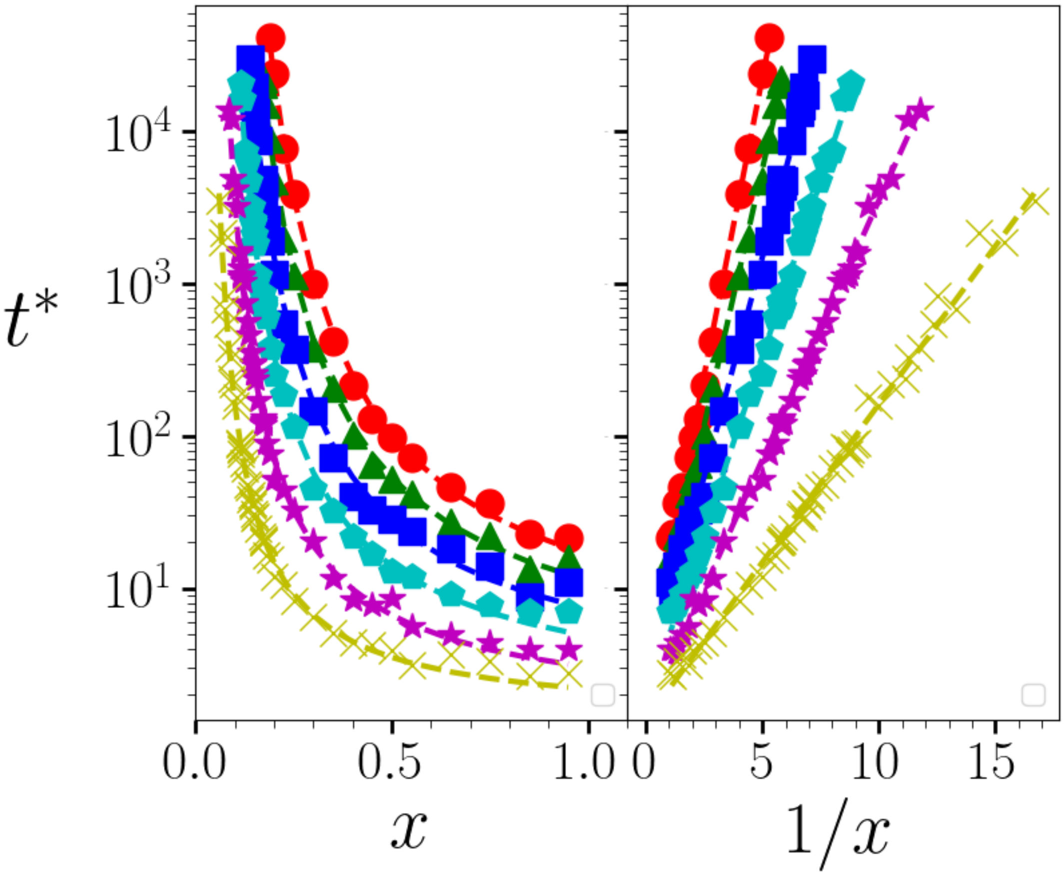

Figure 4.13: **Left panel**: The banding time t^* as a function of the working temperature x for a waiting time $t_w = 10^8$, and a range of imposed step strain amplitudes γ_0=[2.5,2.6,...,3.0] (in order from red to yellow or circles to crosses). The dashed line shows the fit to an exponential function as in Eq. (4.3.2).
Right panel: The same data, as a function of $1/x$.
Key result: t^* increases exponentially with $1/x$.

than explored in the TEP model is plotted in Fig. 4.13. This is because the SGR model does not display the same non-monotonic relationship between t^* and $1/x$ as found in the TEP model, meaning that SGR model simulations with smaller values of x result in banding times beyond the computational limit of this work.

It is possible to combine the dependence of the banding time t^* on the imposed step strain γ_0 (Eq. (4.3.1)), the working temperature x (Eq. (4.3.2)) and the waiting time t_w (work completed during the author's previous work found that $t^* \propto t_\mathrm{w}$ [91]). Note that the gradient of the lines in Fig. 4.12 remain approximately constant for a single x ($m \approx 2 = \alpha/2x$, where $\alpha \approx 1.2$) across the different values of t_w. Therefore, the behaviour of the banding time t^* can be summarised as

$$t^* = kt_\mathrm{w}e^{-\alpha\gamma_0^2/2x}, \tag{4.3.3}$$

where $k = 6.3$ is a fitting parameter and $\alpha \approx 1.2$. When the banding time t^* is plotted relative to the waiting time, as in the bottom panel of Fig. 4.12, there is good agreement with this fitting function. This functional form has precedent in the SGR model, as it has been shown that the stress relaxation after a step strain scales as $t_\mathrm{w}e^{-\gamma_0^2/2x}$ when under enforced shear homogeneity [81]. It is not surprising therefore, that when allowed shear heterogeneity, the time of the shear banding occurrence during stress relaxation is connected to this scaling.

Eq. (4.3.3) implies a divergence in $t^* \to \infty$ as $\gamma_0 \to 0$, as opposed to the non-zero divergence found in the TEP model (Eq. (4.2.2)). Any question into the quantitative difference in model response must first be prefaced by acknowledging the difficulty of numerically fitting divergences from computational data that can only be obtained over a finite range. However, as explained previously, in order to capture extremely long banding times, the TEP model requires an extremely small overlap between the strain distribution $P(l)$ and the yielding function $r(l)$. The SGR model on the other hand, has the added feature of a distribution of energy well depths E (discussed in Section 2.2). This allows even very small step strains to cause the elements in shallow wells to yield, eventually accelerating into banding after a long delay time. This makes the scenario of infinite banding times, where the probability of any yielding in the system becomes zero within computational accuracy, less likely than in the TEP model. This is a potential explanation for the difference in divergence between the two models.

Eq. (4.3.3) also implies that an athermal ($x = 0$) sample under any size step strain will never show shear banding in the SGR model. Indeed, when the SGR model is simulated with $x = 0$, there are no parameter inputs under which significant delayed shear banding can be seen (data not shown here). This correlates with the results for the TEP model at low step strain amplitudes $\gamma_0 < 1.225$ in Fig. 4.6 in which t^* appears to diverge with $x \to 0$. For higher step strain amplitudes in the TEP model, t^* resolves to a constant value with decreasing x, an effect that has only been found in the TEP model. Regardless of this slight difference, the important prediction made by both models is that highly delayed shear banding after the imposition of a step strain is not possible in the athermal $x \to 0$ limit. This finding correlates with a study of athermal systems under oscillatory shear, which found that ultra delayed yielding is only possible with a small but non-zero temperature [212]. In athermal systems, the displacement effect from a plastic rearrangement event has been shown to be large, even on elements far from the event centre [9, 47]. In the athermal limit, there is no thermal noise to smear out this spatial correlation [9, 47], meaning that athermal materials are intrinsically unstable when plastic events occur, and therefore unable to significantly delay entire system yielding [223].

The question of what happens at these extreme banding timescales and athermal limits is however secondary to the important finding of catastrophic banding events occurring at long (but not infinite times) after the initial imposition of a step strain. There is qualitative agreement between the TEP and SGR models in how the banding time t^* depends on the variation of step strain (γ_0), age/annealing (t_w/x_0) and temperature (x).

4.4 Conclusion

This chapter has shown that the TEP and SGR models both display dramatic ultra-delayed shear banding instabilities following the imposition of a step strain, in which strain suddenly strongly localises within the material, associated with a precipitous stress drop. Despite the differences in how the degree and time of this banding depend on the relevant control parameters, strong qualitative comparisons can be made between the two models. Studies prior to this work have predominantly focussed on the appearance of banding within short timescales [65–67,69,87,185–187, 213]. However, experimental evidence for the highly delayed catastrophic banding predicted in this work has been seen in a hydrogel after the imposition of a step strain [214].

A key contribution of the work in this chapter is demonstrating that the delay time of catastrophic banding after an applied step strain increases steeply with decreasing amplitude of the (long historical) imposed strain γ_0, with decreasing working temperature x, and with increasing levels of sample age and annealing prior to shear, characterised by t_{w} and $1/x_0$ in the SGR and TEP models respectively.

In addition, thorough model analysis has revealed an understanding of how shear bands forms in these models, and how changing the system and protocol parameters can alter the behaviour. The introduction of the yielding integral I, to analyse the mesoscopic element response, has allowed insight into the differences in model behaviour, and also highlighted the limitations of the models when exploring the extremes of parameter space.

Demonstrating the same basic physics within two different constitutive models (in addition to correlating studies within a Fluidity model, made by a collaborator [91]), subject to two different methods of sample annealing prior to shear (t_{w}, x_0), and with two different methods of seeding the instability with a small amplitude initial heterogeneity (Eqs. (3.1.2) and (3.1.3)), suggests that the phenomenon of delayed banding – which is directly testable experimentally and in particle-based simulations

– may be generic across amorphous materials.

This finding could be crucial for the wide range of materials that these models have been shown to simulate, from gels and emulsions [3,36–38], to domestic products such as condiments and clays [3, 37]. In the processing and production of these materials, stresses and strains are often applied, and the lack of research into the long timescale effect of a constant strain on these materials has led to an implicit assumption that the sample remains homogeneous as the stress relaxes. The fact that they can fail catastrophically with large strain heterogeneities under these conditions could have wide ranging implications for the industrial processing of amorphous materials [158].

Further work in this area could include:

- **Further theoretical study into the TEP model divergences in t^*** - Improving the efficiency of the code, perhaps with parallelization, would allow for longer simulations, pushing the maximum achievable banding time higher. This would allow more confidence in whether there truly is divergence at non-zero step strain amplitude γ_0 and pre-shear equilibrium temperature x_0. It would also be interesting to find a quantifiable connection between the critical values for these two variables, γ_{0c} and x_{0c}, beyond the assertion made in this work that when one increases the other decreases. In addition, this research has featured some critical analysis of how the TEP model functions, particularly when varying the working temperature x and analysing the value of the yielding integral I. There is scope to continue this research to allow a better understanding of behaviour in the TEP model.

- **Analytical studies with the TEP model** - The simplicity of the TEP model used means that, in the athermal limit, it can be solved analytically. Even with a non-zero temperature there is scope for other analytical tools such as linear stability analysis, which could give a mathematical perspective on the behaviours explored here.

- **Testing the conclusions made in this research with other models** - There are many different models for simulating amorphous materials. It would be particularly interesting to see if atomistic simulations [224] and other microscale models can replicate the results found in mesoscopic (SGR and TEP) and macroscopic (Fluidity) models. In addition, the generalised form of the models used so far have suggested that delayed banding might occur in a wide range of materials, but seeing this effect simulated in models designed for a specific subset of amorphous materials, such as the one outlined in Section 2.4 for breakable protein gels, could strengthen this statement.

- **Experimental studies within the protocol of step strain** - The current experimental literature on the step strain protocol is generally limited to studies on short timescale banding in polymer melts [65, 66, 185–187]. The SGR model is applicable to a much wider range of materials, such as emulsions and colloidal systems [3, 9, 13, 23–25, 37, 71, 92], and therefore this work predicts catastrophic delayed banding in these systems as well. With applications in a range of soft material manufacturing industries, it is important to test this experimentally. This is achievable by implementing a ‘rapid strain ramp’ to access the step in strain, as discussed in Section 2.5.1 [185, 186]. Some parameterisation will be required to ensure that the banding during the relaxation occurs early enough to be within experimental timescales, but also late enough to be defined as delayed as opposed to immediate failure. The most accessible variable to experimentalists studied in this chapter is likely to be the step strain amplitude γ_0, but depending on the experimental system, age and temperature could also be varied to explore the banding time. Some preliminary collaboration with experimentalists has produced some evidence of the delayed banding phenomenon under a step strain in a hydrogel [214], but there is lots of scope for further experimentation on testing materials under step strain.

Chapter 5

Creep and Failure of a Protein Gel After Imposition of Step Stress

5.1 Introduction

This chapter studies the behaviour of amorphous materials under the step stress protocol, as simulated by the Soft Glassy Rheology (SGR) model where the reformation of elements is disallowed, as described in Section 2.4. There will be a focus on the creep and failure of these systems, and how these results correlate with experimental studies on protein gels. The work presented here can be found in a pre-print [225].

The step stress protocol is the application of a constant stress, as outlined in Section 2.5.2. There is a large body of literature on the study of creep and yielding under a step stress in the computational and experimental studies of amorphous materials [9, 11, 25, 28, 36, 81, 87, 107–109, 112–116]. Theoretical models that have explored the step stress protocol include the SGR model [25, 87] and elasto-plastic models similar to the TEP model described in Section 2.3 [9, 111]. Experimental studies of the step stress protocol include materials such as colloidal gels [59, 157], microgels [36, 51], and biological collagen [19].

The initial material response to a step stress, as discussed in Section 2.5.2, is a strain that increases at an ever decreasing rate. This slowing of the strain rate often follows a power law over time $\dot{\gamma} \propto t^{-\alpha}$, $\gamma \propto t^{1-\alpha}$, where $\alpha < 1$. This phenomenon is known as Andrade creep [9, 25, 28, 36, 51, 59, 81, 87, 110–112, 114]. When the amplitude of the step stress is less than the yield stress Σ_y of the system, the decreasing strain rate creep continues indefinitely, as seen in experiments on gels [36, 157], as well as in simulations [87].

When the amplitude of the step stress is larger than the yield stress Σ_y of the system (or indeed when the system does not possess a yield stress), the creep ends with a yielding process in which the strain rate suddenly rises [9, 19, 36, 51, 111, 112]. The consequence of this yielding event is system-dependent, with some systems fluidising to a steady flow [19, 36, 51, 111], and others displaying complete material failure [110, 112]. The occurrence of shear banding during this yielding process has been predicted theoretically [67, 87] and seen experimentally [19, 36, 51, 112].

The time at which fluidisation or failure occurs under step stress is of interest, and produces several interesting phenomena universal to a range of soft systems. One example is the power law relationship between the fluidisation time and the amplitude of the step stress, also known as the Basquin law of fatigue [19,36,111,157, 226–228]. In addition, many systems under step stress display a linear relationship between the fluidisation time and the time at which the strain rate displays a minimum (the turning point between creep and yielding). This relationship is known as the Monkman-Grant relation [189], and has been seen experimentally in fibre composite materials [114], colloidal gels [157] and in fibre bundle model simulations of amorphous materials [107]. Exploring the shear banding of these systems under step stress can also explain why failure occurs, and help predict when it might occur [9, 112, 158]. This is important in a range of applications, for example when considering that landslides feature a slow build-up of strain under a gravitational stress which eventually fails with a large shear banding event [3, 4].

Previous studies of the SGR model under the step stress protocol assumed the reformation of the mesoscopic elements, which models the behaviour of a wide range of materials, including foams, emulsions, and colloids [9, 13, 23–25, 71, 92]. However, studies of protein gels under shear show a breaking of network bonds which do not instantly reform, suggesting a modification of the SGR model is needed to accurately simulate these gels [19, 27, 59, 182].

This modification, outlined in Section 2.4 and newly introduced to the field in this work, takes the framework of the SGR model but integrates the 'breaking' of elements, similar to the 'snapping' of fibres in protein gels [19, 27, 59, 182], and inspired by the failure process in fibre bundle models [9, 106]. The work in this chapter uses this model to understand the results from experimental step stress studies of protein gels [28, 110], with the eventual goal of creating an accurate physical model for the simulation of protein gels.

Protein (or biopolymeric) gels [26–32, 120] are variously defined in the literature, but are generally considered to be polymeric systems comprised of chains of amino acid residues (proteins) [120]. It is important to note that when discussing the fracturing of protein gels under shear, this is generally referring to the breakage of noncovalent bonds between cross-linked polymer strands, as opposed to the breakage of individual proteins [26,29,120]. Protein gels have applications not only in biological systems [27–30,32] but also in the food industry [31,120]. For example, the rheological properties of the protein gels in bread dough can determine loaf volume and crumb structure [121,122]. Studying the way these materials behave under a simple protocol will allow insight into how these materials fail, and under what conditions.

Protein gels under the step stress protocol display a range of phenomena, including Andrade creep, Basquin law of fatigue, and Monkman-Grant relation described above [9, 28, 110, 189]. There has been some success in modelling these effects theoretically with fibre bundle models [107, 110, 157, 227, 228], which simulate two material blocks connected by spring-like fibres [9, 106]. However, these models are incapable of the spatial dependence required to simulate heterogeneous behaviour and, consequently, shear banding [158]. This work highlights the importance of shear banding to the process of failure under step stress, correlating with that found in experiments, and therefore suggests the mesoscopic model used here to be a more accurate model for the simulating of protein gels.

This chapter also explores the build-up of heterogeneity during creep to study the precursors to failure, a topic of interest in the literature [9, 112, 158]. This is a difficult topic to study experimentally, because easily measurable macroscopic variables rarely provide insight into the spatial details of system failure [158]. Experimental procedures can study the system on a smaller scale, with such tools as light scattering and others, but are limited by resolution [27, 30, 72, 110, 112, 158, 205–207]. The simulations presented here can replicate experimental results with a high mesoscopic resolution that can provide additional insight into the behaviour leading up to failure.

All results presented in this section are from simulations using the Soft Glassy Rheology (SGR) model with element reformation disallowed, as outlined in Section 2.4. The creep and failure of these systems will be analysed through the following macroscopic rheological properties and mesoscopic strain fields that can be tracked in these simulations. These measured properties are:

- The macroscopic strain γ response to the stress-controlled protocol.
- The macroscopic strain rate $\dot{\gamma} = d\gamma/dt$ response to the stress-controlled protocol.
- The standard deviation in the strain across the system $\Delta\gamma$, which calculates the scale of the heterogeneity in the strain field $\gamma(y)$ across the shear-gradient direction y_{axis}. This effectively measures the magnitude of strain banding across the system.
- The displacement profile $U(y)$, equal to the integral of the strain $\gamma(y)$ along the shear-gradient direction y_{axis}, which gives a visual representation of the internal state of the material.

These measurements will be explored as a function of the relevant input parameters for the SGR model under the step stress protocol, which are as follows:

- The amplitude of the macroscopic imposed step stress Σ_0.
- The age of the material, given by the waiting time t_w.
- The working temperature of the system, given by the noise temperature x.

Unless specified otherwise, the following parameter values will be applied across all the simulations in this chapter:

- Working temperature $x = 0.3$.
- Number of streamlines $S = 10$, meaning shear heterogeneity across the flow gradient is allowed.
- Numerical time step $\Delta t = 0.01$.
- Solvent viscosity $\eta = 0.05$.
- Size of the perturbation in the waiting time $\epsilon = 0.1$.
- Number of elements per streamline $M = 10^5$.

All of the parameters listed above are explained in more detail in Chapter 3.

This chapter will begin by outlining the general strain and strain rate response of the system to the step stress protocol in Section 5.2. This is followed by analysis of the fluidisation time in Sections 5.3 and 5.4. Section 5.5 will analyse how well the strain rate response of the simulation matches with an experimental fitting, and Section 5.6 will provide some concluding remarks. This research finds that the SGR model, when modified to disallow the reformation of elements, provides a strong modelling tool for protein gels with results that match closely with experiments.

5.2 Strain and Strain Rate Response

The top two panels of Fig. 5.1 show the macroscopic strain γ and strain rate $\dot{\gamma}$ responses to the step stress protocol for a range of imposed step stresses Σ_0. These plots display an overall shape recognisable from other creep studies [9, 19, 28, 36, 51, 110–112, 157], described in Section 5.1 above. Upon the application of the step stress at $t = 0$ (after ageing for a time t_{w}), there is an instantaneous elastic response in the strain proportional to the applied stress $\gamma(t = 0) = \gamma_0 = \Sigma_0/G_0$ where $G_0 = 1$ (see Section 2.2.1). This instantaneous jump is seen in creep experiments [9,19,51,112,157], including in protein gels [28,110], though in this work the modulus is a dimensionless parameter set to unity $G_0 = 1$, which will not be the case in physical systems. The $G_0 = 1$ displayed here is simply a consequence of the choice of units, which is discussed further in Section 3.2. The initial strain γ_0 has been subtracted from the time-dependent strain γ in the top panel of Fig. 5.1 to highlight the behaviour after this instantaneous response.

After the instantaneous elastic response, the system begins to strain forward very slowly, with a small and decreasing strain rate. This slow straining is the origin of the term ‘creep’ used to describe this protocol. This creep regime terminates when the strain rate reaches a minimum, after which it increases suddenly, causing the strain to increase dramatically. This initial creep followed by a sudden large straining leading to fluidisation or failure is seen in a wide range of literature [9, 19, 36, 51, 111, 112], including in the experimental protein gel studies that motivate this project [28, 110].

The element behaviour that causes the macroscopic response described above can be understood by considering the elastic and plastic behaviour of elements outlined in Section 2.2.1. Upon the application of the step stress, the instantaneous element response is elastic. Therefore, immediately after the stress imposition, all element strains are equal to the imposed step stress $l_m = \Sigma_0 \ \forall \ m$ (recall from Section 3.2 that elements have modulus $k = 1$).

For elements in shallow energy wells E, this new strain means a large rate of yielding $r(l)$ and these elements will subsequently yield over a short timescale. As discussed in Section 2.2.1, when an element on a streamline yields, it relaxes its stress and causes the visco-elastic stress of that streamline σ_s to decrease, because σ_s is equal to the average of the element strains on that streamline. Considering the imposition of

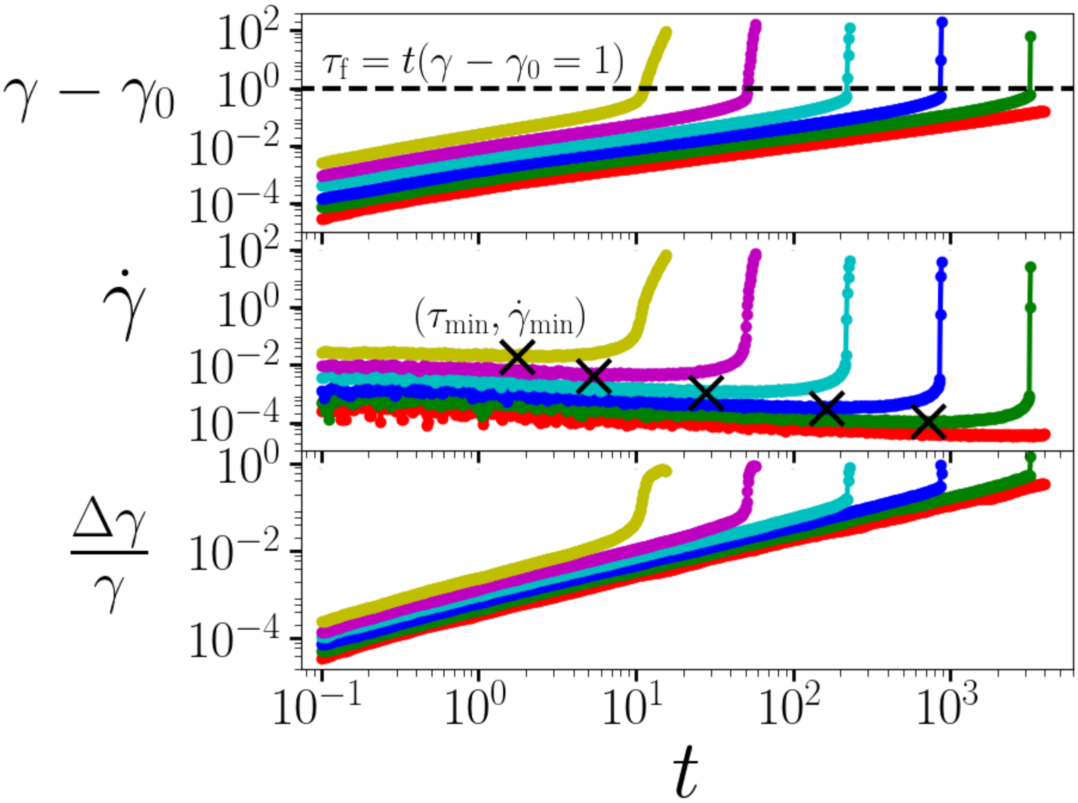

Figure 5.1: **Top panel**: The strain response γ as a function of time t following the imposition of a range of constant step stresses $\Sigma_0 = [1.0, 1.2, ..., 2.0]$ (from bottom to top or red to yellow) after a waiting time $t_w = 10^5$. γ is plotted relative to the initial strain, equal to the imposed stress $\gamma_0 = \Sigma_0$. The black dotted line highlights $\gamma - \gamma_0 = 1$. The time at which the strain reaches this value defines the fluidisation time $\tau_f = t(\gamma - \gamma_0 = 1)$.
Middle panel: The corresponding strain rate response $\dot{\gamma}$. The black crosses in the bottom panel highlight the minimum value of the strain rate $\dot{\gamma}_{\min}$, and its corresponding time $\tau_{\min}$, for each simulation.
Bottom panel: The corresponding standard deviation in the strain across the sample $\Delta\gamma$, a measure of the degree of strain banding, relative to the scale of the strain γ, as a function of time.
Key result: Simulations follow the experimental observations of primary creep followed by fluidisation.

force balance outlined in Eq. (2.2.7) and Eq. (2.2.8) ($\Sigma_0 = \Sigma_s = \sigma_s + \eta\dot{\gamma}_s$), this will cause an increase in the streamline strain rate $\dot{\gamma}_s$. The streamline will accordingly start straining forward. However, the remaining elements that have not yet yielded are in, on average, deeper traps, and so have a smaller rate of yielding $r(l)$, even though the strain is increasing. Therefore, over time the elements in shallow wells yield and only elements with deep wells remain. This causes the slowing of the initial strain rate, the creep, because fewer elements are yielding per unit time.

In the standard SGR model, the elements that yield will instantly reform and begin straining again as the system shifts forward. However, in this modified SGR model, when an element yields it breaks permanently due to the infinite timescale for reformation $\tau_{\mathrm{reform}} = \infty$, and is no longer able to support stress. This means those elements that have not yet yielded are forced to share a greater stress.

Eventually, the greater stress on the unbroken elements causes some of them to yield, which results in further forward straining. However, because these elements now have large strains, the yielding contributes a large step forward in strain for the remaining elements. This perpetuates the conditions under which they yielded, causing others to yield. This process then repeats, and consequently, over a relatively short period of time, an avalanche of yielding elements has resulted in the fluidisation of the system.

This process of fluidisation or failure, as a result of an avalanche of propagating plastic events, is seen in the accumulation of microscopic defects and crack growth in the reference protein gel experiments [28, 110].

Labelled on Fig. 5.1 are also some protocol specific measurements:

- The minimum time (called the 'dip' time in some literature), τ_{min}, defined as the time at which the strain rate as a function of time reaches a minimum $\frac{d\dot{\gamma}}{dt} = 0$ (Black crosses in middle panel of Fig. 5.1).
- The fluidisation (or failure) time, τ_{f}, given as the time at which the change in strain reaches a value $\gamma - \gamma_0 = 1$ (Black dashed line in top panel of Fig. 5.1).

These definitions are similar to those adopted in an experimental study on protein gels [110], and provide appropriate parameters with which to study the behaviour of these systems under step stress.

It is somewhat surprising that all the simulations appear to fluidise at a given value of the change in strain $\gamma - \gamma_0 = 1$, yet this behaviour is seen in protein gel experiments [110]. This implies that failure in protein gels is dependent on a macroscopic variable which can be easily measured experimentally. While it does not provide any information on how the system is failing, this finding does outline a general rule for the failure of protein gels, consistent with experimental results [110].

The fluidisation observed in these simulations is of key interest in this work. In the modified SGR model used here, once all the elements have permanently broken, the system behaves as a Newtonian fluid with a large constant steady state strain rate $\dot{\gamma} = \Sigma_0/\eta$, set by the solvent viscosity η. This resolution to a steady state is seen in creep experiments on microgels [36, 51]. However, in creep experiments on protein gels, the yielding process results in the total failure of the system [28, 110]. The difference is that stresses arising through the viscosity of the experimental solvent that the protein gel bonds within are likely to be very small compared to the elasticity of the gel bonds themselves. Therefore, the stress required for the gel to fluidise will cause a large steady state flow rate for the solvent, so high in fact, that it is likely the experimental setup fails before that limit is reached. The simulations, on the other hand, have no upper limit to stress. In addition, the experimental sample is likely to physically break apart upon failure with air entering these cracks, and inertia may start to play a role. The introduction of a third medium and inertia effects are not considered in the model.

However, the interesting physics is not in the behaviour of the solvent, so the simulations have been cut-off before the full fluidisation. Despite the cut off, the effects of this fluidisation can still be seen in Fig. 5.1 in the very large values of strain and strain rate, particularly in the simulations performed at a larger imposed step stress Σ_0. It is important to note this effect, because it will have relevance when trying to fit the fluidisation to an experimental model in Section 5.5.

So far, only the globally observed strain γ and strain rate $\dot{\gamma}$ responses have been considered. An additional question concerns whether shear banding, as discussed in Chapter 1, occurs during this failure and fluidisation process. The bottom panel of Fig. 5.1 plots the standard deviation in strain across the sample $\Delta\gamma$, effectively measuring the strain banding. This measurement of the degree of banding rises sharply during the fluidisation process, reaching the same order of magnitude as the overall strain before the cut-off. The presence of shear banding is confirmed by Fig. 5.2, which plots the normalised displacement profile $U(y)$ observed in one of the simulations seen in Fig. 5.1 ($\Sigma_0 = 1.6$ and $t_\mathrm{w} = 10^5$). Initially, and during the primary creep (from blue to yellow), the displacement profile is a straight line, showing homogeneous shearing across the system. However, during the fluidisation (orange to red), the displacement profile becomes non-linear, the strain profile becomes highly heterogeneous, and shear banding is clearly visible.

Shear banding during the fluidisation of amorphous materials under an imposed step stress is well established [9, 36, 111], including in the reference protein gel studies [28, 110]. This has also been predicted under linear stability analysis, which suggests that the occurrence of these shear localisation effects during fluidisation under step stress is fluid-universal, independent of the constitutive law and internal state variables of the particular fluid [67, 87]. Therefore, any theoretical study of the fluidisation of systems under step stress must have the capacity for displaying shear banding, which is lacking in the theoretical fibre bundle model simulations conducted so far [158]. Fig. 5.2 shows how the work in this thesis can simulate the shear banding in protein gels predicted theoretically [87] and seen experimentally [28, 110].

The shape of shear banding in Fig. 5.2 is sinusoidal, which is a consequence of the form of the imposed perturbation, as outlined in Section 3.1.2. In the SGR model, the waiting time experienced by each streamline is perturbed by a cosine function across streamlines (along the flow gradient direction y_axis), as in Eq. 3.1.2. This means the weakest area, corresponding to the most poorly aged, is at the centre of

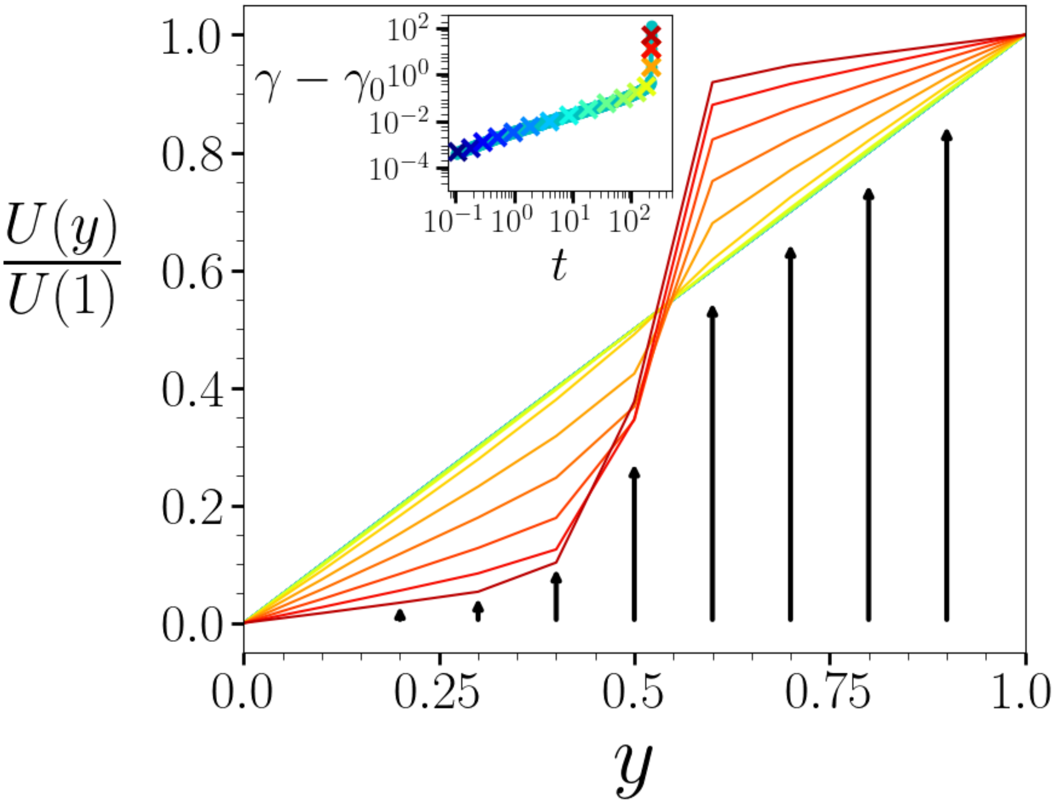

Figure 5.2: The displacement profile $U(y)$ normalised by its value at $y = 1$ as a function of the distance along the flow gradient y for a simulation with $\Sigma_0 = 1.6$ and $t_{\mathrm{w}} = 10^5$. The colour change of blue to red or increasing heterogeneity signifies increasing time. The normalisation is used to show the homogeneous profile and the heterogeneous banded profile on the same scale, as $U(1) = \gamma$. Highlighted by the black arrows is the flow direction x_{axis}. The inset shows the macroscopic strain response γ of the same simulation, with crosses whose colour corresponds to the time at which the lines in the main figure are taken.
Key result: Fluidisation of the system is accompanied by large scale banding.

the system. Consequently, the failure of the system and the separation of the shear bands is most likely to originate there, which can be seen in Fig. 5.2.

Experiments on protein gels found the origination of cracks on the outer edges of the material which eventually propagate through the middle of the system at the point of failure [110]. Therefore, the eventual failed system of the simulations is similar to that in experiments, with differences in the way the shear banding builds. The way the perturbation is applied defines the shape of the perturbation, as can be seen in Chapter 4, where the use of a different perturbation in the Thermal Elasto-Plastic model causes a different shear banding shape. Therefore, future work could consider how the perturbation changes the shape of the heterogeneity that arises during shear, and whether this could be tuned to more closely model experimental observations. In addition, the experimental study found crack propagation along the vorticity direction z_{axis}, so an expansion to 2D could also improve analysis of how the shear bands form.

Sample preparation, in both experimental and theoretical studies, including how intrinsic material heterogeneity is modelled in a system, has a significant impact on the failure of systems [161, 201–203]. However, despite the small differences in shear banding shape, the behaviour of the simulations closely matches that seen experimentally in protein gels [28, 110]. In addition, the large scale of the banding, with $\Delta\gamma$ increasing to the order of the overall strain γ before the cut-off, is likely to result in the material failure present in experiments [28, 110]. Therefore, this modified SGR model is shown to be a strong candidate for simulating the shear banding and failure of protein gels under the step stress protocol.

5.3 Fluidisation Time

A key variable of interest in this research is the fluidisation (or failure) time τ_{f}. This is plotted in Fig. 5.3 as a function of the imposed step stress Σ_0 for a number of different waiting time t_{w}. It can be seen that τ_{f} increases with decreasing Σ_0, as found experimentally for protein gels [28,110] and other systems [19,36,111,157,226]. This can be understood within the model. A small imposed stress causes the elements to have small initial strains, and hence a small rate of yielding $r(l)$, as in Eq. 2.2.3. The fluidisation of the system requires an avalanche of yielding, as described above, and hence this will take longer at smaller imposed stresses.

The left panel of Fig. 5.3 shows a linear behaviour on the log-log scale for the lower values of Σ_0 which corresponds to a power law dependence of τ_f on Σ_0. Noting the collapse of simulations with different ages given by the waiting time t_w, it can be seen that $\tau_\mathrm{f} \propto t_\mathrm{w}\Sigma_0^\beta$, where β is the power law gradient. This power law behaviour appears in many creep studies [19,36,111,157,226], including in protein gels [28,110] and is reminiscent of the Basquin Law of Fatigue, originally discussed in the context of solids but since found in many soft materials [157,227,228].

This power law implies that the system will fail catastrophically under any stress, however small. Therefore, even a very small applied stress will eventually cause the material to fail, albeit on extremely long timescales. This conclusion could have important implications for industries that utilise protein gels, particularly where long timescales are involved, given that materials are inevitably subject to gravitational stresses at least.

The divergence in the fluidisation time τ_f in the limit of zero step stress $\Sigma_0 \to 0$ is seen in experiments on protein gels [110]. However, in another study on a different protein gel, τ_f diverges at a step stress equal to a yield stress $\Sigma_0 = \Sigma_\mathrm{y}$ [28], behaviour that is also seen in colloidal gels [157] and microgels [36]. This work suggests that the difference lies in the timescale for reformation τ_reform in these systems. When the SGR model is simulated with instantaneous reformation $\tau_\mathrm{reform} = 0$, the fluidisation time τ_f diverges as Σ_0 approaches Σ_y from above, where Σ_y is a non-zero yield stress [87]. In the work presented here there is no yield stress, due to the permanent breaking of elements $\tau_\mathrm{reform} = \infty$. The study that showed a protein gel with a yield stress discusses a long but non-infinite timescale for reformation during shear [28], whereas the study on a protein gel with a divergence at zero discusses irreversible crack and

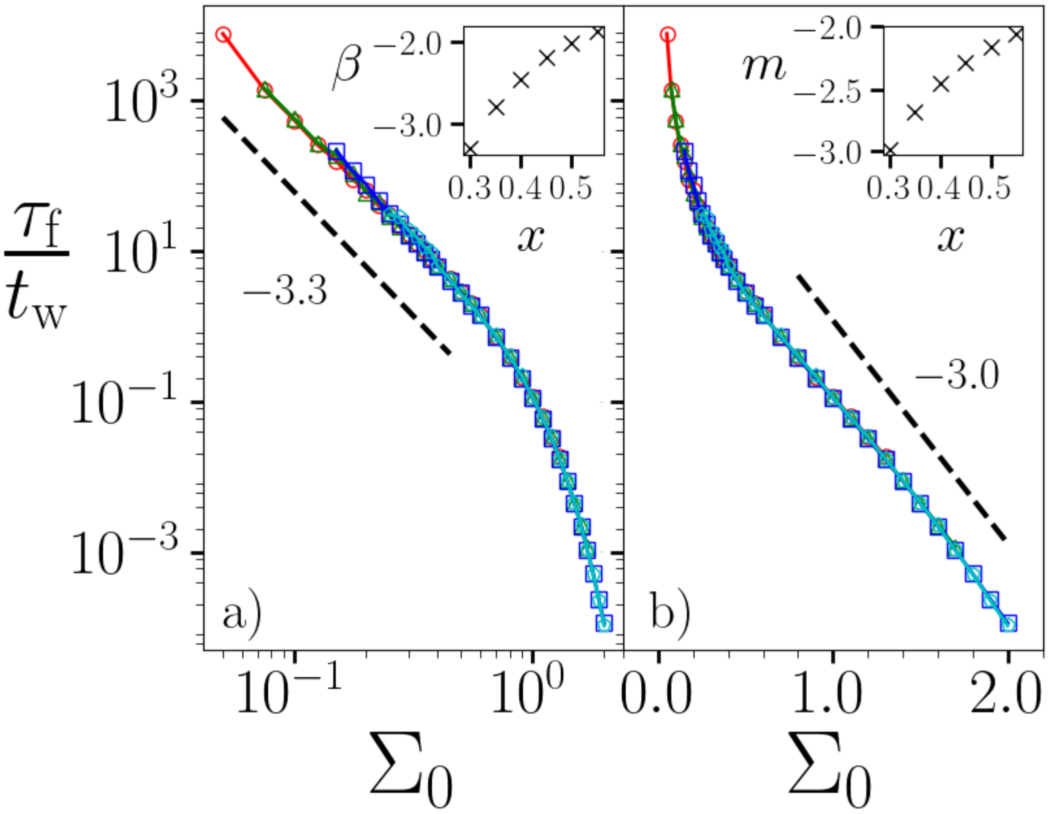

Figure 5.3: The fluidisation time τ_f as a function of the imposed step stress Σ_0, for a range of simulations over waiting times $t_w = 10^3$ - red circles, $t_w = 10^4$ - green triangles, $t_w = 10^5$ - blue squares, $t_w = 10^6$ - cyan pentagons, at noise temperature $x = 0.3$.
Left Panel: On a log-log scale, τ_f displays a power law dependence for small Σ_0. The exponent of this power law, β, is indicated by the black dashed line. The inset shows how this gradient β varies with noise temperature x.
Right Panel: On a log-linear scale, τ_f displays an exponential law dependence for large Σ_0. The exponent of this exponential law, m, is indicated by the black dashed lines. The inset shows how this gradient m varies with noise temperature x.
Key result: τ_f displays a Basquin law dependence on Σ_0.

fracture growth [110], implying an infinite timescale for reformation $\tau_{\mathrm{reform}} = \infty$, as considered in the simulations in this work. This highlights the timescale for reformation τ_{reform} as an important variable when simulating protein gels. To the author's knowledge, this is the first study to consider the variation of τ_{reform} in the context of mesoscopic models. Values of τ_{reform} outside of zero and infinity are not studied in this work, but their potential effects are discussed in Section 5.6.

In the right panel of Fig. 5.3, a change of scale allows observation of a different fitting. It is clear that the behaviour of τ_{f} at larger values of Σ_0 follows an exponential law of the form $\tau_{\mathrm{f}} \propto t_{\mathrm{w}} e^{m\Sigma_0}$, where m is the exponential law gradient. This two-region effect for the dependency of the fluidisation time τ_{f} on the imposed stress Σ_0 is seen in experiments on protein gels [28], as well as theoretical and experimental studies on colloidal gels [116, 157, 229]. This exponential decrease of τ_{f} with increasing Σ_0 implies that at large values of imposed step stress, the material will fluidise or fail quickly, as might be expected intuitively.

The influence of the working temperature x on the fluidisation time τ_{f} can be seen in the insets of Fig. 5.3. In particular, the exponent of the power law (β) and exponential law (m) become less negative (the gradient decreases) with increasing temperature. This is logical because a smaller temperature will result in less activation of yielding and therefore delay the eventual fluidisation. The temperature will also affect the ageing of the material, with a larger temperature resulting in a broader distribution of element energy depths E, as discussed in Section 3.1.1. In some protein gels, the temperature can have a significant effect on ageing in systems with long but finite reformation timescales τ_{reform} [28]. In this work, the impact of a smaller working temperature x during the ageing and subsequent stress application causes the fluidisation time to be delayed.

The effect of the age of the system prior to shear, represented in the SGR model by the waiting time t_{w}, on the fluidisation time τ_{f} can be seen in Fig. 5.3. It is found that $\tau_{\mathrm{f}} \propto t_{\mathrm{w}}$. This direct proportionality implies that as the age of the system increases, the fluidisation time is delayed. This relation is alluded to by another theoretical study, which found that an increased system age will delay system failure, but not with the detail or range of input variables covered here [158]. Although the ageing or annealing of a system is not always easy to control experimentally, it clearly has a significant effect on the failure of these systems under creep. One option is to look at the gelation process, as discussed in Section 3.1.1 where a strongly connected gel is similar to a well-aged system, or indeed the time allowed for gelation as comparable to the waiting time [51].

This section has shown clear dependencies of the fluidisation time τ_{f} on the applied step stress Σ_0, working temperature x, and waiting time t_{w} for breakable gels.

5.4 Fluidisation Time and Minimum Time Relationship

The relationship between the minimum time τ_{min}, the time at which the macroscopic strain rate response $\dot{\gamma}$ reaches a minimum, and the fluidisation time τ_{f}, is plotted in Fig. 5.4. Also plotted is a fitting from experimental results on protein gels, which found $\tau_{\mathrm{min}} = 0.56\tau_{\mathrm{f}}$ [110]. There is good agreement between the two results, particularly for the larger values of τ_{f}. This correlates with the results found in Fig. 5.3, where the large values of τ_{f} in the left panel matched the power law found in [110]. This linear relationship between τ_{min} and τ_{f}, also known as the Monkman-Grant relation [189], is also seen experimentally in other gel systems [114, 157].

It is sometimes claimed in the literature that failure is not possible to detect through macroscopic variables, such as strain and stress [158]. While it can be argued that by the time a shear rate minimum is reached, the system is already failing, the Monkman-Grant relation can give powerful predictive powers when monitoring the failure of materials undergoing creep. This suggests that once a minimum time has been measured, the time of fluidisation or failure can be estimated.

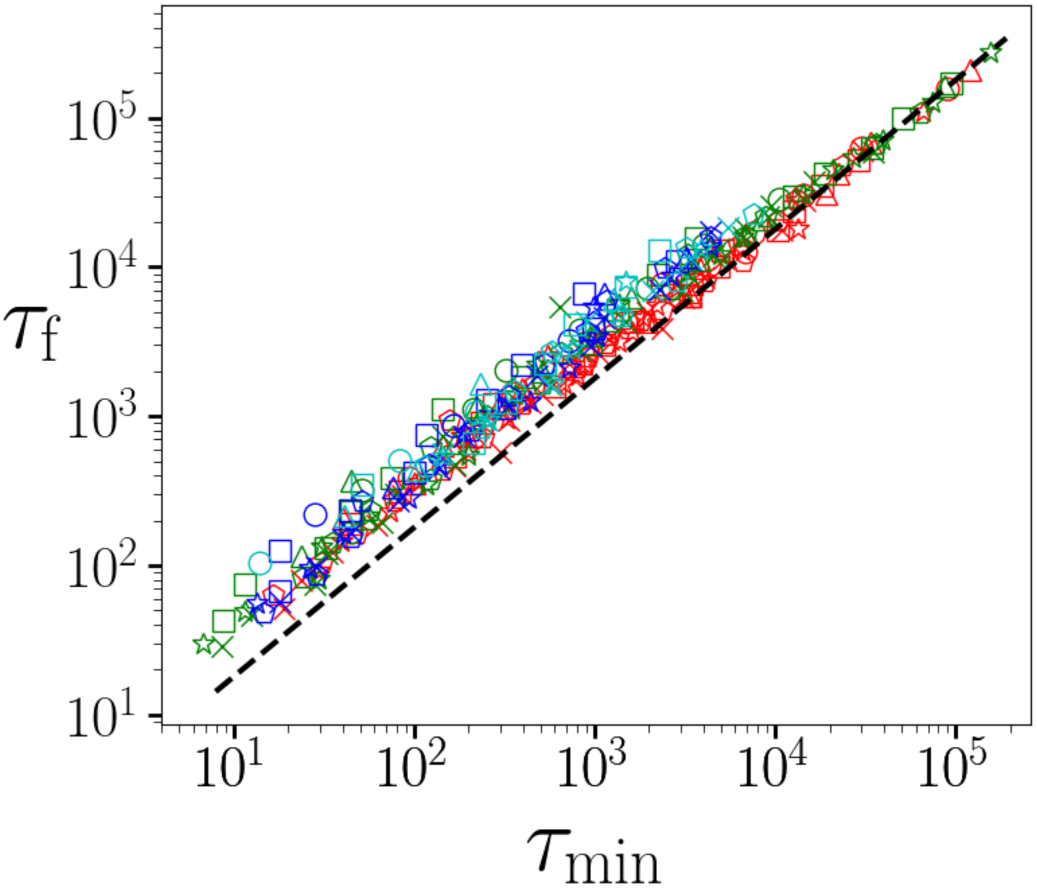

Figure 5.4: The relationship between the fluidisation time τ_{f} and the minimum time τ_{min} for a range of simulations over noise temperatures $x = 0.3$ - circles, $x = 0.35$ - triangles, $x = 0.4$ - squares, $x = 0.45$ - pentagons, $x = 0.5$ - stars, $x = 0.55$ - crosses, waiting times $t_{\mathrm{w}} = 10^{3}$ - red, $t_{\mathrm{w}} = 10^{4}$ - green, $t_{\mathrm{w}} = 10^{5}$ - blue, $t_{\mathrm{w}} = 10^{6}$ - cyan, and imposed step stresses $\Sigma_0 = [0.05, 0.1, 0.15, ..., 2.0]$ (from right to left in coloured symbols). Each symbol corresponds to a single simulation. The black dashed line shows the result from experimental protein gel literature [110]. **Key result**: τ_{f} displays the Monkman-Grant relation with τ_{min}.

5.5 Primary, Secondary, and Tertiary Creep Regimes

The three creep regimes in the strain rate $\dot{\gamma}$ response of the system to a step stress, as simulated by the modified SGR model, are shown in Fig. 5.5. A fitting from experimental results for a protein gel [110] is also plotted. The fit is the superposition of two physical processes

$$\frac{\dot{\gamma}}{\dot{\gamma_{\mathrm{min}}}} = \underbrace{\lambda \left(\frac{t}{\tau_{\mathrm{f}}}\right)^{-\alpha}}_{\text{Primary Creep}} + \underbrace{\frac{\mu}{1 - t/\tau_{\mathrm{f}}}}_{\text{Fracture Growth}} \quad . \tag{5.5.1}$$

In this equation, the first term on the right-hand side represents the aforementioned primary creep with exponent $\alpha = 0.3$ in Fig. 5.5. The second term, which models a divergence in $\dot{\gamma}$ as $t \to \tau_{\mathrm{f}}$, corresponds to the final growth of the fractures leading to material failure [110]. λ and μ are fitting parameters, which for the data in Fig. 5.5 take values $\lambda = 0.35$ and $\mu = 0.4$. Exploring how these fitting parameters depend on the model and protocol variables is not within the scope of this project, but is discussed as a potential topic for future work in Section 5.6.

The top panel of Fig. 5.5 highlights primary creep, and shows a good fitting to Eq. (5.5.1) in this regime. This power law creep $\dot{\gamma} \propto t^{-\alpha}$, also referred to as Andrade creep [9, 28, 36, 51, 110, 114], represents a progressive slowing of the dynamics over time, with a gradual decrease in the strain rate $\dot{\gamma}$. Andrade creep has been seen in numerous creep experiments and simulations [25,27,28,36,51,59,81,87,111,112,114]. The fitting matches $\alpha \approx x$, a result seen in other simulations of the original SGR model in which elements are allowed to reform [25,87]. This is interesting, and implies that primary creep is predominantly a cause of elements that have yielded once, or not at all. This is logical, as the strain rate is small during primary creep, such that even if a yielded element did reform, its strain would be unlikely to subsequently reach a value where its yielding rate is significant. The primary creep exponent α is also independent of the age of the material, given by the waiting time t_{w}. The

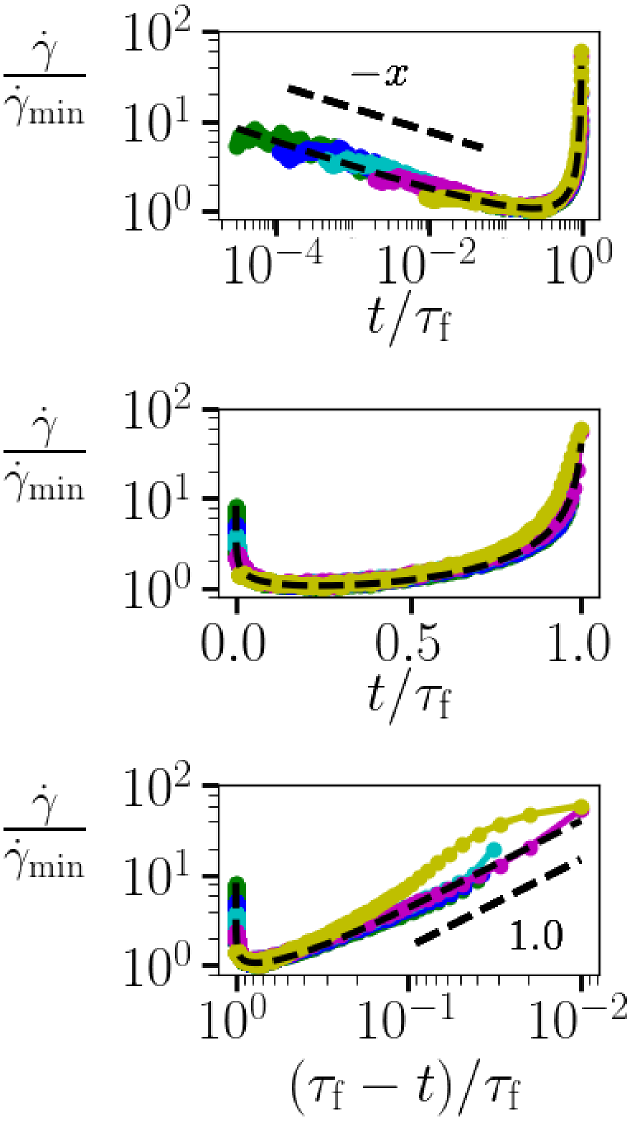

Figure 5.5: The strain rate $\dot{\gamma}$ normalised by its minimum $\dot{\gamma}_{\rm min}$ for the simulations presented in Fig. 5.1 where $t_{\rm w} = 10^5$ and $x = 0.3$. The range of constant step stresses $\Sigma_0 = [1.2, 1.4, ..., 2.0]$ are represented by the same colours as that in Fig. 5.1 (from green to yellow or left to right in the starting strain rate). Note that the $\Sigma_0 = 1.0$ simulation in Fig. 5.1 (red line) is not shown here because it does not reach its fluidisation time within the allowed computational time. The black dashed line shows a fitting of the same form used to fit experimental results (Eq. (5.5.1)) [110].

Top Panel: On a log-log scale to highlight the primary creep.

Middle Panel: On a log-linear scale to highlight the secondary creep.

Bottom Panel: On a reversed log-log scale to highlight the tertiary creep.

Key result: Simulations display the experimentally observed three creep regimes.

lack of influence of material age on primary creep has been shown in experimental studies on microgels and colloidal gels [51, 59].

The secondary creep regime is highlighted in the middle panel of Fig. 5.5 and shows a good fitting to Eq. (5.5.1) for $t \lesssim 0.9\tau_{\mathrm{f}}$. In this regime, there is a departure from power law creep, with the strain rate reaching a minimum at time τ_{min}, after which it starts to increase. There is significant evidence in the literature for this quasistationary creep where heterogeneity begins to form within the material [9, 19, 110, 114, 158]. This behaviour can be seen Fig. 5.2, where the colours that represent the times where the strain begins to curve upwards in the inset (light green to light orange) show a displacement profile $U(y)$ that is beginning to increase in heterogeneity.

The final regime is highlighted in the bottom panel of Fig. 5.5. The aforementioned indicators of material failure during secondary creep suddenly accelerate, leading to full macroscopic rupture or fluidisation. This is called the tertiary creep regime, appearing for times $t \gtrsim 0.9\tau_{\mathrm{f}}$ [110, 157]. The shear rate diverges as $(\tau_{\mathrm{f}} - t)^{-1}$ and the presence of shear banding is clear in Fig. 5.2, where the colours that represent the times where the strain is rising rapidly in the inset (orange to red) show a displacement profile $U(y)$ that is highly heterogeneous. This corresponds to the large positive and negative velocities present in the velocity profiles of protein gel experiments during tertiary creep [110]. It is this catastrophic shear banding, with a scale on the order of the strain γ, that causes the experimental systems to fail [28,110].

The deviation between the simulations and the fitting in this regime is interesting. The clearest difference between the simulations and the fitting appears in the $\Sigma_0 = 2.0$ simulation, but all the simulations begin curving away from the fitting during the tertiary creep regime. This is due to the difference in fluidisation, as discussed in Section 5.2. Approaching fluidisation, the simulations tend towards the large but finite constant strain rate $\dot{\gamma} = \Sigma_0/\eta$ of the Newtonian solvent with viscosity η. The experimental fitting, on the other hand, diverges to an infinite strain rate as $t \to \tau_{\mathrm{f}}$. There have been studies that show the substantial effect the solvent viscosity can have on crack growth, where increasing the solvent viscosity can suppress the development of fractures [10,31]. Therefore, it is possible that the simulations would better fit Eq. (5.5.1) with zero viscosity $\eta = 0$. Indeed, the strain rate of the Newtonian fluid that the simulations resolves to $\dot{\gamma} = \Sigma_0/\eta \to \infty$ as $\eta \to 0$. It is possible to implement $\eta = 0$ in the SGR model, as described in Section 2.2.3, and so this hypothesis can be tested. However, this is outside the scope of this project.

This detailed study into the three creep regimes of the macroscopic strain rate response $\dot{\gamma}$ show a good fitting to experimental results for protein gels [110], outside of the behaviour just before failure.

5.6 Conclusion

In this chapter, the SGR model, modified to disallow reformation of elements, has been used to study the creep and failure of irreversibly breakable gels under the step stress protocol. The modification, inspired by fibre bundle models [9, 106], aims to simulate the permanent breaking of fibres in protein gels under shear [19, 27, 59, 182]. This work expands beyond prior SGR model studies that focus on systems in which the mesoscopic substructures reform after yielding [25, 81, 87], and also beyond fibre bundle models unable to simulate shear banding [158].

The simulations produce results that correlate well with experimental studies [28,110]. This includes good fittings to the Basquin law of fatigue [227, 228], primary Andrade creep [9, 28, 36, 51, 110, 114], Monkman-Grant relation [189], and the three creep regimes of the strain rate response (Eq. (5.5.1)) [110, 157]. In addition, studying the behaviour of the mesoscopic SGR elements and the strain profile across the material shows a slow building of heterogeneity during primary creep, which then avalanches into the catastrophic shear banding that leads to the fluidisation or failure of these systems. This allows insight into the precursors to failure under creep, which is of interest in the literature [9, 112, 158].

The SGR model therefore appears a strong candidate for modelling the behaviour of these protein gels, and for interpreting experimental results. In addition, the results presented here, along with their experimental counterparts, provide a good understanding of the behaviour of protein gels under step stress, which are important in both biological systems [27–30, 32] and the food and cosmetic industries [27, 31, 120–122].

Further work in this area could include:

- **Exploration of other protocols using this modified SGR model** - Studying this model under shear startup [9, 67, 71, 87], oscillatory shear [41, 159, 208–211], and other rheological protocols could reveal further interesting phenomena and discoveries on how protein gels might react to other stimuli.
- **Comparing the results presented here to the same simulations but setting $\eta = 0$** - The agreement between the simulations and experimental fitting in Fig. 5.5 could be improved by simulating the SGR model with zero solvent viscosity $\eta = 0$, as described in Section 2.2.3. In addition, once the simulations more closely match the experimental fitting, the system dependencies of the fitting parameters λ and μ could be explored, as discussed in Section 5.5.
- **Changing the perturbation** - As discussed in Section 5.2, the perturbation that seeds strain heterogeneity is not expected to significantly impact the fluidisation time τ_{f}. However, the shape of the shear banding in Fig. 5.2 is a direct consequence of the shape of the perturbation. In addition, sample preparation is increasingly being recognised as an important factor in rheological behaviour [161, 201–203]. Consequently, experimenting with the shape and size of the perturbation could provide some interesting points of discussion for how, why and where the shear banding forms, beyond those discussed here.
- **Varying the reformation timescale τ_{reform}** - The SGR model has been simulated here for $\tau_{\text{reform}} = \infty$, effectively disallowing elements to reform after

yielding (see Section 2.4). In all previous studies of the SGR model, elements have reformed instantly after yielding $\tau_{\text{reform}} = 0$. There is therefore scope in future studies to vary this parameter and explore the consequences of a long but non-infinite reformation time. As discussed in Section 5.3, this would give the system a yield stress, as the reformation of elements can then delay the fluidisation time τ_{f} indefinitely for a small enough stress. This could cause a divergence in the fluidisation time at a non-zero stress, which would match some experiments on protein gels, which found that bonds can reform broken strand connections under strain, but can only do so over long timescales [28]. The reformation timescale τ_{reform} could then be tuned to accurately model the specific type of gel. In addition, this would also alleviate the need for a discontinuity of τ_{reform} at $t = 0$ (discussed in Section 3.1.1), as the ageing process can be simulated as long as τ_{reform} is finite.

- **Investigating other ways to add specificity to the SGR model** - One of the SGR model's biggest strengths is its generality, its ability to apply its findings to a wide range of amorphous materials. However, this project highlights the ability to innovate with the model and increase the specificity of the model to apply to a more complex group, protein gels. This is not the only way the SGR model could be adapted to apply to more specific material types, for example, a different energy well landscape could be used, and exploring this could expand the strength of the SGR model as a tool for simulating amorphous materials.

- **Expanding the simulation dimensionality** - This work has shown the power of the SGR model in simulating the failure of protein gels, even when spatial variations are allowed only in the flow-gradient direction y_{axis}. However, as discussed previously, experimental analysis into the tertiary creep regime found fracture growth along the vorticity direction z_{axis} [110]. Therefore, simulating the SGR model with the no element reformation modification in 2D or 3D could more accurately reproduce the formation of shear bands found in experiments.

Chapter 6

Recoverable Strain and Reversible Plasticity Under Creep-Recovery Test

6.1 Introduction

This chapter studies the behaviour of amorphous materials under the creep-recovery test protocol. The Soft Glassy Rheology (SGR) model is used, which provides a generalised description for studying the response of these materials. There will be a focus on the amount of strain the system is able to recover, how the relaxation can exhibit non-monotonicity, and the origins of this recoverable strain.

The amount of strain that a system can recover after shearing, the recoverable strain, is widely studied for protocols including oscillatory shear [126, 143, 144], shear startup [57, 153], and the protocol studied in this chapter: the creep-recovery test [50, 53, 77, 123]. In these studies, the imposition of shear is removed after some time, the system subsequently recovers by straining in the opposite direction to that of the strain acquired during shearing. The degree of recoverable strain is shown to correlate with the temporal evolution of microstructure under shear, where rearrangements can affect recoverability [144]. Under the creep-recovery test protocol, it has also been suggested that the recoverable strain can aid in analysing the material behaviour that leads to fluidisation [143]. Recoverable strain is a particularly important property in hydrogels, with many studies on these materials into the conditions under which recoverable strain is maximised [52–55, 127, 130, 131]. Hydrogels have applications in tissue engineering, vehicles for drug delivery, and actuators for optics and fluidics [52]. Understanding their material properties is therefore of high importance.

The recoverable strain of a system also provides an indication of the overall propensity of a material towards elastic deformation or viscous flow [53, 129]. Elastic straining is, by definition, reversible and therefore recoverable [61, 162]. Small scale deformations, such as to the configuration of a cluster of particles, are generally elastic [147–149]. Plastic events, such as the large scale rearrangement of a cluster of particles [49, 62], cause straining that has been assumed to be irrecoverable [45, 125, 152, 190, 214]. This work will show evidence to contradict this assumption. The strain gained in the system through plasticity during shear is reversible, in a process comparable to reversible plasticity [58, 135–139, 145–151].

Reversible plasticity is a topic gaining interest in the amorphous materials literature [58, 135–139, 145–151]. It has generally been found to occur on the microscale and mesoscale [58, 145, 147, 149, 150], where a group of particles or molecules that plastically rearrange under a forward strain can return to their original configuration when a backwards strain is subsequently applied via a secondary path different from the initial rearrangement [147–149]. It has been suggested that this small-scale reversible plasticity only translates to irreversible macroscopic plastic flow when the elastic regions surrounding the plastic zones fail [149]. This implies that the number of plastic events in a system must remain small, and the surrounding behaviour predominantly elastic, for the plasticity to be on a scale necessary to be reversible.

The study of reversible plasticity is common in the shape memory polymer literature, where a specific class of materials called reversible plasticity shape memory polymers have been developed [135–139]. Reversibility can be activated, such as by shear, temperature or submersion in water [135, 136, 138, 139], the latter an effect that has also been seen in a hydrogel [146]. These systems have applications in self-healing materials, where cracks or fractures in a material can be repaired [135, 136, 138, 139].

Theoretical studies into reversible plasticity have primarily studied the process under oscillating shear, where the regularly reversing nature of the protocol assists in the creation of reversible plastic events [58, 147–150]. Indeed, to the author's knowledge, this is the first theoretical exploration of reversible plasticity in amorphous materials under the creep-recovery protocol.

A study of reversible plasticity in solid copper [145], a crystalline solid, highlighted its connection to the Bauschinger effect, where the material's stress/strain characteristics change as a result of the microscopic stress distribution of the material [230–232]. A common example of this effect is an increase in tensile yield strength occurring at the expense of compressive yield strength [232]. While this effect is generally attributed to solid materials, there is experimental evidence for the presence of the Bauschinger effect in soft amorphous materials such as in dense suspensions [78, 233]. Theoretical studies have considered its origins in glassy and polymer systems [8, 79, 234–236], such as in the alignment of covalent bonds [234]. However, none of these studies make the connection between the Bauschinger effect and reversible plasticity that is made here, inspired by the insights from the study into copper mentioned above [145].

The protocol studied in this work, the creep-recovery test, involves the application of a step shear stress for some time before it is switched off and the relaxation of the strain is studied [123], as outlined in Section 2.5.3. It has been explored experimentally for a range of materials including colloidal systems [59, 77], microgels [50], shape memory polymers [136], and the protein gels studied closely in Chapter 5 [152]. The theoretical studies of this protocol are generally specific to the material, with simulations for concrete [124] and cold-set gels [125] in the literature, which both predict significant recoverable strain for these systems. This work aims to explore the phenomenon of recoverable strain under the creep-recovery test protocol for a more generalised model, with the aim of making predictions that apply generically across a range of materials.

The work in this chapter studies the behaviour of amorphous materials under the creep-recovery test as simulated by the SGR model with shear homogeneity enforced, outlined in Section 2.2.1. A lot of the early work in the SGR model used enforced homogeneity in shear. Indeed, even within these simplifying assumptions, the model is able to explore many phenomena shown in amorphous materials [71, 81, 92]. However, when behaviour is likely to involve significant material heterogeneity, enforced shear homogeneity is no longer an appropriate approximation [13, 24, 25]. For this reason, it is important to note that the results presented in this chapter are only relevant physically under conditions where the influence of heterogeneity in shear is minimal.

The influence of shear heterogeneity is likely to be most important during the creep portion of the creep-recovery test, where a constant stress is applied. The creep protocol is explored thoroughly in Chapter 5, and finds that under the primary creep regime, minimal shear heterogeneity forms. This finding is replicated in many creep studies, where significant heterogeneity in shear only builds up during the secondary and tertiary creep regime, as the material moves towards failure [25, 27, 28, 36, 51, 81, 87, 111, 112, 114, 157]. Experiments concerning the creep-recovery test generally stay in the primary creep regime, because after the full failure or fluidisation of the material there is unlikely to be any significant strain recovery [50, 77, 152, 157]. Therefore, the SGR model with enforced homogeneity in shear is predicted to be a good candidate for modelling the creep-recovery test protocol, as long as the system remains in the primary creep regime during the stress application.

It is also important to acknowledge that a build-up of shear heterogeneity can also occur during relaxation, as explored in Chapter 4. Although the creep-recovery test is a stress-controlled protocol, the results from Chapter 4 in the step strain protocol can provide insight into the conditions under which significant heterogeneity in shear can form during relaxation. For small strains $\gamma_0 < 2$, significant shear heterogeneity in the SGR model occurs only over extremely long timescales, before which the relaxation is generally homogeneous in shear. Therefore, as long as the values of strain remain small, the relaxation should also stay homogeneous in shear. Indeed, this condition is also enforced by remaining in primary creep, as Chapter 5 revealed that, under a shear stress, a system approaching a change in strain larger than $\gamma - \gamma_0 \approx 2$ is likely to be outside the primary creep regime. Therefore, enforced homogeneity in shear is likely to be an appropriate approximation for this work under these conditions. The introduction of heterogeneity in shear into the model is suggested for future work in Section 6.7.

An important benefit of enforced shear homogeneity is the simplicity of the simulations, allowing a full analysis into the complex relaxation behaviour that occurs under the protocol for the various input parameters. With substantial recoverable strain discovered, including some interesting non-monotonic behaviour, this work lays the foundations for the SGR model to become a tool for modelling the recoverability of amorphous materials. In addition, the exploration of reversible plasticity in SGR model systems could change the established understanding on the origins of recoverable strain.

Because the creep-recovery test is a stress-controlled protocol, the creep and recovery of these systems will be analysed primarily through the macroscopic strain $\gamma(t)$ response. Note that because there is enforced shear homogeneity (through restricting the system to one streamline $S = 1$), there is no shear heterogeneity in the flow-gradient direction y_{axis}, hence there is no analysis of standard deviations or strain profiles, in contrast to previous chapters.

These strain γ measurements will be explored as a function of the relevant input parameters, these being:

- The amplitude of the temporarily imposed macroscopic step stress Σ_0.

- The controlled forward strain $\Delta\gamma_{\mathrm{f}}$, the maximum strain accumulated during creep, which defines the stress switch-off time t_{stop}.
- The age or annealing of the material, given by the waiting time t_{w}.

Unless specified otherwise, the following parameter values will be applied across all the simulations in this chapter:

- The working temperature of the system, given by the noise temperature $x = 0.3$.
- Number of streamlines $S = 1$, meaning homogeneity in shear is enforced.
- Adaptive numerical timestep Δt_{ad}, with minimum $\Delta t = 0.01$.
- Solvent viscosity $\eta = 0$.
- Number of elements $M = 10^5$.

All of the parameters listed above are explained in more detail in Chapter 3.

This chapter will begin by outlining the general strain response of the system to the creep-recovery test protocol in Section 6.2, along with the mesoscopic element response in Section 6.3. Section 6.3 will also look more closely at some of the interesting behaviour of the strain relaxation after the stress switch-off, including (in some parameter regimes) a non-monotonic dependence on time. This is followed by an analysis of the recoverable strain $\Delta\gamma_{\mathrm{rec}}$ and its relationship with the imposed stress Σ_0 (Section 6.4), the controlled forward strain $\Delta\gamma_{\mathrm{f}}$ (Section 6.5) and the waiting time t_{w} (Section 6.6). Finally, Section 6.7 will provide some concluding remarks and suggest avenues of investigation to expand beyond this work. This research finds significant recoverable strain under the creep-recovery test protocol for the SGR model, and explores its origins, providing the foundations for modelling amorphous materials with high strain recoverability.

6.2 Strain Response

The stress application of the creep-recovery protocol is shown in the top panel of Fig. 6.1. After ageing the material for a waiting time t_{w}, a constant stress is applied at time $t = 0$ and then switched off at time t_{stop}. A typical strain response γ to this protocol is shown in the bottom panel of Fig. 6.1 for parameters $\Sigma_0 = 1.0$, $\Delta\gamma_{\mathrm{f}} = 0.5$, and $t_{\mathrm{w}} = 10^3$. There are four distinct regimes in the strain response:

- The instantaneous response to the application of the step stress at $t = 0$ is elastic, with the strain jump equal to the applied stress $\gamma(t = 0^+) = \gamma_0 = \Sigma_0/G_0$ and $G_0 = 1$ (see Section 2.2.1). This effect under a step stress is seen in experiments [9,19,28,51,112,157], though in these cases the modulus is generally not equal to one $G_0 \neq 1$. The $G_0 = 1$ displayed here is simply a consequence of the choice of units, which is discussed further in Section 3.2.

- The subsequent behaviour during the stress application is that of creep, where the strain slowly increases as the system strains forward under the applied stress, seen in a wide range of studies [25, 27, 28, 36, 51, 81, 87, 111, 112, 114]. As mentioned previously, for the approximation of homogeneous shear made in these simulations to be valid, the system must stay in primary creep during the stress application.

- At the switch-off of the stress at time $t = t_{\mathrm{stop}} = t(\gamma = \gamma_0 + \Delta\gamma_{\mathrm{f}})$, the instantaneous response is again elastic and the strain drops by the size of the imposed step stress/initial strain $\Sigma_0 = \gamma_0$. Note that this makes the value of the strain just after the removal of the stress equal to the controlled forward strain $\gamma(t^+_{\mathrm{stop}}) = \Delta\gamma_{\mathrm{f}}$.

- There is then some amount of strain relaxation before the system eventually reaches a steady state [123]. Generally, this post-stress straining results in a steady state strain below that of the strain immediately after the removal of the stress, with the system having recovered in the reverse direction some of the strain that arose in the forward direction during the stress application. This is the recoverable strain, which forms the key focus of this work.

The behaviour described here is also widely seen in experimental creep-recovery test studies [59, 77, 124, 152]. However, the instantaneous drop in strain is not always equal to the initial strain increase. In creep-recovery tests on concrete and fractal gels they are identical within experimental error [59, 124], but those on colloidal dispersions and protein gels found a significant disparity, with the instantaneous drop up to 50% smaller in size [77, 152], despite a quick removal of stress. In the SGR model, the element response to any instantaneous change in stress or strain will always be elastic, because no plastic yielding arises instantaneously (see Section 2.2.1). Therefore, as long as the timestep is small enough to ensure no elements are yielding in the timestep where the stress is switched off, all elements will behave elastically, with each local element stress dropping by the value of the stress that is being removed.

This equality between the instantaneous changes in strain could, however, be a feature of the enforced homogeneity in the model system used here. In these simulations all elements are governed by the same strain rate $\dot{\gamma}$, which becomes large and negative when the stress is removed, shifting all elements back by the same amount. Allowing strain rate heterogeneity across the system by introducing multiple streamlines could cause some streamlines to shift back further than others, as long as the average stress drop is equal to the overall stress drop Σ_0. In addition, if permanent breakage of elements was introduced into the model, as in the modification of the SGR model described in Section 2.4, the strain drop could be changed by broken elements. The effects of shear heterogeneity and broken elements are not studied here, but a discussion on their possible effects can be found in Section 6.7. Regardless, the general finding of significant recoverable strain within the SGR model is expected to remain a feature of these systems.

Also outlined in the bottom panel of Fig. 6.1 is the definition of the recoverable strain $\Delta\gamma_{\mathrm{rec}}$, which follows that adopted in other studies [50, 77, 123]. $\Delta\gamma_{\mathrm{rec}}$ is equal

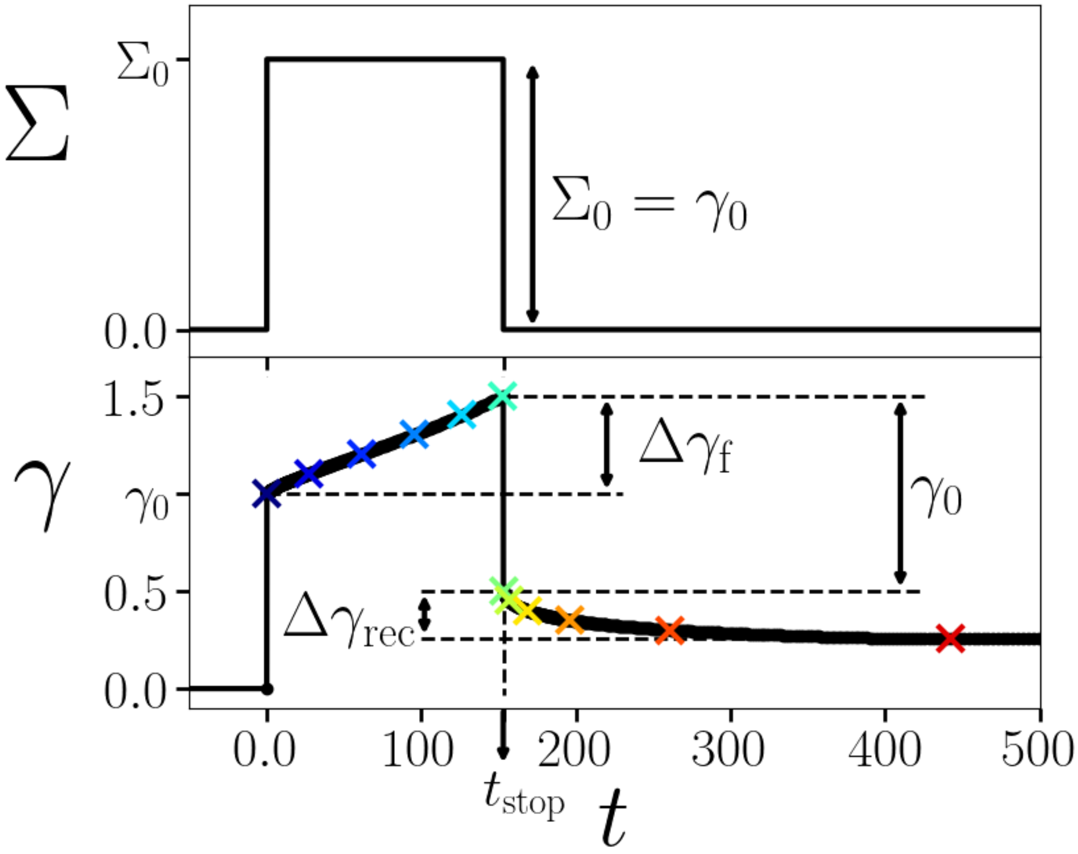

Figure 6.1: **Top Panel**: The stress Σ applied as a function of time for the creep-recovery test protocol. This features the preparation of the sample at $t = -t_w$, which then ages undisturbed for a time $-t_w < t < 0$. At $t = 0$, a step stress is applied and then subsequently removed at a time $t_{stop} = t(\gamma = \gamma_0 + \Delta\gamma_f)$. Note that the initial strain response is equal to that of the imposed step stress $\gamma_0 = \Sigma_0$.
Bottom panel: The strain γ response over time t as simulated by the SGR model with homogeneity enforced, where $\Sigma_0 = 1.0$, $\Delta\gamma_f = 0.5$, and $t_w = 10^3$. Highlighted are the controlled forward strain $\Delta\gamma_f$, the immediate strain drop after the stress is removed equal to the initial imposed step stress $\gamma_0 = \Sigma_0$, and the degree of recoverable strain $\Delta\gamma_{rec}$ measured from t^+_{stop}. The coloured crosses highlight the instances in time at which the normalised distribution of element strains $P(l)$ are plotted in Fig. 6.2.

to the difference between the strain immediately after the stress removal, equal to the controlled forward strain $\gamma(t^+_{\text{stop}}) = \gamma_0 + \Delta\gamma_{\text{f}} - \gamma_0 = \Delta\gamma_{\text{f}}$, and the steady state strain $\gamma_{\text{ss}} = \gamma(t \to \infty)$. This value is positive when γ_{ss} is smaller than $\Delta\gamma_{\text{f}}$. In mathematical terms

$$\Delta\gamma_{\text{rec}} = \Delta\gamma_{\text{f}} - \gamma_{\text{ss}} \,. \tag{6.2.1}$$

6.3 Element Distribution Analysis

6.3.1 General Element Response

Fig. 6.2 displays the response of the distribution of element strains $P(l)$ to the creep-recovery test protocol for the simulation featured in the bottom panel of Fig. 6.1. The coloured crosses in the bottom panel of Fig. 6.1 correspond to the instances in the simulation where $P(l)$ has been plotted in Fig. 6.2.

The top panel of Fig. 6.2 shows the behaviour before the stress is switched off, for times $t < t_{\text{stop}}$, and the bottom panel for times after switch-off $t > t_{\text{stop}}$. Recall that the SGR model features a number of elements M, each with a strain l and energy well E, which in this case all exist on a single streamline due to the enforced shear homogeneity (see Section 2.2). The distribution of element strains $P(l)$ plots the histogram of element strain frequencies.

The initial distribution of element strains $P_0(l)$ at time $t = 0$ is a delta function at the value of the imposed step stress $l = \Sigma_0$, represented by the dark blue line in top panel of Fig. 6.2. Note that this is artificially represented in this figure as a peak with finite height and width, because a true delta function is impossible to plot. All the element strains are equal to the imposed step stress $l_m = \Sigma_0 \; \forall \; m$. As explained previously, the instantaneous application of stress has caused an elastic element response. Note that in a real experimental study, there could be a range of strains within the material before shear, whereas here it is assumed that for a newly

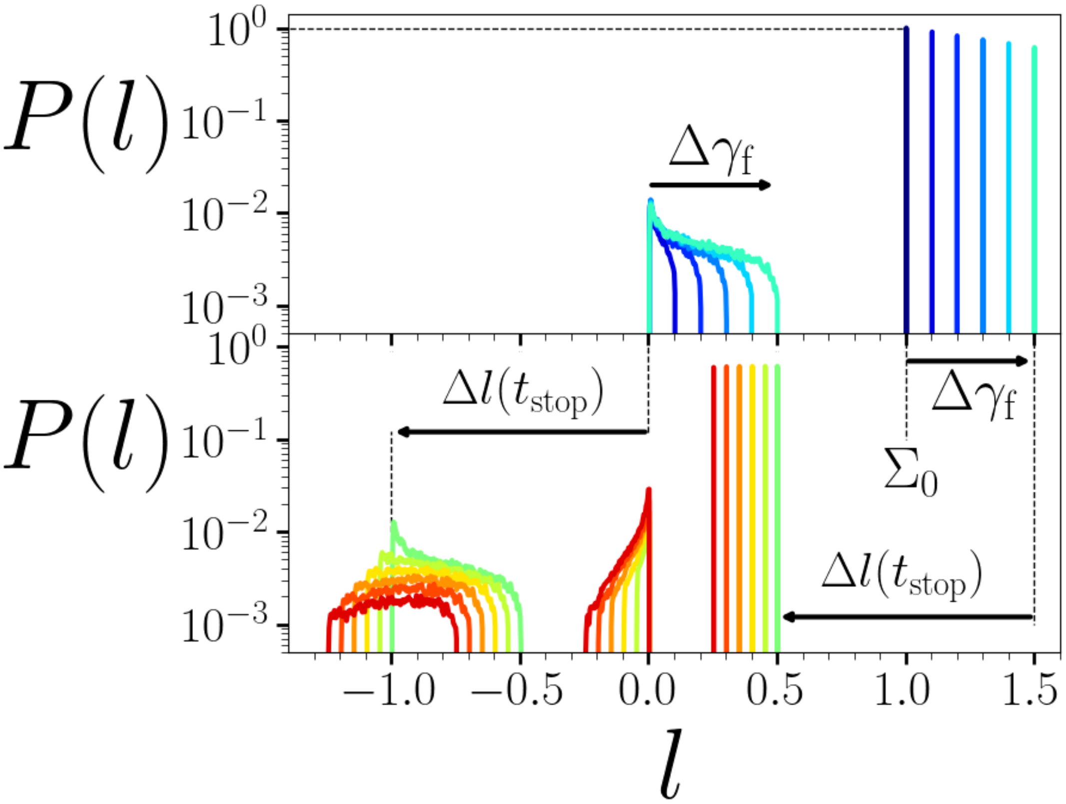

Figure 6.2: **Top Panel**: The normalised distribution of element strains $P(l)$ at several times during the simulation in Fig. 6.1, for which $\Sigma_0 = 1.0$, $\Delta\gamma_\mathrm{f} = 0.5$, and $t_\mathrm{w} = 10^3$. The different colours (from dark blue to turquoise or left to right in the peaks in the right panel) represent different instances in time before the stress has been switched off ($t < t_\mathrm{stop}$), highlighted by crosses in the bottom panel of Fig. 6.1.

Bottom Panel: The measurement described above, but for times after the stress has been switched off ($t > t_\mathrm{stop}$). The different colours (from green to red or right to left in the peaks in the middle panel) represent different instances in time, highlighted by crosses in the bottom panel of Fig. 6.1.

Highlighted is the instantaneous strain shift in the entire system by $\Delta l(t_\mathrm{stop}) = -\Sigma_0$ at time $t = t_\mathrm{stop}$, caused by the switch-off of the stress. This shift occurs between the turquoise plot in the top panel and the green plot in the bottom panel. Also note that the narrow peaks on the right-hand side of both panels are representative of single-value functions, as all elements in practice have the same strain value in these peaks.

Key result: Recoverable strain depends on the yielding of elements with positive and negative strains.

prepared, undeformed sample, all element strains are zero $l = 0$, following previous studies [9, 71, 81].

After some time (the dark blue to light blue lines), some of the elements in the delta function begin to yield. This can be seen in the decreasing area within the thin peak. As discussed in Section 2.2.1, when an element yields, it relaxes its strain l and its contribution to the visco-elastic stress σ, equal to the average of the element strains, becomes zero. Considering Eq. (2.2.5) and the imposition of a constant stress $\Sigma = \Sigma_0$, this decrease in σ will cause an increase in the strain rate $\dot{\gamma}$. Hence, the system starts straining forward, seen in the rightward shift of the thin peaks in the top panel of Fig. 6.2 for increasing times. In other words, for the total stress to remain constant, when an element relaxes its strain through a yield event, the other elements must compensate by straining forward.

The consequence of yielding elements on the macroscopic strain rate $\dot{\gamma}$ is an important part of the recoverable strain process and will be discussed in detail in this chapter. To summarise, when a positively strained ($l_m > 0$) element yields, it provides a positive contribution to the macroscopic strain rate $\dot{\gamma}$.

When elements yield, their strain drops to zero $l_m \to 0$. This explains the second part of the strain distribution in the middle of the top panel of Fig. 6.2, which sees an increasing group of elements around zero strain $l = 0$. However, after yielding, this group also strains forward due to the macroscopic forward strain rate caused by the yielding elements. The smearing of the element strains in this group is a consequence of elements yielding at different times, and therefore straining forward by different amounts.

Once the system has strained forward by a value equal to the controlled forward strain $\Delta\gamma_{\mathrm{f}}$, the stress is switched off. There are therefore two groups of elements that can be seen in the top panel of Fig. 6.2 at the switch-off time:

(i) A delta function of elements that have not yet yielded, all with strain $l = \Sigma_0 + \Delta\gamma_{\mathrm{f}}$, represented by the turquoise line in the right of the top panel of Fig.

6.2.

(ii) A spread of elements that have yielded during the imposed step stress, with smallest strain $l = 0$ and largest strain $l = \Delta\gamma_{\mathrm{f}}$, represented by the turquoise line in the middle of the top panel of Fig. 6.2.

When the stress is switched off, the macroscopic strain rate is instantaneously large and negative, straining the whole system backwards by the amplitude of the removed stress $\Delta l(t_{\mathrm{stop}}) = -\Sigma_0$. As mentioned previously, the elements respond elastically to this change and all strain backwards by this same amount $l \to l - \Sigma_0$. This causes the two aforementioned groups of elements to assume new strains:

(i) The delta function of elements that have not yet yielded now all have strain $l = \Sigma_0 + \Delta\gamma_{\mathrm{f}} - \Sigma_0 = \Delta\gamma_{\mathrm{f}}$, represented by the green line in the right of the bottom panel of Fig. 6.2.

(ii) The spread of elements that had yielded during the imposed step stress have also been strained backwards by Σ_0. This gives a distribution of strain values with minimum value $l = 0 - \Sigma_0 = -\Sigma_0$ and maximum $l = \Delta\gamma_{\mathrm{f}} - \Sigma_0$, represented by the green line in the left of the bottom panel of Fig. 6.2.

Once the stress is removed, with no external factors, these two groups (i) and (ii) determine how the system relaxes. To exhibit recoverable strain, the system needs to strain backwards. This is achieved in an analogous way to that in which the forward straining was achieved during the application of the step stress. Elements in group (ii) will yield to zero strain $l_m \to 0$. However, they are now yielding from a *negative* strain $l_m < 0$. This means the visco-elastic stress σ (equal to the average of the element strains) will increase, causing the strain rate $\dot{\gamma}$ to decrease. If enough yielding occurs from negatively strained elements, then the strain rate will decrease enough to become negative, and the system will strain backwards.

This process is important, because it is the origin of recoverable strain in the SGR model. To summarise, when a negatively strained ($l_m < 0$) element yields, it provides a negative contribution to the macroscopic strain rate $\dot{\gamma}$.

This yielding of negatively strained elements can be seen in the bottom panel of Fig. 6.2, where the distribution on the left, representing group (ii), decreases in height over time (from green to red lines) causing the system to strain backwards. These yielding elements then form a third group, with strains around zero. The elements in this group then also strain backwards due to the negative macroscopic strain rate just discussed.

This behaviour is interesting, because element yield events correspond to plastic rearrangements, yet it is these elements that form group (ii) that cause the backwards straining that leads to recoverable strain. Therefore, it can be concluded from this study that, in the SGR model, any strain recovery that occurs after the initial elastic response at $t = t_{\text{stop}}$ is a direct consequence of plastic events. This is in contrast to the interpretation in some of the literature, which assumes the recoverability of a material to be a consequence of elastic straining [45, 125, 152, 190, 214]. The effect instead resembles the phenomenon of reversible plasticity [58, 135–139, 145–151], which has not before been seen in the SGR model or predicted theoretically in the creep-recovery protocol.

Some studies define reversible plasticity as rearrangements that return to their exact pre-yield configuration in space [147–149]. This definition requires microscopic accuracy of individual particle trajectories [147, 149], which is not possible with this model. The reversible plasticity observed here is more closely aligned with that defined in the polymer literature, where plastically breaking bonds can reform, but the resulting configuration is not identical to that pre-yield [136, 137, 139]. This definition generally focusses on the reversibility of plastic strain rather than particle behaviour, similar to that seen in metallic glasses [150], which is more relevant in applications in reversible plasticity shape memory polymers [136, 137] and in hydrogels [146].

Reversible plasticity has also been connected to the Bauschinger effect in the crystalline solid literature [145]. This is where the material response to external forces changes as a result of the microscopic stress distribution of the material [230–232]. The effect is highly directional, for example, a forward stress causes rearrangements that then resist further forward loading but are less resistant to reversing the direction of the applied load [230, 231].

While the Bauschinger effect is generally attributed to solid materials, it is relevant to the example shown in Fig. 6.2. The elements in group (ii) that have experienced a plastic rearrangement event have reformed and continued straining forward under the step stress, relieving the other elements of some of the overall load, effectively resisting further forward loading. However, when the stress is switched off, the system shifts back suddenly, and the elements are in configurations which are negatively strained. These elements, whose subsequent yielding leads to the reversible plasticity observed, have a high rate of yielding. This reversal of shear direction causes a large amount of yielding showing a low resistance of these elements to a change in strain direction, reminiscent of the Bauschinger effect.

This mechanical polarisation in shear strength through reversible plasticity has been seen under cyclic shear in a TEP model similar to that discussed in Section 2.3, but was not recognised as Bauschinger-like behaviour [148]. The work here therefore provides a new perspective on the origin of recoverable strain, where plastic rearrangement events that relax strain locally in a system can contribute to the recoverability of the system through reversible plasticity caused by a Bauschinger-like effect.

It should be noted that in Fig. 6.2 the area within the delta function of elements representing group (i), is decreasing, though by an amount not visible on the scale shown. Therefore, there are elements in group (i) that are yielding in addition to those in group (ii). This is despite the system straining backwards, decreasing the probability of yielding for these elements. These elements have a positive strain, and so will provide a positive contribution to the strain rate. In the case of the example in Fig. 6.2, the yielding from group (ii) dominates over the yielding from group (i) and so the system strains backwards. However, in other cases that will be seen in this chapter, this positively strained group (i) of elements can limit the amount of backwards straining, and sometimes cause further forward straining after the stress switch-off.

What is important from this discussion of the time evaluation of the distribution of local strains is that the behaviour after the removal of stress is the consequence of a competition between the two groups of elements already discussed:

- Group (i): The positively strained elements, with a delta function distribution of strains, which have not yet yielded. When these elements yield they contribute a forward strain.
- Group (ii): The negatively strained elements, with a smeared distribution of strains, which had yielded during the imposed step stress. When these elements yield they contribute a backwards (or reverse) strain, contributing to strain recovery.

It is also important to acknowledge how the various input parameters affect these competing groups, because this will aid in understanding the relaxation behaviours that will be discussed in the rest of this chapter:

- The imposed step stress Σ_0. This determines the minimum strain of group (ii). The effects of Σ_0 will be explored further in Section 6.4.
- The controlled forward strain $\Delta\gamma_{\mathrm{f}}$. This determines the strain of the elements in group (i), the maximum strain of the elements in group (ii), and the relative numbers of elements in the two groups. A larger $\Delta\gamma_{\mathrm{f}}$ will result in a larger group (ii) and a smaller group (i), and vice versa for a smaller $\Delta\gamma_{\mathrm{f}}$. The effects of $\Delta\gamma_{\mathrm{f}}$ will be explored further in Section 6.5.
- The waiting time t_{w}. This determines the depths of the energy wells occupied by elements in group (i). The effects of t_{w} will be explored further in Section 6.6.

Note that both the imposed stress Σ_0 and the waiting time t_w will also determine the rate at which the system reaches the controlled forward strain, $\Delta\gamma_\mathrm{f}$, which could change the shape of the group (ii) strain distribution. However, this effect is not studied here. In addition, there will be results presented for the case in which $\Delta\gamma_\mathrm{f}$ is larger than Σ_0, which will mean a fraction of the elements in group (ii) will actually have positive strains after the stress switch-off. However, there will always be some proportion of elements in group (ii) with negative strains, so the recoverable strain mechanism still works in the same way as described above. For this reason, when analysing the way in which the behaviour of elements governs strain recovery in Sections 6.3.2 to 6.3.4, there will be a simple distinction between elements with positive strain, and those with negative strain.

To analyse the behaviour described above, this study will consider a slight variation on the yielding integral I described in Section 3.3.4, where the contributions to I from positively and negatively strained elements are now considered separately. Therefore, the yielding integral of positively strained elements is defined as

$$I^+ = \int_0^\infty r(l)P(l)l\,dl\,, \tag{6.3.1}$$

and the yielding integral of negatively strained elements as

$$I^- = \int_{-\infty}^0 r(l)P(l)l\,dl\,. \tag{6.3.2}$$

The total yielding integral I effectively measures the average rate of strain relaxation across the system from yielding by taking the average value integral over the strain space l of the multiplication of the strain distribution $P(l)$ and the yielding rate $r(l)$. What splitting this integral into its positive I^+ and negative I^- parts does is inform the average strain relaxation rate for elements with positive and negative strains separately. These variables effectively measure the competition in yielding between the positively strained group (i) with I^+ and the negatively strained group (ii) with I^-. Note that once elements in these two groups have yielded for times after the stress switch-off, they provide only a small contribution to I because their strains are small and their energy wells are generally shallow. Therefore, the contributions of elements that have yielded after the stress switch-off to I^+ and I^- are negligible in comparison to the contribution of elements in groups (i) and (ii), and so the corresponding pairs ($I^+ \sim$ (i) and $I^- \sim$ (ii)) will be discussed interchangeably.

In addition, the proportion of elements with positive or negative strains can be measured using

$$\rho^+ = \int_0^\infty P(l)\, dl \,, \tag{6.3.3}$$

and

$$\rho^- = \int_{-\infty}^0 P(l)\, dl \,. \tag{6.3.4}$$

This normalised proportion of elements simply reflects the number of elements with positive or negative strains relative to the total number of elements.

The next three sections will present the results of three representative numerical simulations that summarise the responses of the SGR model to the creep-recovery test protocol. For each of these simulations, the underlying behaviour in terms of the dynamics of the mesoscopic elements will be explored using the above variables.

6.3.2 Significant Recoverable Strain

A representative simulation is chosen to outline how the element behaviour described in the previous section contributes to significant strain recovery after the stress is switched off. The results are presented in Fig. 6.3. The top panel shows the strain decay γ as a function of time. Note that the strain is normalised by the controlled forward strain $\Delta\gamma_{\mathrm{f}}$. The time is plotted relative to the stress switch-off time t_{stop} to remove the time during the stress application $0 < t < t_{\mathrm{stop}}$ and focus only on the strain relaxation for times $t > t_{\mathrm{stop}}^+$.

The observed behaviour closely reflects that described in Section 6.2 and Section 6.3.1. At short times there is a negative strain rate in the system which eventually tends to zero as the system reaches a steady state. Important to note is the observation

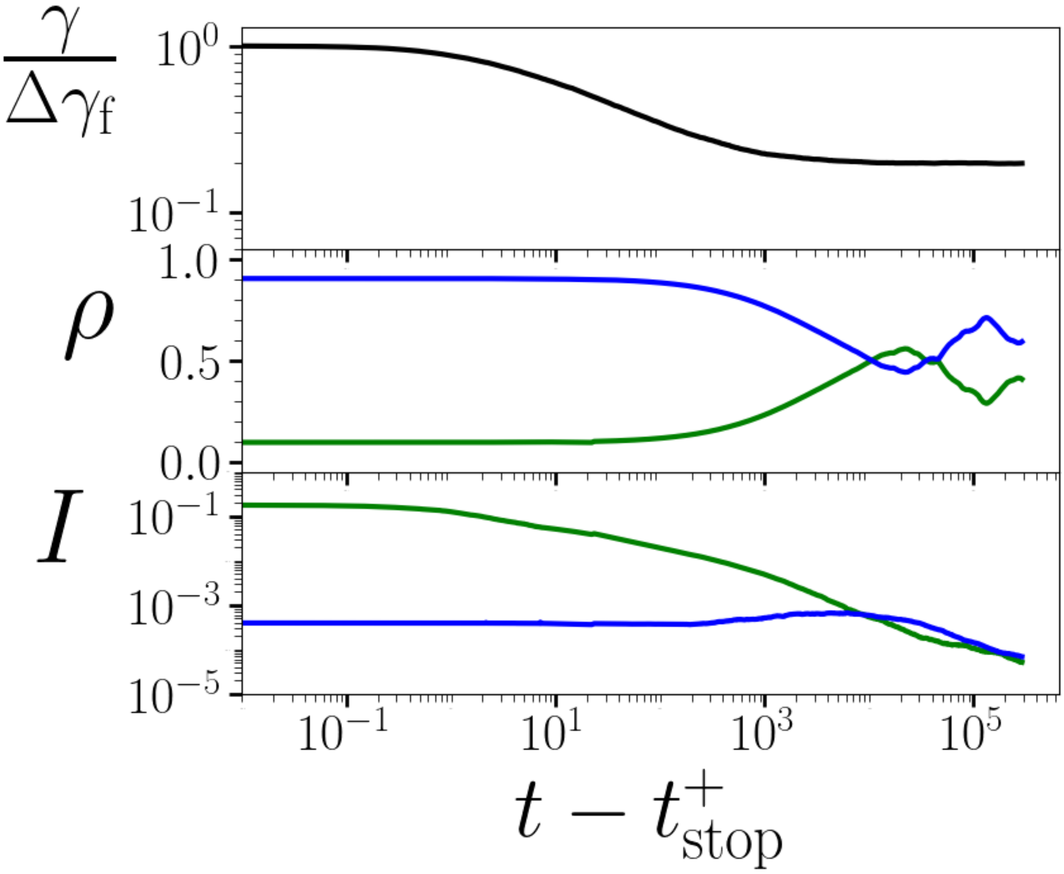

Figure 6.3: **Top panel**: The strain response γ normalised by the controlled forward strain $\Delta\gamma_{\mathrm{f}}$ as a function of time after the stress switch-off for an imposed step stress $\Sigma_0 = 1.0$, controlled forward strain $\Delta\gamma_{\mathrm{f}} = 0.1$, and waiting time $t_{\mathrm{w}} = 10^3$.
Middle panel: For the above simulation, the proportion of elements with positive (blue, top line at $t - t^+_{\mathrm{stop}} = 10^{-1}$) and negative (green, bottom line at $t - t^+_{\mathrm{stop}} = 10^{-1}$) strains.
Bottom panel: For the above simulation, the yielding integral over positive I^+ (blue, bottom line at $t - t^+_{\mathrm{stop}} = 10^{-1}$) and negative I^- (green, top line at $t - t^+_{\mathrm{stop}} = 10^{-1}$) strains.
Key result: Simulations display significant recoverable strain, dependent on the yielding of elements with positive and negative strains.

of significant recoverable strain. Indeed, in this simulation, the system recovers 80% of the strain from its value at time $t = t^{+}_{\text{stop}}$ just after the stress has been removed. This displays the capacity of the SGR model to simulate materials that exhibit a high degree of recoverable strain.

Observing the two contributions I^{+} and I^{-} to the yielding integral I in the bottom panel of Fig. 6.3 makes clear how this recoverable strain is achieved. The yielding integral for negative strains I^{-} (green line, bottom panel) is initially large, meaning there are a lot of negatively strained elements in group (ii) that are yielding, causing a negative strain rate. Over time, I^{-} drops as the number of elements in group (ii) with significant negative strains decreases due to yielding. As the yielding integral for negative strains I^{-} drops towards a value similar to the yielding integral for positive strains I^{+} (blue line, bottom panel), the strain γ (top panel) decrease starts to slow, eventually reaching a steady state.

The tending to a steady state is due to the yielding of the elements in group (i), the positively strained delta function, whose yielding is represented by I^{+}. I^{+} is a flat function at early times, implying a small but steady amount of yielding of positively strained elements. However, the effect of this yielding is initially nullified by the large amount of yielding of negatively strained elements in group (ii), shown by the large disparity between I^{+} and I^{-} at early times. The strain rate starts tending towards zero when I^{+} and I^{-} are closer in value, showing that the yielding of elements in group (i), represented by I^{+}, becomes significant. When I^{-} drops below I^{+}, the yielding of positively strained elements is now dominating. This dominance is short-lived however, and both yielding integrals then tend towards zero causing the strain to reach a steady state value.

The behaviour described above is not immediately obvious from the proportion of positively (ρ^{+}) and negatively (ρ^{-}) strained elements in the middle panel of Fig. 6.3, because the fraction of positively strained elements is initially much larger than those with negative strain. However, it is important to remember that the positive strain of the elements in group (i) is defined by the controlled forward strain

$\Delta\gamma_{\mathrm{f}} = 0.1$, whereas the maximum negative strain of elements in group (ii) is given by the imposed step stress $\Sigma_0 = 1.0$. Therefore, although in this instance group (i) has a large number of elements, their strain is small ($l = 0.1$) compared to the large negative strain of the small number of negatively strained elements in group (ii) ($-1.0 < l < -0.9$). In addition, the influence of the waiting time $t_{\mathrm{w}} = 10^3$ means that the elements in group (i) are also in deeper energy wells on average than those in group (ii). Taken together, this means that when the yielding integral is calculated for the positively strained elements in group (i), the low rate of yielding causes I^+ to be small, despite the large number of elements.

There is also some noise in ρ in the middle panel of Fig. 6.3 towards the end of the simulation. This is because, by this time, the majority of the finite number of elements have yielded, clear from the small yielding integral I for both positively and negatively strained elements. Therefore, all elements have a strain around or equal to zero $l \sim 0$, meaning even a small shift in the system can cause elements to go from positive to negative strain. The values for the proportions ρ must be considered with the perspective provided by the yielding integral I. Repeating the simulations for a larger number of elements M would reduce this noise but this was not possible within the timescales for this project.

Behaviour of the kind described above can demonstrate significant recoverable strain, and is the most common type of behaviour seen across the parameter regimes explored in this work.

6.3.3 Recoverable Strain with a Non-Monotonic Strain Response

Fig. 6.4 shows another representative example of the recovery behaviour predicted by the SGR model. The strain decay γ in the top panel of Fig. 6.4 is very similar to that in Fig. 6.3, with one important difference. The strain decay in Fig. 6.3 is monotonic as a function of time, whereas the strain in Fig. 6.4 appears to reach

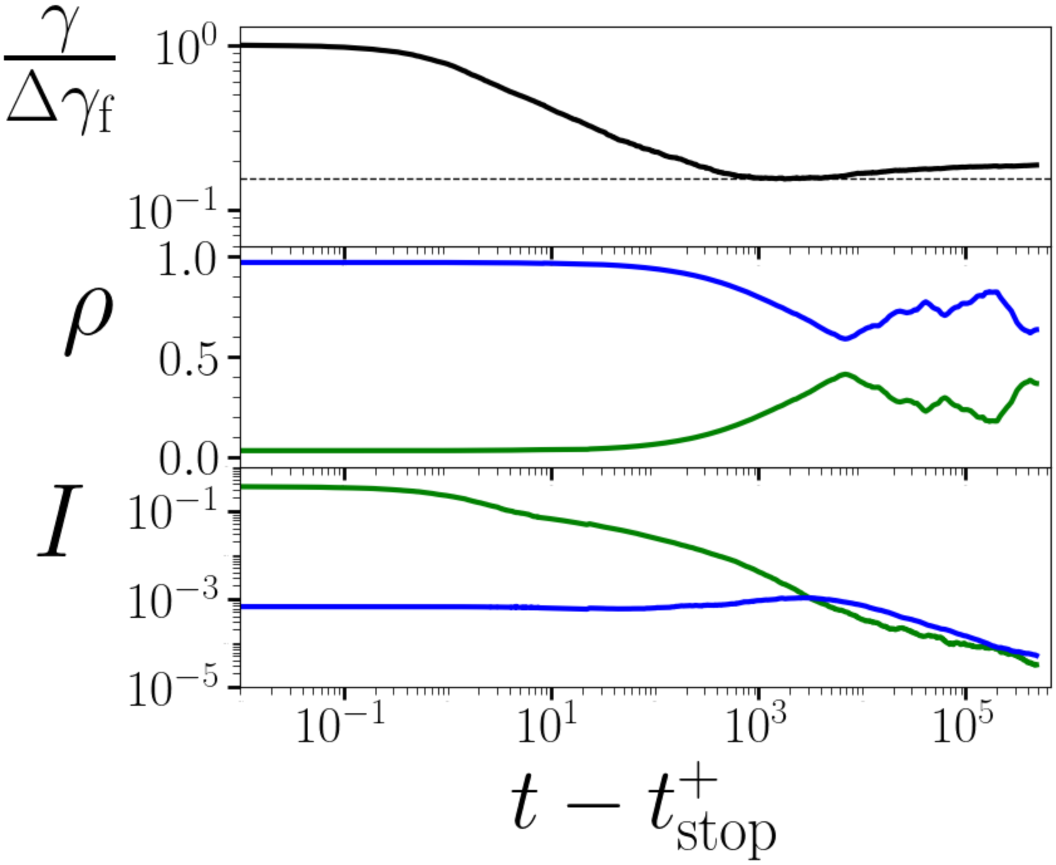

Figure 6.4: **Top panel**: The strain response γ normalised by the controlled forward strain $\Delta\gamma_f$ as a function of time after the stress switch-off for an imposed step stress $\Sigma_0 = 1.0$, controlled forward strain $\Delta\gamma_f = 0.03$, and waiting time $t_w = 10^3$. The dashed line highlights the minimum value that the strain achieves.
Middle panel: For the above simulation, the proportion of elements with positive (blue, top line at $t - t^+_{\text{stop}} = 10^{-1}$) and negative (green, bottom line at $t - t^+_{\text{stop}} = 10^{-1}$) strains.
Bottom panel: For the above simulation, the yielding integral over positive (blue, bottom line at $t - t^+_{\text{stop}} = 10^{-1}$) and negative (green, top line at $t - t^+_{\text{stop}} = 10^{-1}$) strains.
Key result: Simulations can display non-monotonic strain responses.

a minimum before rising and then subsequently settling to a steady state. This non-monotonic strain recovery is surprising considering the simple nature of the model. It shows that the SGR model has the capacity to simulate complex memory effects in recoverable amorphous materials.

The non-monotonic behaviour can be understood as follows. The behaviour of the strain at early times in Fig. 6.4 is similar to that discussed in Section 6.3.2. The yielding of negatively strained elements in group (ii) dominates the small rate of yielding of positively strained elements in group (i), as seen in the orders of magnitude difference in the sizes of I^+ and I^-. However, the point at which I^+ and I^- cross over is earlier in time than for the example in Fig. 6.3 and I^+ is significantly larger than I^- for a longer period of time. This means that the yielding of elements in group (i) dominates enough during this time not just to bring the negative strain rate back to zero, but actually enough to cause the strain rate to become positive. The system then attains a steady state as both I^+ and I^- drop towards zero. In this simulation, the competition between group (i) and group (ii) described in Section 6.3.1 has resulted in a non-monotonic strain response.

The behaviour of the proportions ρ^+ and ρ^- are very similar to that in Fig. 6.3, except that when the system starts straining forward, ρ^+ increases, leaving a larger steady state separation between ρ^+ and ρ^-.

The discovery of non-monotonicity in the strain response as a function of time is an exciting result. Complex material memory and non-monotonic rheological responses are areas of significant current interest in the rheology literature [28, 44, 56, 57, 158, 173, 237–240]. The non-monotonic relaxation behaviour of strain with time here is reminiscent of experiments on colloidal gels showing non-monotonic stress decay after the removal of a constant strain rate [57]. However, as will be shown in Sections 6.4 to 6.6, this particular non-monotonicity in strain recovery is only visible for a small range of parameter space, discovered as a consequence of a fine preliminary sampling of the parameter space. For the majority of the parameters explored, the behaviour generally follows that described in Section 6.3.2, where I^- dominates such that the only influence of I^+ is to reach a steady state, and the strain recovers monotonically. Regardless, the discovery of non-monotonicity in strain recovery in the SGR model, even when restricted to enforced shear homogeneity, shows the potential for simulating complex recoverable strain behaviour.

6.3.4 Negative Recoverable Strain

The third representative example of the predictions of the SGR model under the creep-recovery test protocol is shown in Fig. 6.5. This shows two simulations, with identical imposed step stress $\Sigma_0 = 2.0$ and controlled forward strain $\Delta\gamma_\mathrm{f} = 3.0$, but different waiting times $t_\mathrm{w} = 10^3$ (solid lines) and $t_\mathrm{w} = 10^6$ (dashed lines).

Considering first the $t_\mathrm{w} = 10^6$ (dashed line) simulation, the observed behaviour is recognisable as an extreme version of that described in Section 6.3.2. The initial state sees a dominance of I^- over I^+ and therefore a negative strain rate produced by the yielding of group (ii) dominating over that of group (i). This is then followed by an approach to steady state when I^+ and I^- reach similar values. This can also be seen in the response of ρ^+ and ρ^-, as the system strains backwards the proportion of negatively strained elements ρ^- increases.

The $t_\mathrm{w} = 10^3$ (solid line) simulation, on the other hand, displays a new phenomenon. In this case, the strain first increases, before reaching a maximum, and then subsequently decreases to a steady strain that remains above the starting strain $\gamma_\mathrm{ss} > \Delta\gamma_\mathrm{f}$.

The behaviour of the two populations of elements in this simulation is much more complex than those previously characterised, but can still be summarised by the competition of yielding between positively and negatively strained elements. The initial system state sees I^+ and I^- almost equal (bottom panel of Fig. 6.5, solid lines), but with I^+ marginally larger. This means that the yielding of positively strained elements in group (i) dominates over that of the negatively strained elements in group (ii). This results in a positive strain rate. However, at a time around $t \sim 10^1$,

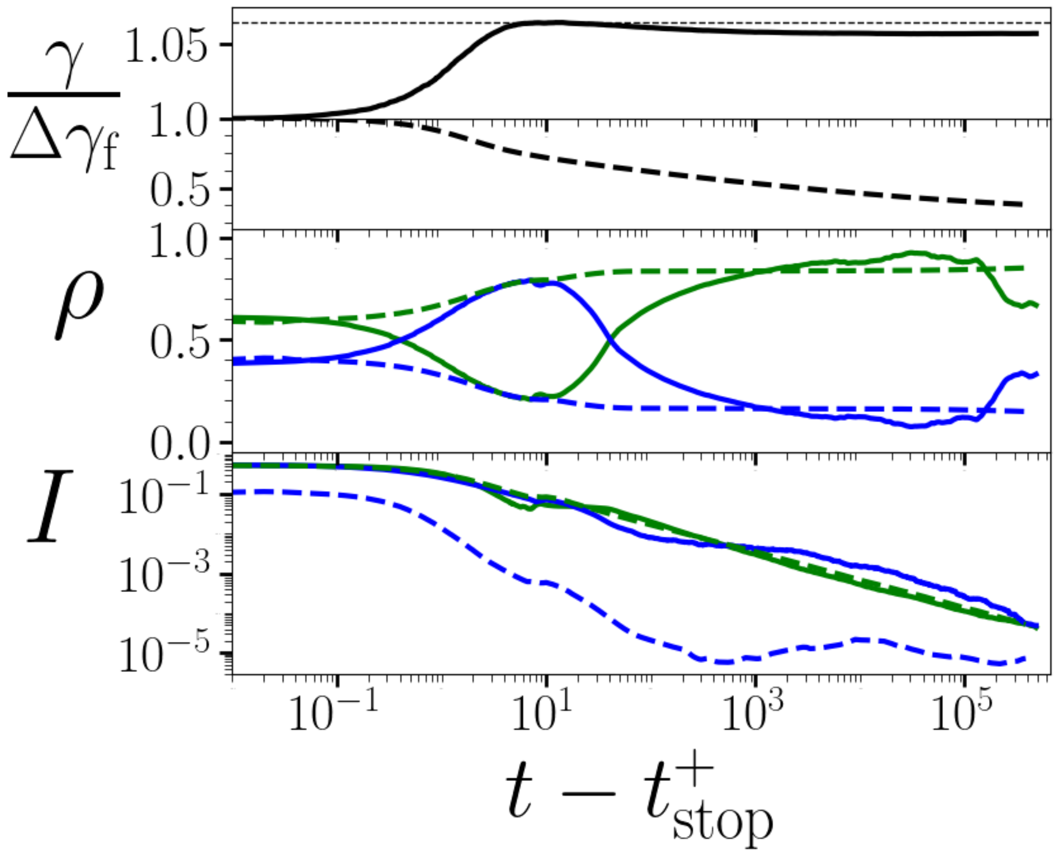

Figure 6.5: **Top panel**: The strain response γ normalised by the controlled forward strain $\Delta\gamma_f$ as a function of time after the stress switch-off for an imposed step stress $\Sigma_0 = 2.0$, controlled forward strain $\Delta\gamma_f = 3.0$, and for two waiting times $t_w = 10^3$ (solid lines) and $t_w = 10^6$ (dashed lines). Note the separation of axes with different scales to highlight the two simulation responses. The thin dashed line highlights the maximum value that the strain achieves.
Middle panel: For the above simulations, the proportion of elements with positive (blue, bottom group at $t - t^+_{\text{stop}} = 10^{-1}$) and negative (green, top group at $t - t^+_{\text{stop}} = 10^{-1}$) strains.
Bottom panel: For the above simulations, the yielding integral over positive (blue, bottom dashed line at $t - t^+_{\text{stop}} = 10^{-1}$) and negative (green, top dashed line at $t - t^+_{\text{stop}} = 10^{-1}$) strains.
Key result: Simulations can display negative recoverable strain.

I^- begins to dominate, causing the strain rate to decrease (with the strain attaining a maximum) and eventually become negative. At a time around $t \sim 10^3$, I^+ dominates, which brings the negative strain rate back up towards zero after which it settles to a steady state. The response of ρ^+ and ρ^- mirrors the behaviour of the strain, with the proportion of positively strained elements ρ^+ increasing to reach a maximum before decreasing to reach a steady state.

This is another example of non-monotonic strain behaviour in creep recovery. Experiments on colloidal gels found that the steady state residual stress after shear startup could be higher than the stress immediately after the switch-off of the strain rate, providing a counterpart to the scenario found here [57]. This again shows the capability of the SGR model to predict complex behaviour during creep recovery.

It is important to note that the behaviour just described leads to a negative recoverable strain $\Delta\gamma_{\mathrm{rec}} = \Delta\gamma_{\mathrm{f}} - \gamma_{\mathrm{ss}} < 0$, implying that the system has not only failed to recover any of the strain gained during the stress application, but has managed to gain additional strain after the removal of stress. Note that the elastic contributions to the strain are ignored here, because the strain gained instantaneously upon the stress application and recovered upon its removal is equal. As will be discussed when looking more broadly across the parameter space, this particular behaviour only occurs when the imposed step stress Σ_0 and controlled forward strain $\Delta\gamma_{\mathrm{f}}$ are both large. This therefore can be argued that the system has been strained so severely during the imposition of the step stress that even when the stress is switched off the system continues to feel its effects.

What is also interesting to note in Fig. 6.5 is the impact of the waiting time t_{w}. In Section 6.3.1, it was argued that the only significant impact of t_{w} was on the average energy depth of the positively strained elements in group (i). This impact can be seen in the bottom panel of Fig. 6.5, where there is a significant difference in the starting values of I^+ for the two different waiting times (blue dashed and solid lines), representing the yielding integral for these elements. The larger t_{w} causes the elements in group (i) to be in deeper traps. This in turn causes their rate of yielding

$r(l)$, and consequently the yielding integral I^+, to be smaller. However, there is almost no difference in the behaviour of I^- between the two different waiting times (green dashed and solid lines), representing the yielding integral for the negatively strained elements in group (ii). This shows that t_w can have a significant impact, but only on the group (i) of positively strained elements.

6.3.5 Summary

The above discussions have explored how the strain recovery predicted by the SGR model stems from the dynamics of its mesoscopic elements. This behaviour can be highly complex, but is summarised by the competition between the yielding of the positively strained elements in group (i), which contribute a forward strain, and the negatively strained elements in group (ii) which contribute a reverse strain.

The three representative simulations just described provide a general overview of the three types of responses seen across all the simulations explored in this work. The following sections will consider the dependence of strain recovery on the input parameters, referencing back to the discussions of the preceding sections where appropriate.

6.4 Dependence of recoverable strain on Σ_0

The strain decay γ as a function of time for several different amplitudes of the temporarily imposed stress Σ_0 is shown in Fig. 6.6. Note that the strain plotted is normalised by the controlled forward strain $\Delta\gamma_\mathrm{f}$ (although in this case the value is constant $\Delta\gamma_\mathrm{f} = 0.5$ for these results). The time is plotted relative to the time t_stop at which the stress is switched off to remove the time during the stress application $0 < t < t_\mathrm{stop}$ and focus only on the strain relaxation.

The behaviour observed in these simulations reflects that described in Section 6.2, Section 6.3.1 and Section 6.3.2. In particular, there is a negative strain rate due

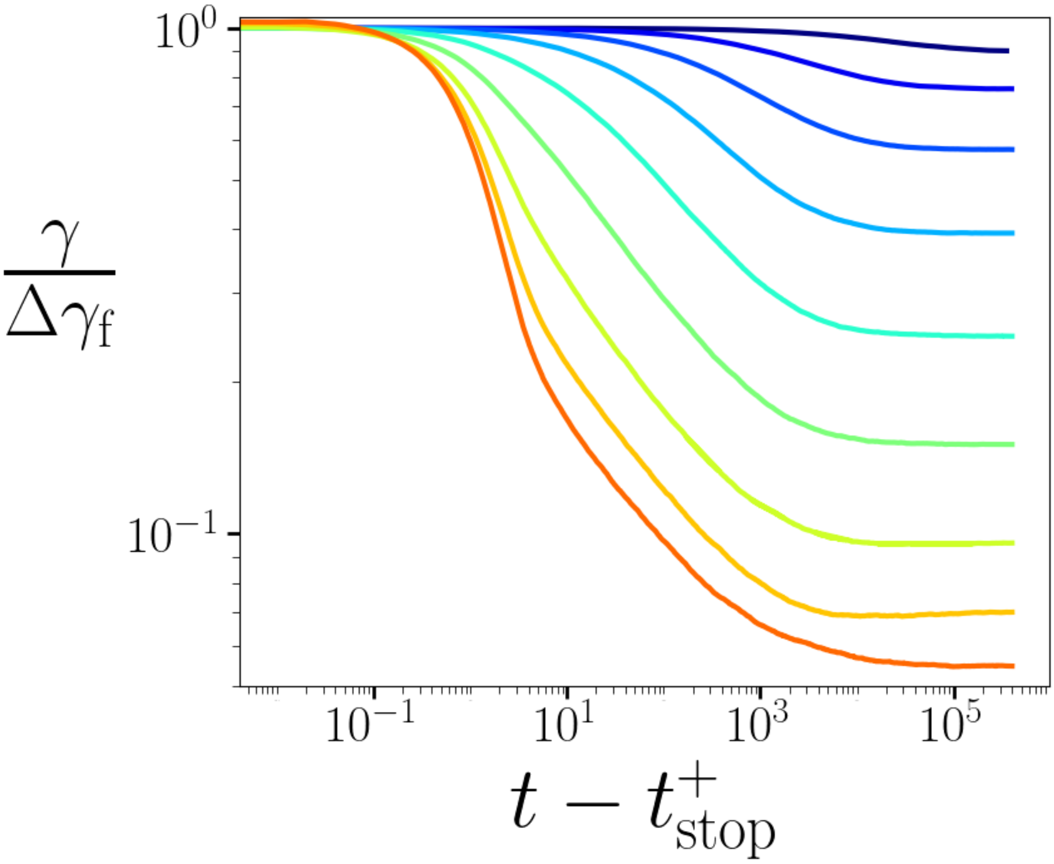

Figure 6.6: The strain response γ normalised by the controlled forward strain $\Delta\gamma_{\mathrm{f}}$ as a function of time after the stress switch-off for a single controlled forward strain $\Delta\gamma_{\mathrm{f}} = 0.5$, waiting time $t_{\mathrm{w}} = 10^3$ and a range of imposed step stresses $\Sigma_0 = [0.3, 0.5, ..., 1.9]$ (from top to bottom or dark blue to red).
Key result: Strain recovery increases with increasing Σ_0.

to the yielding of the negatively strained elements in group (ii), which eventually resolves to a steady strain as the yielding of elements with positive strain in group (i) eventually equals that of elements in group (ii).

The simulations in Fig. 6.6 display significant recoverable strain. Some have recovered over 90% of the strain from its value at $t = t^+_{\text{stop}}$ (just after the stress has been removed). These high values of recoverable strain are similar to those found in literature for protein gels [152] and colloidal gels [57, 59].

It is clear from these results how the imposed stress Σ_0 affects the degree of recoverable strain under the creep-recovery test. Specifically, as Σ_0 increases, the recoverable strain $\Delta\gamma_{\text{rec}}$ increases. This relationship between the recoverable strain $\Delta\gamma_{\text{rec}}$ and the imposed stress Σ_0 was found experimentally for a polymer melt under an elongation creep-recovery test [140]. This may initially seem counter-intuitive, because one might expect a larger imposed stress to result in less recoverable strain. However, because the forward strain is controlled, all systems experience the same strain change $\Delta\gamma_{\text{f}}$ regardless of the size of the imposed stress. This means that smaller stresses are held for longer before being switched off, in order to acquire the same amount of forward strain.

As discussed in Section 6.3, the value of the imposed stress Σ_0 controls the backwards shift that the system experiences upon the removal of the stress. The larger Σ_0, the more negative the minimum strain of the elements in group (ii) is. When the elements in group (ii) have a more negative strain, the yielding from this group will be more significant, resulting in a larger negative strain rate.

Also notable in Fig. 6.6 is the simulation with $\Sigma_0 = 1.7$ (the orange line), in which the strain increases slightly before settling to a steady value. This is an example of the recoverable strain with non-monotonicity discussed in Section 6.3.3.

The dependence of recoverable strain $\Delta\gamma_{\text{rec}}$ on the imposed step stress Σ_0 is explored further in Fig. 6.7. The recoverable strain $\Delta\gamma_{\text{rec}}$ is plotted normalised by the controlled forward strain $\Delta\gamma_{\text{f}}$ to provide the proportion of recoverable strain. Note

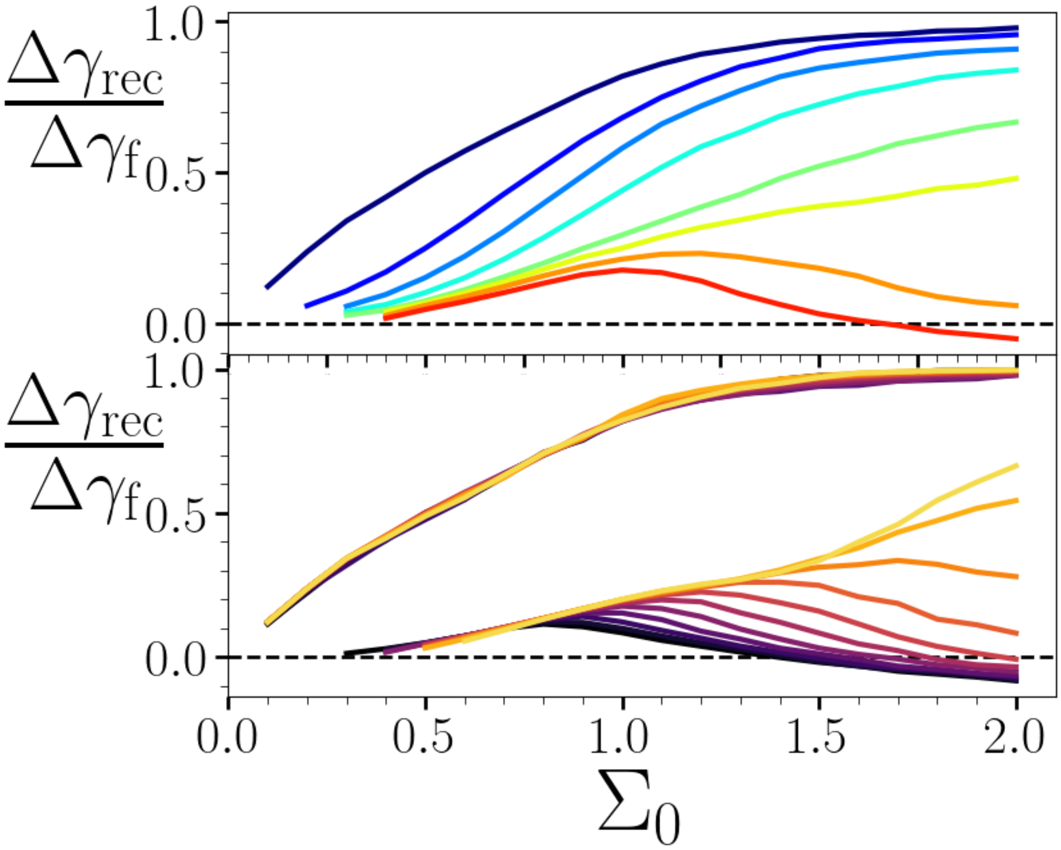

Figure 6.7: **Top Panel**: The proportion of recoverable strain $\Delta\gamma_{\rm rec}$ normalised by the controlled forward strain $\Delta\gamma_{\rm f}$, as a function of the imposed stress Σ_0 for a range of controlled forward strains $\Delta\gamma_{\rm f} = [0.1, 0.5, 1.0, 1.5, 2.0, 2.2, 2.5, 3.0]$ (from blue to orange or top to bottom) and waiting time $t_{\rm w} = 10^3$.
Bottom Panel: The measurement described above, but for two controlled forward strains $\Delta\gamma_{\rm f} = 0.1$ (top group) and $\Delta\gamma_{\rm f} = 3.0$ (bottom group) and a range of waiting times $t_{\rm w} = [10^1, 10^{1.5}, ..., 10^6]$ (from black to yellow or bottom to top in the bottom group of lines).
Key result: Outside of extremes, $\Delta\gamma_{\rm f}$ increases with increasing Σ_0.

that $\Delta\gamma_{\mathrm{rec}}/\Delta\gamma_{\mathrm{f}} = 1$ corresponds to full recovery, and that $\Delta\gamma_{\mathrm{rec}}/\Delta\gamma_{\mathrm{f}} = 0$ corresponds to zero recovery.

The data sets for $\Delta\gamma_{\mathrm{f}} \leq 2.2$ in the top panel of Fig. 6.7 show the general behaviour described earlier, where $\Delta\gamma_{\mathrm{rec}}$ increases as Σ_0 increases. However, this behaviour changes significantly when $\Delta\gamma_{\mathrm{f}} > 2.2$ (the orange and red lines), where the recoverable strain $\Delta\gamma_{\mathrm{rec}}$ initially increases before decreasing, with one line reaching negative values $\Delta\gamma_{\mathrm{rec}} < 0$.

Recalling the definition of $\Delta\gamma_{\mathrm{rec}}$ in Eq. (6.2.1), it is clear that for $\Delta\gamma_{\mathrm{rec}}$ to become negative, the steady state strain γ_{ss} must be larger than the strain immediately after the stress is switched off, equal to $\Delta\gamma_{\mathrm{f}}$. This is the effect of negative recoverable strain discussed in Section 6.3.4. It is clear from the bottom panel of Fig. 6.7 that this effect is suppressed by increasing the waiting time t_{w}, as previously argued.

Despite the outliers, it is clear from these results that generally, outside the extreme values of the controlled forward strain $\Delta\gamma_{\mathrm{f}}$, the recoverable strain $\Delta\gamma_{\mathrm{rec}}$ increases with increasing step stress amplitude Σ_0.

6.5 Dependence of recoverable strain on $\Delta\gamma_{\mathrm{f}}$

The strain decay γ as a function of the time after the stress switch-off is shown for a range of controlled forward strains $\Delta\gamma_{\mathrm{f}}$ in Fig. 6.8. Note that the strain is normalised by the controlled forward strain $\Delta\gamma_{\mathrm{f}}$, which is equal to the strain immediately after the stress switch-off. This allows the different starting positions to be super-imposed and a focus on the proportion of recoverable strain over time. The general behaviour of the majority of these simulations again reflects that described in Section 6.2, Section 6.3.1 and Section 6.3.2, with significant recoverable strain present.

The overall relationship between the controlled forward strain $\Delta\gamma_{\mathrm{f}}$ and the recoverable strain $\Delta\gamma_{\mathrm{rec}}$ appears to be the inverse of that between the imposed stress Σ_0 and $\Delta\gamma_{\mathrm{rec}}$. Indeed, as $\Delta\gamma_{\mathrm{f}}$ increases, $\Delta\gamma_{\mathrm{rec}}$ decreases. This is a more intuitive result, because with

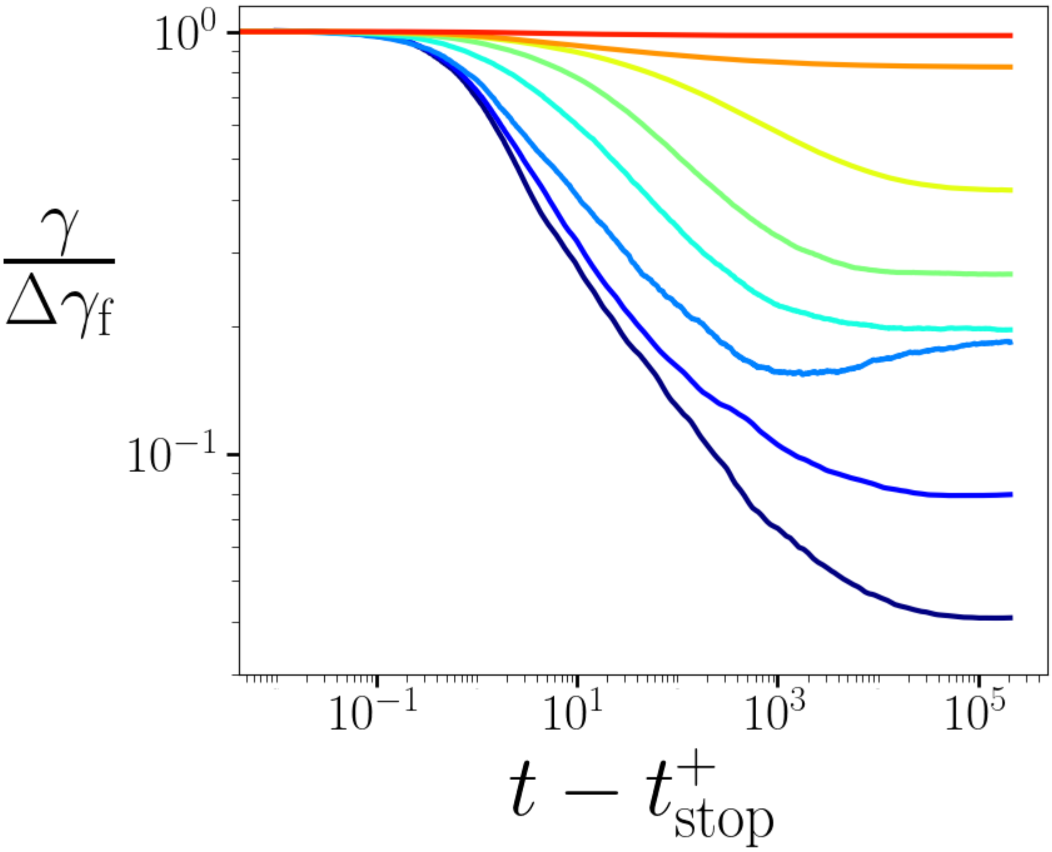

Figure 6.8: The strain response γ normalised by the controlled forward strain $\Delta\gamma_\mathrm{f}$ as a function of time after the stress switch-off for a single imposed step stress $\Sigma_0 = 1.0$, waiting time $t_\mathrm{w} = 10^3$ and a range of controlled forward strains $\Delta\gamma_\mathrm{f} = [10^{-2}, 10^{-1.75}, 10^{-1.5}, 10^{-1}, 10^{-0.5}, 10^0, 10^{0.5}, 10^1]$ (from bottom to top or dark blue to red).
Key result: Strain recovery decreases with increasing $\Delta\gamma_\mathrm{f}$.

a large forward strain, one might expect the material to be too damaged to recover. Indeed, this general relationship between recoverable strain and the change in strain was found experimentally for bread dough and collagen under the creep-recovery test [19, 122], and for protein gels and colloidal gels under shear startup [51, 57, 131].

The reversible plasticity literature also finds a similar trend in other rheological protocols, for example, high levels of reversible plasticity are seen in small strain amplitude oscillatory shear, which is gradually overwhelmed by irreversibility for increasing strains, in experiments on dense jammed suspensions [147] and bubble systems [149]. Increasing irreversibility translates to the failing of the elastic regions that surround the small-scale reversible plasticity, where the plasticity grows to scales where it is no longer reversible [149].

As discussed in Section 6.3, the cause of the relationship between $\Delta\gamma_\mathrm{rec}$ and $\Delta\gamma_\mathrm{f}$ in the SGR model is that $\Delta\gamma_\mathrm{f}$ determines the strain of elements in group (i). If $\Delta\gamma_\mathrm{f}$ is large, the positively strained elements in group (i) will have a large strain. Consequently, there will be a high rate of yielding from this group causing a forward straining that will limit the amount of backwards straining the system is able to achieve. In addition, the larger $\Delta\gamma_\mathrm{f}$ will smooth out the distribution of group (ii), and if larger than the imposed stress Σ_0, will make a proportion of its elements positively strained. This will also help to limit the amount of backwards strain recovery.

The non-monotonic strain behaviour that was discussed in Section 6.3.3 is clear in the simulation with $\Delta\gamma_\mathrm{f} = 10^{-1.5}$ in Fig. 6.8. This strain response clearly increases with time after a substantial initial decrease before finally settling to a steady state.

The important result here is that the recoverable strain $\Delta\gamma_\mathrm{rec}$ increases with decreasing controlled forward strain $\Delta\gamma_\mathrm{f}$. This is shown more fully in the top panel of Fig. 6.9, where this dependence is plotted for a range of imposed stresses Σ_0. However, again, at the extreme values of $\Delta\gamma_\mathrm{f} \gtrsim 3$ and $\Sigma_0 \gtrsim 2$, the recoverable strain drops past zero and into negative values. This effect is again suppressed by increasing t_w, as can be seen in the bottom panel of Fig. 6.9.

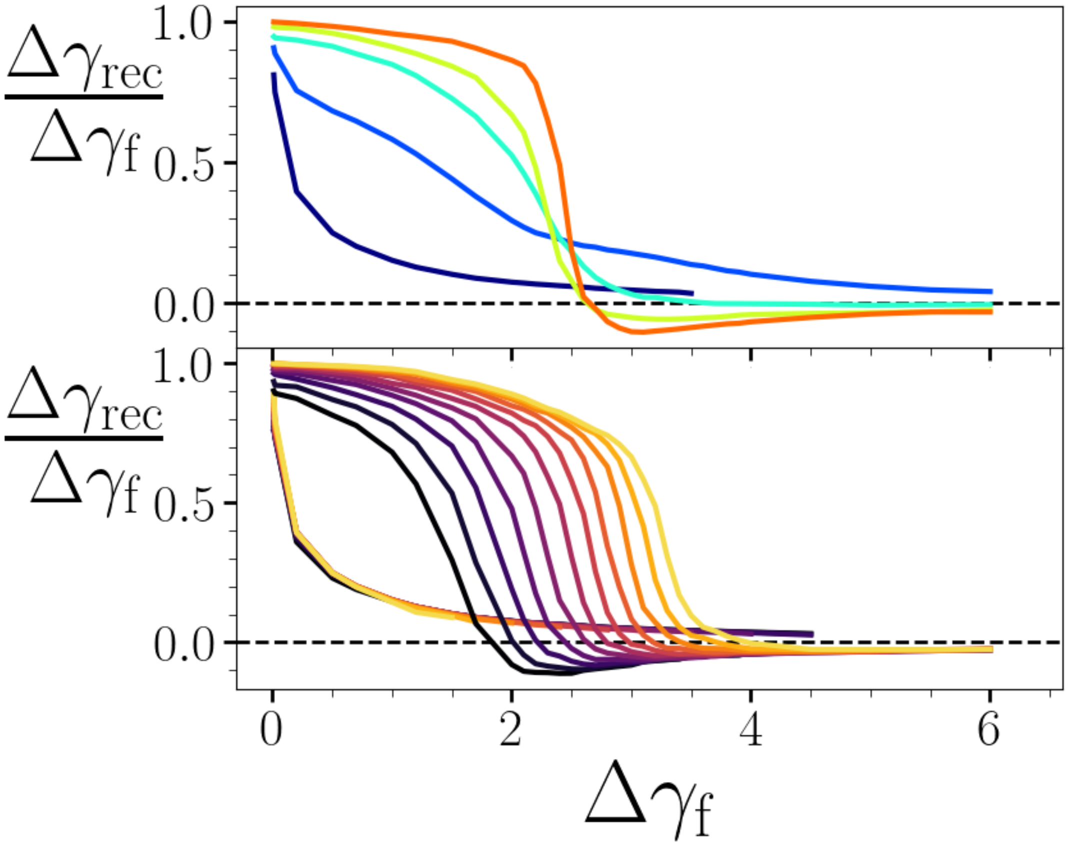

Figure 6.9: **Top Panel**: The proportion of recoverable strain $\Delta\gamma_\mathrm{rec}$ normalised by the controlled forward strain $\Delta\gamma_\mathrm{f}$, as a function of the controlled forward strain $\Delta\gamma_\mathrm{f}$ for a range of imposed step stresses $\Sigma_0 = [0.5, 1.0, 1.5, 2.0, 3.0]$ (from blue to orange or bottom to top at $\Delta\gamma_\mathrm{f} = 1$) and waiting time $t_\mathrm{w} = 10^3$.
Bottom Panel: The measurement described above, but for two imposed step stresses $\Sigma_0 = 0.5$ (left group) and $\Sigma_0 = 2.0$ (right group) and a range of waiting times $t_\mathrm{w} = [10^1, 10^{1.5}, ..., 10^6]$ (from black to yellow or left to right in the right group of lines).
Key result: Outside of extremes, $\Delta\gamma_\mathrm{f}$ decreases with increasing $\Delta\gamma_\mathrm{f}$.

What is also interesting about the top panel of Fig. 6.9 is the overlap of lines for different Σ_0, which occurs around $\Delta\gamma_\mathrm{f} \sim 3$, in the same region where the surprising non-monotonic behaviour of $\Delta\gamma_\mathrm{rec}$ with Σ_0 behaviour started in Fig. 6.7. All of this behaviour is a consequence of the negative recoverable strain (at large values of $\Delta\gamma_\mathrm{f}$ and Σ_0) discussed in Section 6.3.4.

Despite the negative recoverable strain, it is clear from these results that generally, outside these extreme values, the recoverable strain $\Delta\gamma_\mathrm{rec}$ decreases with increasing controlled forward strain $\Delta\gamma_\mathrm{f}$.

6.6 Dependence of recoverable strain on t_w

The strain decay γ as a function of time is shown for a range of waiting times t_w in Fig. 6.10. The overall relationship between the waiting time t_w and the recoverable strain $\Delta\gamma_\mathrm{rec}$ is the same as between the imposed stress Σ_0 and $\Delta\gamma_\mathrm{rec}$. As t_w increases, $\Delta\gamma_\mathrm{rec}$ increases. This can be understood intuitively in terms of a better aged material being more resistant to strain and therefore more likely to recover lost strain after creep.

As discussed in Section 6.3, t_w determines the depths of the energy wells of elements in group (i). If t_w is large, the elements in group (i) have, on average, large energy well depths $E \gg 1$, as explained in Section 3.1.1. This means that the timescales for relaxation of this group of positively strained elements is long. Consequently, elements in group (ii) are likely to yield on a shorter timescale, creating a negative strain rate that results in significant recoverable strain. Note that the waiting time t_w has no effect on the energy well depths of group (ii) because they have yielded since the ageing process, and have therefore left their age-dependent energy well.

The converse of this argument can explain the surprising result for the low values of t_w in Fig. 6.10 (dark purple lines), where the strain increases after the stress switch-off. In this case, a small waiting time t_w causes the average element energy

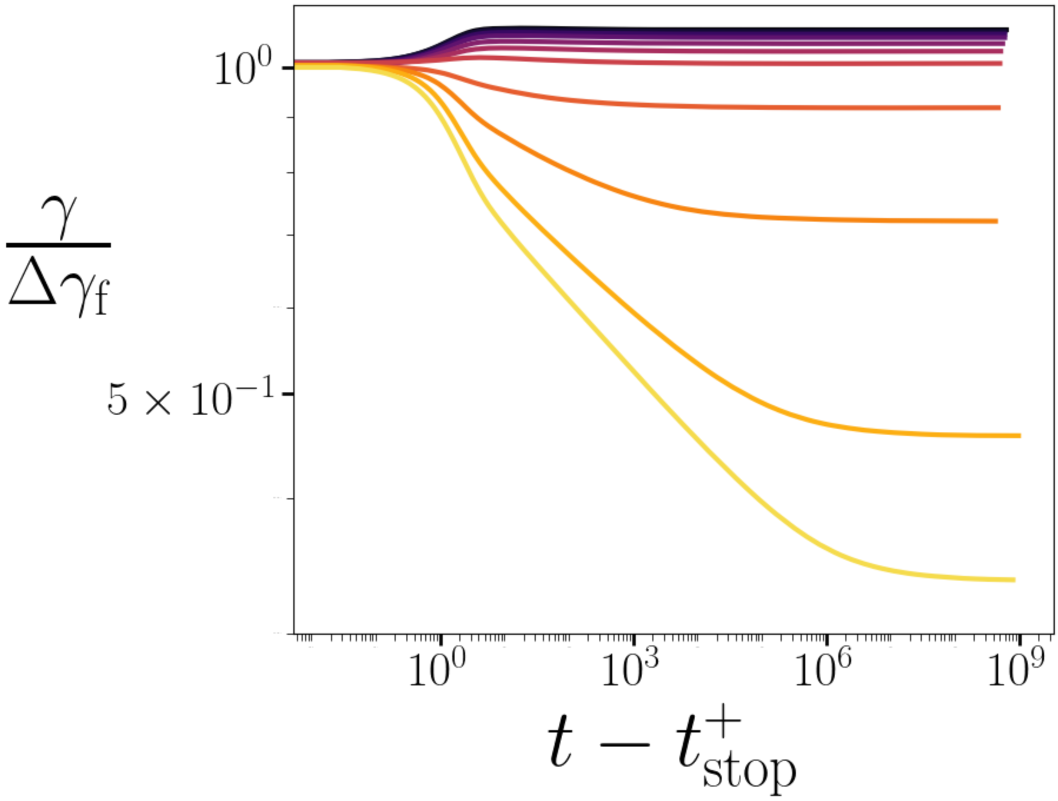

Figure 6.10: The strain response γ normalised by the controlled forward strain $\Delta\gamma_f$ as a function of time after the stress switch-off for a single imposed step stress $\Sigma_0 = 2.0$, controlled forward strain $\Delta\gamma_f = 3.0$, and a range of waiting times $t_w = [10^1, 10^{1.5}, ..., 10^6]$ (from black to yellow or top to bottom).

Key result: Strain recovery increases with increasing t_w.

well depth E of group (i) to be small, meaning a small timescale for relaxation. The element yielding in group (i) therefore initially dominates over the yielding of group (ii), causing a positive strain rate. This is later balanced by the yielding in group (ii) leading to an ultimate strain that is larger than the initial strain after the stress removal $\gamma_{ss} > \gamma(t^+_{stop}) = \Delta\gamma_f$. This behaviour is the cause of the negative recoverable strains $\Delta\gamma_{rec}$ seen in Fig. 6.7, Fig. 6.9 and discussed further in Section 6.3.4.

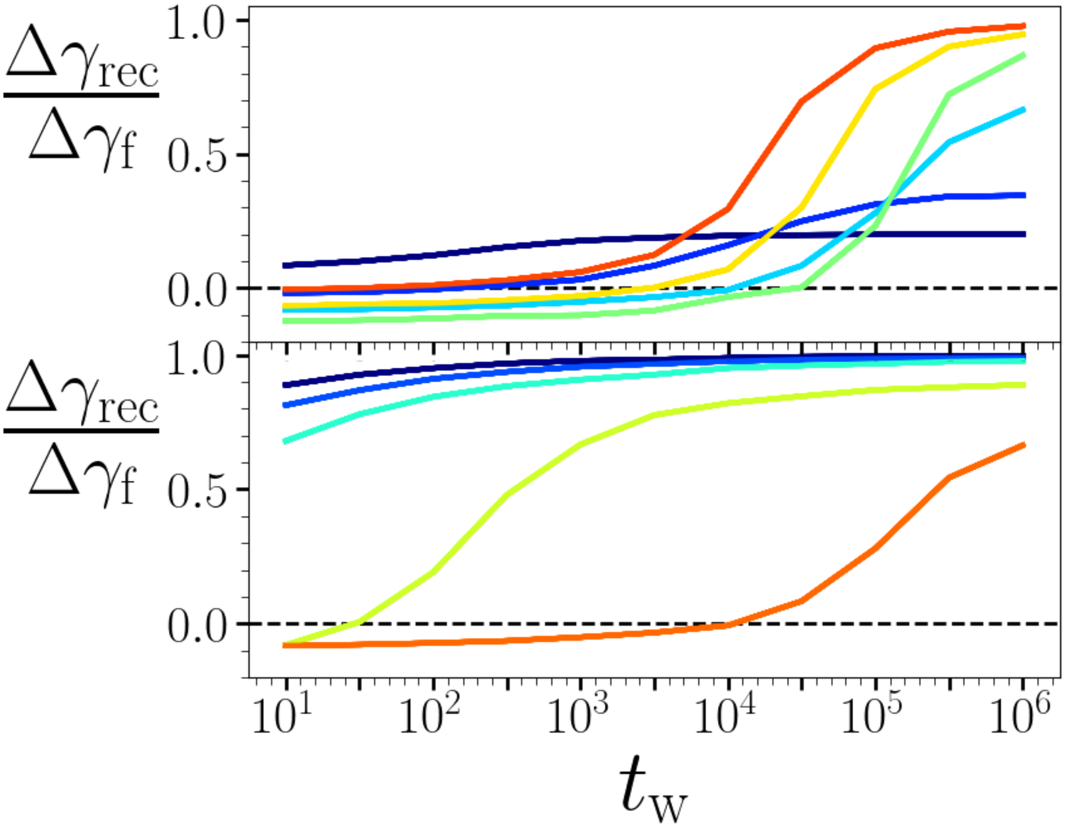

Figure 6.11: **Top Panel**: The proportion of recoverable strain $\Delta\gamma_{rec}$ normalised by the controlled forward strain $\Delta\gamma_f$, as a function of the waiting time t_w for a range of imposed step stresses $\Sigma_0 = [0.5, 1.0, 1.5, 2.0, 3.0, 4.0]$ (from blue to red or bottom to top at $t_w = 10^6$) and controlled forward strain $\Delta\gamma_f = 3.0$.
Bottom Panel: The measurement described above, but for an imposed step stress $\Sigma_0 = 2.0$ and a range of controlled forward strains $\Delta\gamma_f = [0.1, 0.5, 1.0, 2.0, 3.0]$ (from blue to orange or top to bottom).
Key result: $\Delta\gamma_f$ increases with increasing t_w.

The effect of the waiting time t_w for a range of imposed stresses Σ_0 and controlled forward strains $\Delta\gamma_{\mathrm{f}}$ is shown in Fig. 6.11. Generally, it is clear that increasing t_{w} also increases the amount of recoverable strain $\Delta\gamma_{\mathrm{rec}}$. However, it is also clear that t_{w} has a much more significant effect when Σ_0 and $\Delta\gamma_{\mathrm{f}}$ are large, because the variation in the curves is much larger for the yellow and orange lines. This highlights the behaviour also found in the bottom panels of Fig. 6.7 and Fig. 6.9, where the variation of t_{w} has minimal effect on $\Delta\gamma_{\mathrm{rec}}$ for small values of Σ_0 and $\Delta\gamma_{\mathrm{f}}$, but has a significant impact when these values are large.

The effect of t_{w} only becomes apparent at these extremes because generally the behaviour is dominated by the negatively strained elements in group (ii), which have no knowledge of the value of t_{w}. Only when the yielding of the positively strained elements in group (i) becomes relevant does t_{w} have a significant impact.

In addition, the effect of rising strain causing negative recoverable strain $\Delta\gamma_{\mathrm{rec}} < 0$, though interesting, is also only seen at the extreme values of $\Delta\gamma_{\mathrm{f}} \gtrsim 3.0$ and $\Sigma_0 \gtrsim 1.5$ (see Fig. 6.7 and Fig. 6.9). This brings into question how physical the results are at these values. There is some experimental evidence for this kind of effect in other rheological protocols, a residual stress higher than the stress immediately after the removal of a strain rate was observed in a colloidal gel [57]. However, part of the rationale for using the SGR model with enforced shear homogeneity is that generally for the controlled forward strains considered here $\Delta\gamma_{\mathrm{f}}$, the system would have built up minimal heterogeneity, so the approximation to homogeneous behaviour is valid. However, for strains around $\Delta\gamma_{\mathrm{f}} \gtrsim 3.0$, under step stress, a system can build-up significant heterogeneities in shear [9, 19, 110, 114, 158]. This can be seen in the results in Chapter 5 which, although using a modified SGR model, show significant shear heterogeneity build-up for forward strain values $\gamma \gtrsim 2.0$. Also, relaxation from values of step strains on this scale $\gamma_0 \gtrsim 2.0$ in Chapter 4 resulted in highly heterogeneous flows after a delay time.

Therefore, while the surprising behaviour at large values of Σ_0 and $\Delta\gamma_{\mathrm{f}}$ can be understood through the model, it should be tested with allowed shear heterogeneity before any statement on its physicality can be made. This is outside the scope for this project, but is discussed as future work in Section 6.7.

The conclusion from this section is that, outside of extreme values, an increase in the age of the material represented by the waiting time t_{w} has a small but positive effect on the recoverable strain $\Delta\gamma_{\mathrm{rec}}$.

6.7 Conclusion

This chapter has shown that the SGR model under enforced homogeneity can display significant (over 90%) recoverable strain under the creep-recovery test protocol. In addition, strong dependencies for the degree of recoverable strain $\Delta\gamma_{\mathrm{rec}}$ on the relevant input parameters have been predicted. Typically, $\Delta\gamma_{\mathrm{rec}}$ increases with increasing imposed step stress Σ_0, with decreasing controlled forward strain $\Delta\gamma_{\mathrm{f}}$, and with increasing age or annealing, represented by the waiting time t_{w}.

Analysis of the element behaviour during relaxation shows that, contrary to expectation, any recoverable strain is a direct consequence of plastic rearrangement events in the system, a concept known as reversible plasticity [58, 135–139, 145–151]. This could dramatically change how the origins of recoverable strain are understood. Despite the simplicity of the SGR model, complex element behaviour also results in non-monotonic strain responses in creep recovery. The non-monotonic time dependence of rheological response functions is an area of interest in the amorphous materials literature [28, 44, 56, 57, 158, 173, 237–240].

Significant recoverable strain has been found experimentally in several gel systems [57, 59, 152]. One of these studies showed non-monotonic stress responses after the switch-off of a shear startup in which the stress grew during recovery, which provides an experimental counterpart to the complex behaviour predicted in this work [57]. The dependencies for the degree of recoverable strain $\Delta\gamma_{\mathrm{rec}}$ predicted in this work are also evidenced experimentally, the increase in $\Delta\gamma_{\mathrm{rec}}$ with increasing stress Σ_0 in a low density polymer melt [140] and with decreasing controlled forward strain $\Delta\gamma_{\mathrm{f}}$ in a range of systems [19, 51, 57, 122, 131].

The SGR model has been successful modelling a wide range of dense complex materials, from colloidal dispersions to emulsions [13,24,25]. Now that the phenomenon of significant recoverable strain has been found in the SGR model, it is hoped that this will motivate experimental studies to explore it in these materials. This could then lead to new applications for highly recoverable amorphous materials. In addition, modern experimental tools allow the study of internal dynamics of systems, which could help illuminate the origins of this recoverable strain, which this work predicts to be a consequence of reversible plasticity in a Bauschinger-like effect.

This work lays the foundation for the SGR model to become a tool in the simulation of amorphous materials where strain recovery is important. These include hydrogels [52–55,127,130,131], shape memory polymers [132–139], and polymer melts [128,140,141]. Such materials have applications in medical tools and material processing, with their recoverability an important property in these applications [133,134,141,142]. This work increases understanding in not only the dependencies of recoverable strain on the relevant control parameters, but also how and why recoverability occurs.

Further work in this area could include:

- **Including shear heterogeneity** - As mentioned previously, the results presented can only be considered physical under conditions where the assumption to homogeneous shear is valid. This is true for values of the controlled forward strain small enough to ensure the system stays in primary creep $\Delta\gamma_{\mathrm{f}} \lesssim 2.0$, where the build-up of shear heterogeneity is minimal. For these values, the results are not expected to change even if heterogeneity was allowed, because the system remains approximately homogeneous in shear. However, for values of $\Delta\gamma_{\mathrm{f}}$ larger than this, significant heterogeneity is expected to form. This could change how the system relaxes once the stress has been switched off. This regime is also where the surprising negative recoverable strain $\Delta\gamma_{\mathrm{rec}} < 0$ appeared. It is worth investigating this regime to see if this behaviour remains when heterogeneity in shear is allowed, or if even more interesting behaviour arises. In addition, allowing shear heterogeneity could also present the added complexity of significant shear bands forming. These could form during the application of the stress, similar to that seen in Chapter 5, or could even form during the relaxation, similar to the relaxation from a step strain found in Chapter 4.

- **Other recovery test protocols** - As outlined in the introduction, the creep-recovery test is not the only way of testing the recoverability of amorphous materials. Simulating the SGR model for other protocols, such as relaxation from an oscillatory shear [126, 143, 144] or shear startup [153], could further expand on the results presented here, and would allow for further experimental comparison. In addition, the creep-recovery test protocol presented here can be extended to multi-stress creep recovery, which has been experimentally explored for protein gels [152] and is an important regulation test for asphalt production [190, 191]. Also, the work in this chapter presented an explanation of the reversible plasticity seen in the process of recovering strain, and likened it to the Bauschinger effect of solids [230–232]. It would be interesting to see whether the phenomena presented in this work remain under alternative protocols.

- **Changing the timescale for reformation** - In this work, the usual assumption in the SGR model of instantaneous reformation of an element post-yield has been made, meaning the timescale for element reformation is zero $\tau_{\text{reform}} = 0$. However, part of the inspiration for this work came from the supplementary material [152] of a key reference [110] in Chapter 5, which found that protein gels under creep could recover over 90% of their strain if the stress was switched off after some time. In Chapter 5 it was argued that the SGR model with breakable elements, using an infinite timescale for reformation $\tau_{\text{reform}} = \infty$, was a good model for protein gels. Therefore, it is logical to test how the degree to which strain is recoverable in SGR-like systems changes when elements are no longer allowed to reform, more accurately reflecting the recovery of protein (and other irreversibly breakable) gels [19,27,59,182]. This would significantly change the process through which recoverable strain is achieved, because the elements that yield during the step stress would not be able to reform. Therefore, when the stress is switched off, these broken elements that previously (with element reformation) contributed to recoverable strain by relaxing their negative strains would be unable to support the strain and would relax immediately, creating an interesting scenario for recoverable strain.

- **Investigating temperature variation** - This work has not studied the variation of recoverable strain $\Delta\gamma_{\rm rec}$ on the working temperature x. However, this could significantly impact the strain recovery of these systems, because the general impact of increasing x is to increase the rate of yielding. There is also experimental motivation to explore this variable, with variation in temperature having a significant impact on the recoverability of shape memory polymers [132] and the rheology of polymer melts [141]. In addition, research into creep-recovery tests on collagen suggest working temperatures above the glass temperature $x > x_g$ [19], which this study does not explore. Also, the reversible plasticity in some shape memory polymers is activated by temperature [135, 136, 138, 139]. Indeed, there could be even more interesting behaviour in the athermal limit $x \to 0$, where the yielding rate function $r(l)$ becomes a step function, as analysed in Chapter 4, which also looked at relaxation, but of systems under a step strain.

- **Exploring other non-monotonic behaviour** - The SGR model has been shown to simulate complex non-monotonic strain recovery behaviour. Accordingly, it would be interesting to investigate whether it is possible that other non-monotonicities such as those discovered under the relaxation of a colloidal gel from a constant strain rate could be captured within the SGR model [57].

- **Testing the timescales** - The time to reach the controlled forward strain $\Delta\gamma_{\mathrm{f}}$ and the time to reach the steady state strain γ_{ss} were not studied in this work. However, the observed increase in strain recovery with increasing t_{w} implies that the longer it takes to reach $\Delta\gamma_{\mathrm{f}}$ the more recoverable strain, because a larger t_{w} will delay the time taken to reach $\Delta\gamma_{\mathrm{f}}$. On the other hand, the observed increase in strain recovery with increasing Σ_0 implies that the longer it takes to reach $\Delta\gamma_{\mathrm{f}}$ the less recoverable strain, because a larger Σ_0 will decrease the time taken to reach $\Delta\gamma_{\mathrm{f}}$. This is an interesting juxtaposition, and the conclusion from this work is that the other impacts of these variables are more important, particularly when the amount of strain change is controlled. However, it is possible that there is more complex behaviour in the build-up to the stress removal than accounted for in this work. In addition, the rate of recoverable strain is an important variable in the processing of hydrogels, polymer melts, and asphalt, and so is also a worthy avenue of investigation [131, 141, 190].

- **Varying the viscosity** - The work in this chapter features a solvent viscosity set to zero. Testing the phenomena with a small but non-zero solvent viscosity does not change the results presented. However, this has only been tested for increasingly small viscosities, as is standard in the SGR model to minimise the effect of the solvent. One study has suggested that the irrecoverable strain present in protein gels under the creep-recovery test protocol could be attributed to viscous solvent flow within the porous structure of the gel [152]. Making the solvent viscosity significant could therefore affect the levels of recoverable strain and would test this experimental finding.

- **Experimental exploration** - As mentioned previously, it would be interesting to perform experimental studies into recoverable strain on a wider range of materials. Experiments could also attempt to observe the mesoscopic rearrangement events described above, to investigate whether reversible plasticity and the Bauschinger effect can be connected to the concept of recoverable strain in soft matter, as predicted here. This finding could provide a clear explanation for the origin of recoverable strain, and create a connection between the appearance of the Bauschinger effect in crystalline solids and amorphous fluids.

Chapter 7

Conclusion

This thesis has explored the yielding, relaxation and recovery of amorphous material through three rheological shear protocols. The mesoscopic models used to computationally simulate these systems have been shown to replicate experimentally observed phenomena, and also predict new ones. The applications of amorphous materials have been outlined throughout, from the biological systems essential to life [5–7, 20–22], to manufacturing industries [9, 13–15] and geological systems [3, 17].

By utilising and expanding on simple generic models in the literature [9], this work is intended to apply to a wide range of amorphous materials, from dense suspensions [8,23–25] to low density structures [26–33]. This is because the disordered mesoscopic substructures present in the models are universal in amorphous materials [9, 23, 25, 71, 81, 81]. Consequently, rheological effects such as ageing [71, 81, 83], non-monotonic strain curves [28, 44, 56, 57, 158, 173, 237–240], and shear banding [8–11,84–86,90] can be simulated. These effects are important not only in a material's shear properties but also because, particularly in the latter case, they can lead to failure, fluidisation and fracture [8–11, 84–86, 90].

Scientific progress is founded on collaboration between experimental and theoretical study. Theoretical work can reveal insights into material behaviour, experimental results, and manufacturing processes. In particular, the stresses and strains found in the physical applications of these materials can be simulated under common shear protocols. Simulations can also predict new phenomena, and suggest avenues for experimental exploration. The work in this thesis is therefore a contribution, upon which further experimental and theoretical work can be built.

In Chapter 4, amorphous materials were simulated with the Soft Glassy Rheology (SGR) and Thermal Elasto-Plastic (TEP) models outlined in Sections 2.2 and 2.3 under the step strain protocol described in Section 2.5.1. The key result was the discovery of highly delayed catastrophic shear banding, a long time after the initial imposition of the strain. Theoretical and experimental studies prior to this work have generally focussed on the appearance of banding within short timescales [65–67, 69, 87, 185–187, 213]. It has perhaps been assumed, due to the absence of any final flowing state, that the stress relaxation at long times after the initial step strain will take place homogeneously in shear. However, data from a step strain experiment on a hydrogel found preliminary evidence for the highly delayed banding predicted in this work [214].

The work in Chapter 4 not only predicts the delayed banding described above, but also demonstrates strong parameter dependencies for the time of banding. In particular, the simulations show that the banding time increases dramatically with decreasing amplitude of the (long historical) imposed strain, with decreasing working temperature, and with increasing levels of sample annealing or ageing prior to shear. These ultra-delayed flow-gradient heterogeneities are predicted by both the SGR and TEP models, in addition to correlating with studies within a continuum fluidity model from a collaborator [91]. The qualitative agreement of these models, which are widely used in literature, in addition to the different sample preparation protocols utilised in each, imply that the phenomena may be generic across amorphous materials.

This finding could have wide implications for the processing and use of amorphous materials [158]. For example, in manufacturing, amorphous materials can be stored for large periods of time [74, 75]. If there are unresolved strains within a material, it could catastrophically fail after a long delay time, which could not be predicted without knowledge of its strain history. The research provided in this study of how instabilities form within systems and how the delay time of the consequential failure depends on the material parameters could potentially help these industries predict or diagnose problems and apply preventative measures.

Further work in this study, detailed in Section 4.4, could include using a range of other theoretical models within the amorphous material literature to further strengthen the predictions made by the mesoscopic and macroscopic models used already [9, 224]. However, this research is primarily intended to motivate targeted experimental studies for finding this delayed banding phenomena. The work in this chapter makes clear how this might be achieved experimentally, by outlining the parameter dependence of banding, and how a 'rapid strain ramp' can access the step in strain, as discussed in Section 2.5.1 [185, 186].

In Chapter 5, amorphous materials were simulated with a modified SGR model under the step stress protocol described in Section 2.5.2. The modification, new in this work and outlined in Section 2.4, disallows the reformation of mesoscopic elements, with the aim of more closely simulating the permanent breaking of fibres in protein gels [19, 27, 59, 182]. Protein gels are of interest for their applications both in biological systems [27–30, 32], such as in fish protein [28], and also in the food industry [31, 120–122].

Although the step stress protocol has been thoroughly studied for amorphous materials [9, 11, 25, 25, 28, 36, 81, 87, 87, 107–109, 112–116], theoretical research prior to this one generally focusses on systems in which the mesoscopic substructures reform after yielding. Studies into protein gels show the breaking of network bonds that do not reform [19, 27, 59, 182], of which the breakable spring-like system in fibre bundle models provide a simplified representation [9, 106, 107, 110, 157, 227, 228]. Taking inspiration from these studies, combining the breakability of the fibre bundle models [9, 106] with the complex energy landscape and capacity for shear banding of the SGR model [13, 23–25, 71, 81, 92, 172] creates a system aimed at simulating the failure of protein gels under creep.

The key results correlate closely with experimental observations and the predictions of fibre bundle models [28,110]. This includes good fittings to the Basquin law of fatigue [227,228], primary Andrade creep [9,28,36,51,110,114], Monkman-Grant relation [189], and the three creep regimes of the strain rate response [110,157]. It advances beyond the results of the fibre bundle models by providing an understanding of the build-up of heterogeneity during creep. In replicating experimental observations, while also allowing a spatial resolution of the strain field across the material, the results reveal an insight into the precursors to failure, of interest in the literature [9,112,158]

By prohibiting element reformation, the SGR model becomes a strong candidate for simulating protein gels, and for understanding experimental results. Further work, as detailed in Section 5.6, could include expanding on this study by exploring other rheological protocols with this new model, such as in shear startup [9,67,71,87]. Alternatively, making further changes to the model could target the modelling of specific protein gels, for example by changing the reformation time of elements. In addition, this work has shown the capacity for the SGR model to be adapted to model materials outside of its originally designed systems, and this could be expanded on to further establish it as a tool for simulating a wide range of amorphous materials.

In Chapter 6, amorphous materials were simulated with the SGR model, outlined in Section 2.2, under the creep-recovery test protocol, the application of a step stress for some time before it is switched off, described in Section 2.5.3. The key result was the discovery of significant recoverable strain, an important property in a range of amorphous materials [9,52–55,127,128,130–141].

The work in Chapter 6 also found strong dependencies for the degree of recoverable strain on input parameters, comparable to experimental studies [57,124,140,152,153]. In particular, the degree of recoverable strain increases with increasing imposed stress, decreasing forward strain, and increasing age or annealing. In addition, non-monotonic strain responses as a function of time were discovered as a consequence of the complex behaviour of the mesoscopic elements in the SGR model.

Theoretical studies of the creep-recovery test prior to this one have generally been material specific [124,125]. In contrast, the SGR model used here is generic to a wide range of amorphous materials, from emulsions to colloidal suspensions [13, 23–25, 71, 81, 92, 172], in which it predicts high levels of recoverable strain. The recoverable strain of a material is an important property to study, as it has been shown to provide insights into the microstructural evolution of systems under shear [144], and is relevant to many amorphous material applications [52–55, 127, 128, 130–141], such as in biological collagen [19].

The detailed study into the mesoscopic origins of recoverable strain presented in Chapter 6 reveals a potentially surprising finding. It has generally been assumed that recoverable strain is a consequence of reversible elastic straining, and that plasticity only restricts the recoverability of amorphous systems [45,125,152,190,214]. However, the work here suggests that recoverable strain is actually a result of plastic events, through a process known in the literature as reversible plasticity [58, 135–139, 145–151].

This new discovery of reversible plasticity in the SGR model has the capacity to change the understanding of the origins of recoverable strain in amorphous materials. With its origins primarily in the hard matter literature [145, 230, 231], reversible plasticity has only recently been recognised in soft matter, predominantly through the study of shape memory polymers [135–139]. This study therefore extends the applicability of reversible plasticity as a concept to soft matter more broadly, in particular in the context of amorphous materials with recoverable strain.

Chapter 6 outlines how the SGR model can simulate the strain recovery of amorphous materials, and suggests it as a candidate for future theoretical studies in this area. This further work, outlined in Section 6.7, could include an increased spatial dimensionality, other recovery protocols such as the relaxation from oscillatory shear [41, 159, 208–211], and further model variation, for instance in the exploration of how temperature affects recoverable strain. In addition, experimental studies could reveal the behaviours predicted here in amorphous materials not traditionally expected to be capable of strain recovery.

To conclude, this thesis has explored a range of phenomenological behaviours of amorphous materials under shear protocols. The simulations have captured existing experimental observations, and predicted new phenomena. Nevertheless, from mayonnaise to magma [17, 74], there is still more to discover about this diverse group of disordered systems and multiple avenues of possible future work have been suggested. It is hoped that the results obtained in this thesis, and any of the follow-up studies proposed, will advance insight into the yielding, relaxation and recovery of amorphous materials.

Appendix A

Convergence Checks

In Fig. A.1, Fig. A.2, and Fig. A.3, the results of some of the convergence tests carried out for the work in this thesis can be seen. These show the variation of the number of elements (or the number of discretisation points in strain space, depending on the model) M and the timestep Δt. These are the two key parameters for determining convergence and ensuring that the results are consistent across different seeding for the random number generation involved in the model.

Across all of these figures, it is clear that there is a high consistency between the simulations with $M = 10^5$ and $M = 10^6$, and similarly with $\Delta t = 0.01$ and $\Delta t = 0.005$. Although there are slight differences between the plots, assumed to be a result of noise originating from the random probabilities associated with the models, the differences are negligible, and are not clearly visible on the scale of the simulation. This confirms good convergence for these values.

For all the results presented in this thesis, convergence tests have been carried out to ensure that no behaviour is a result of finite system size or computational randomness.

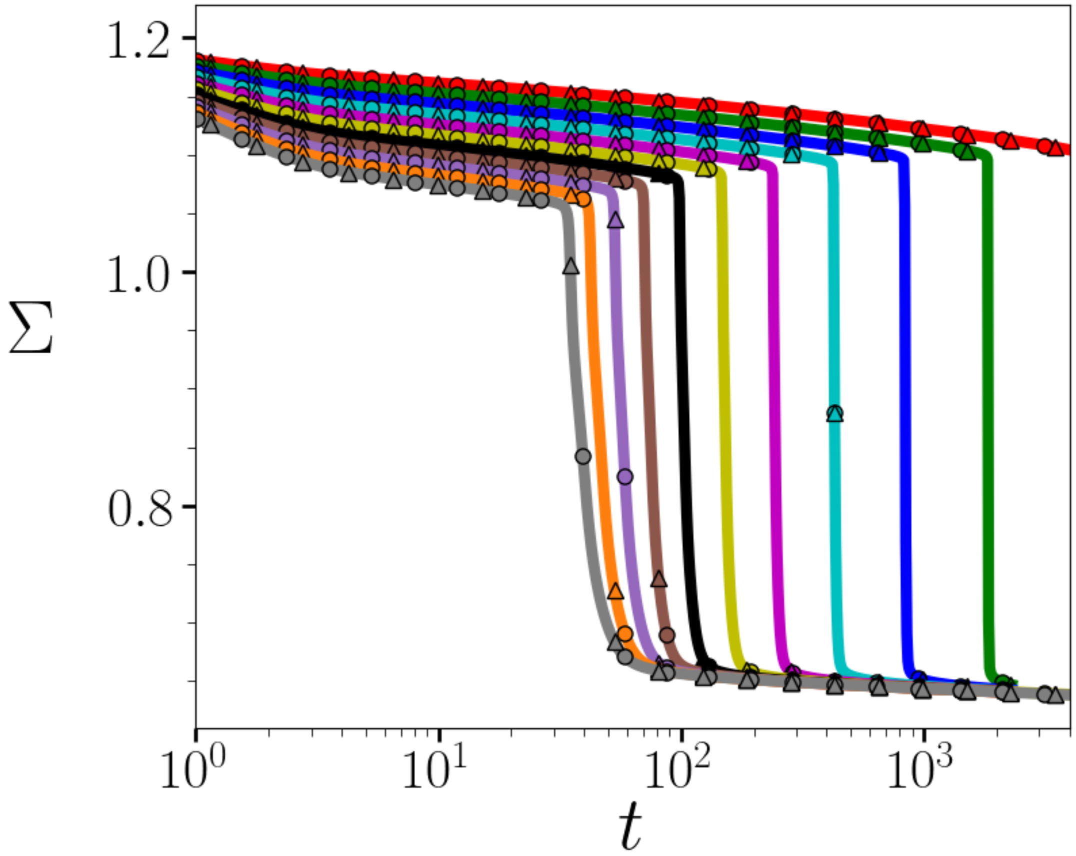

Figure A.1: Stress decay Σ as a function of time t after the imposition of a step strain of amplitude $\gamma_0 = 1.2$, as simulated within the Thermal Elasto-Plastic model, for a range of pre-shear equilibrium temperatures x_0=[0.02, 0.019, ..., 0.01] (in order from grey to red or left to right in the sudden stress drop). For each x_0, the solid line represents the simulation with $M = 10^5$ and $\Delta t = 0.01$, the line with triangles represents simulations with $M = 10^6$, and the line with circles represents simulations with $\Delta t = 0.005$. Each of these three lines has also been plotted for five different seeds of the random number generator used in the model. Although there are differences between the fifteen lines for each x_0, the difference is negligble, and cannot be clearly seen on the scale of the simulation, confirming good convergence with these simulation parameters.

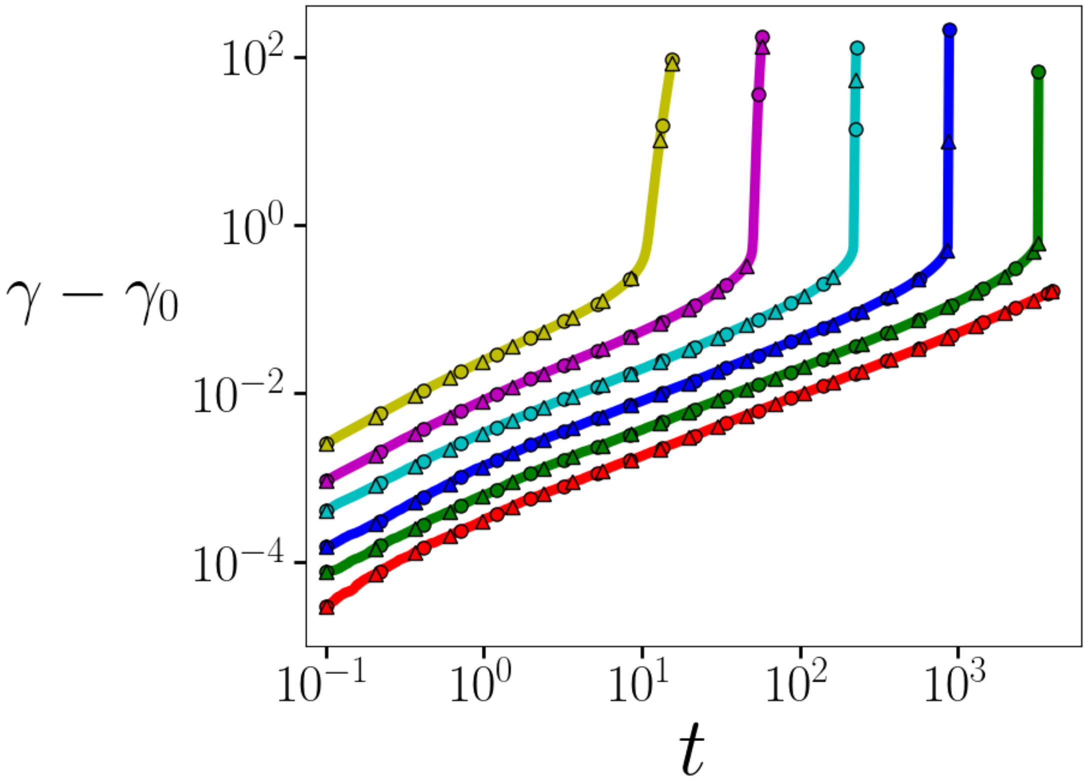

Figure A.2: The strain response γ relative to the initial strain as a function of time t following the imposition of a range of constant step stresses $\Sigma_0 = [1.0, 1.2, ..., 2.0]$ (from bottom to top or red to yellow) after a waiting time $t_\mathrm{w} = 10^5$. For each Σ_0, the solid line represents the simulation with $M = 10^5$ and $\Delta t = 0.01$, the line with triangles represents simulations with $M = 10^6$, and the line with circles represents simulations with $\Delta t = 0.005$. Each of these three lines has also been plotted for five different seeds of the random number generator used in the model. Although there are differences between the fifteen lines for each Σ_0, the difference is negligble, and cannot be clearly seen on the scale of the simulation, confirming good convergence with these simulation parameters.

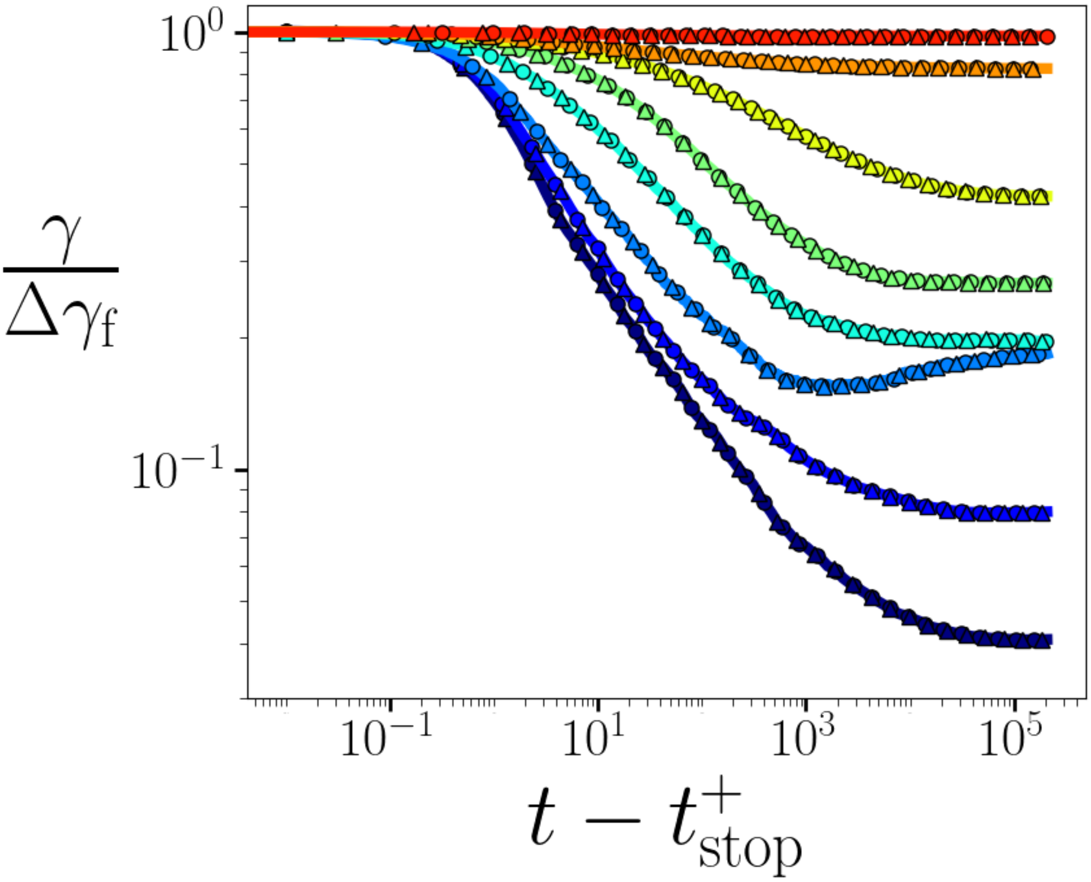

Figure A.3: The strain response γ normalised by the controlled forward strain $\Delta\gamma_f$ as a function of time after the stress switch-off for a single controlled forward strain $\Delta\gamma_f = 0.5$, waiting time $t_w = 10^3$ and a range of imposed step stresses $\Sigma_0 = [0.3, 0.5, ..., 1.9]$ (from top to bottom or dark blue to red). For each Σ_0, the solid line represents the simulation with $M = 10^5$ and $\Delta t = 0.01$, the line with triangles represents simulations with $M = 10^6$, and the line with circles represents simulations with $\Delta t = 0.005$. Each of these three lines has also been plotted for five different seeds of the random number generator used in the model. Although there are differences between the fifteen lines for each Σ_0, the difference is negligble, and cannot be clearly seen on the scale of the simulation, confirming good convergence with these simulation parameters.

Bibliography

[1] P. Coussot and F. Gaulard, *Gravity flow instability of viscoplastic materials: The ketchup drip*, *Phys. Rev. E* **72** (2005) 031409.

[2] P. Bottiglieri, F. D. Sio, G. Fasanaro, G. Mojoli, M. Impembo and D. Castaldo, *Rheological characterization of ketchup*, *Journal of food quality* **14** (1991) 497–512.

[3] P. Coussot, Q. D. Nguyen, H. T. Huynh and D. Bonn, *Avalanche behavior in yield stress fluids*, *Phys. Rev. Lett.* **88** (2002) .

[4] N. M. Pinyol, M. Alvarado, E. E. Alonso and F. Zabala, *Thermal effects in landslide mobility*, *Géotechnique* **68** (2018) 528–545.

[5] R. J. Tetley, M. F. Staddon, D. Heller, A. Hoppe, S. Banerjee and Y. Mao, *Tissue fluidity promotes epithelial wound healing*, *Nature Physics* **15** (2019) 1195–1203.

[6] J. Huang, J. O. Cochran, S. M. Fielding, M. C. Marchetti and D. Bi, *Shear-driven solidification and nonlinear elasticity in epithelial tissues*, *Phys. Rev. Lett.* **128** (2022) 178001.

[7] D. Bi, X. Yang, M. C. Marchetti and M. L. Manning, *Motility-driven glass and jamming transitions in biological tissues*, *Phys. Rev. X* **6** (2016) 021011.

[8] M. L. Falk and J. S. Langer, *Deformation and failure of amorphous, solidlike materials*, *Annu. Rev. Condens. Matter Phys.* **2** (2011) 353–373.

[9] A. Nicolas, E. Ferrero, K. Martens and J. Barrat, *Deformation and flow of amorphous solids: Insights from elastoplastic models*, *Rev. Mod. Phys.* **90** (2018) 045006.

[10] R. G. Larson, *Instabilities in viscoelastic flows*, *Rheologica Acta* **31** (1992) 213–263.

[11] D. Bonn, M. M. Denn, L. Berthier, T. Divoux and S. Manneville, *Yield stress materials in soft condensed matter*, *Rev. Mod. Phys.* **89** (2017) .

[12] X. Trepat, L. Deng, S. S. An, D. Navajas, D. J. Tschumperlin, W. T. Gerthoffer et al., *Universal physical responses to stretch in the living cell*, *Nature* **447** (2007) 592–595.

[13] S. M. Fielding, M. E. Cates and P. Sollich, *Shear banding, aging and noise dynamics in soft glassy materials*, *Soft Matter* **5** (2009) 2378–2382.

[14] S. E. Chidiac and F. Mahmoodzadeh, *Plastic viscosity of fresh concrete–a critical review of predictions methods*, *Cement and Concrete Composites* **31** (2009) 535–544.

[15] P. F. G. Banfill and D. C. Saunders, *On the viscometric examination of cement pastes*, *Cement and Concrete Research* **11** (1981) 363–370.

[16] G. Etse, A. Carosio and R. Danesi, *Computational rate dependant localization analysis in concrete*, *SMiRT 13* (1995) .

[17] H. M. Mader, E. W. Llewellin and S. P. Mueller, *The rheology of two-phase magmas: A review and analysis*, *Journal of Volcanology and Geothermal Research* **257** (2013) 135–158.

[18] E. A. Evans, *Structure and deformation properties of red blood cells: Concepts and quantitative methods*, *Methods in enzymology* **173** (1989) 3–35.

[19] F. Gobeaux, E. Belamie, G. Mosser, P. Davidson and S. Asnacios, *Power law rheology and strain-induced yielding in acidic solutions of type i-collagen*, *Soft Matter* **6** (2010) 3769–3777.

[20] M. Czajkowski, D. M. Sussman, M. C. Marchetti and M. L. Manning, *Glassy dynamics in models of confluent tissue with mitosis and apoptosis*, *Soft Matter* **15** (2019) 9133–9149.

[21] D. Gonzalez-Rodriguez, K. Guevorkian, S. Douezan and F. Brochard-Wyart, *Soft matter models of developing tissues and tumors*, *Science* **338** (2012) 910–917.

[22] T. C. Polachini, R. C. Basso and J. Telis-Romero, *Rheology and fluid dynamic of egg white: Effect of thixotropy on engineering design*, *Journal of Food Process Engineering* **40** (2017) e12277.

[23] D. M. Hoyle and S. M. Fielding, *Age-dependent modes of extensional necking instability in soft glassy materials*, *Phys. Rev. Lett.* **114** (2015) .

[24] R. L. Moorcroft, M. E. Cates and S. M. Fielding, *Age-dependent transient shear banding in soft glasses*, *Phys. Rev. Lett.* **106** (2011) .

[25] S. M. Fielding, *Shear banding in soft glassy materials*, *Rep. Prog. Phys.* **77** (2014) .

[26] B. Keshavarz, T. Divoux, S. Manneville and G. H. McKinley, *Nonlinear viscoelasticity and generalized failure criterion for polymer gels*, *ACS Macro Lett.* **6** (2017) 663–667.

[27] B. Saint-Michel, T. Gibaud and S. Manneville, *Predicting and assessing rupture in protein gels under oscillatory shear*, *Soft Matter* **13** (2017) 2643–2653.

[28] T. Brenner, S. Matsukawa, K. Nishinari and R. Johannsson, *Failure in a soft gel: delayed failure and the dynamic yield stress*, *Journal of Non-Newtonian Fluid Mechanics* **196** (2013) 1–7.

[29] F. Grinnell and W. M. Petroll, *Cell motility and mechanics in three-dimensional collagen matrices*, *Annual Review of Cell and Developmental Biology* **26** (2010) 335–361.

[30] J. Viovy, *Electrophoresis of dna and other polyelectrolytes: Physical mechanisms*, *Rev. Mod. Phys.* **72** (2000) 813–872.

[31] T. Baumberger, C. Caroli and D. Martina, *Solvent control of crack dynamics in a reversible hydrogel*, *Nature Mater* **5** (2006) 552–555.

[32] R. Mezzenga, P. Schurtenberger and A. Burbidge, *Understanding foods as soft materials*, *Nature Mater* **4** (2005) 729–740.

[33] D. M. Teegarden, *Polymer chemistry: introduction to an indispensable science.* NSTA Press, 2004.

[34] P. Coussot, *Rheophysics of pastes: a review of microscopic modelling approaches*, *Soft Matter* **3** (2007) 528–540.

[35] M. Kogan, L. Ducloué, J. Goyon, X. Chateau, O. Pitois and G. Ovarlez, *Mixtures of foam and paste: suspensions of bubbles in yield stress fluids*, *Rheologica Acta* **52** (2013) 237–253.

[36] T. Divoux, C. Barentin and S. Manneville, *From stress-induced fluidization processes to Herschel-Bulkley behaviour in simple yield stress fluids*, *Soft Matter* **7** (2011) 8409–8418.

[37] F. Caton and C. Baravian, *Plastic behavior of some yield stress fluids: from creep to long-time yield*, *Rheologica Acta* **47** (2008) 601–607.

[38] T. Divoux, C. Barentin and S. Manneville, *Stress overshoot in a simple yield stress fluid: an extensive study combining rheology and velocimetry*, *Soft Matter* **7** (2011) 9335–9349.

[39] E. C. Bingham, *Fluidity and plasticity.* McGraw-Hill, 1922.

[40] W. H. Herschel and R. Bulkley, *Konsistenzmessungen von gummi-benzollösungen*, *Kolloid-Zeitschrift* **39** (1926) 291–300.

[41] R. Radhakrishnan and S. M. Fielding, *Shear banding of soft glassy materials in large amplitude oscillatory shear*, *Phys. Rev. Lett.* **117** (2016) 188001.

[42] T. Gibaud, C. Barentin and S. Manneville, *Influence of boundary conditions on yielding in a soft glassy material*, *Phys. Rev. Lett.* **101** (2008) 258302.

[43] R. Cabriolu, J. Horbach, P. Chaudhuri and K. Martens, *Precursors of fluidisation in the creep response of a soft glass*, *Soft Matter* **15** (2019) 415–423.

[44] V. E. Debets, X. M. D. Wit and L. M. C. Janssen, *Cage length controls the nonmonotonic dynamics of active glassy matter*, *Phys. Rev. Lett.* **127** (2021) 278002.

[45] Y. Jin, P. Urbani, F. Zamponi and H. Yoshino, *A stability-reversibility map unifies elasticity, plasticity, yielding, and jamming in hard sphere glasses*, *Science advances* **4** (2018) 6387.

[46] D. Fiocco, G. Foffi and S. Sastry, *Oscillatory athermal quasistatic deformation of a model glass*, *Phys. Rev. E* **88** (2013) 020301.

[47] A. L. Greer, Y. Q. Cheng and E. Ma, *Shear bands in metallic glasses*, *Materials Science and Engineering: R: Reports* **74** (2013) 71–132.

[48] J. P. Coleman, F. Meng, K. Tsuchiya, J. Beadsworth, M. LeBlanc, P. K. Liaw et al., *Effect of annealing on nanoindentation slips in a bulk metallic glass*, *Phys. Rev. B* **96** (2017) 134117.

[49] D. Pan, A. Inoue, T. Sakurai and M. W. Chen, *Experimental characterization of shear transformation zones for plastic flow of bulk metallic glasses*, *Proceedings of the National Academy of Sciences* **105** (2008) 14769–14772.

[50] P. Lidon, L. Villa and S. Manneville, *A mesoscale study of creep in a microgel using the acoustic radiation force*, *Soft Matter* **15** (2019) 2688–2702.

[51] P. Lidon, L. Villa and S. Manneville, *Power-law creep and residual stresses in a carbopol gel*, *Rheologica Acta* **56** (2017) 307–323.

[52] J. Sun, X. Zhao, W. R. K. Illeperuma, O. Chaudhuri, K. H. Oh, D. J. Mooney et al., *Highly stretchable and tough hydrogels*, *Nature* **489** (2012) 133–136.

[53] W. Helen, P. D. Leonardis, R. V. Ulijn, J. Gough and N. Tirelli, *Mechanosensitive peptide gelation: mode of agitation controls mechanical properties and nano-scale morphology*, *Soft Matter* **7** (2011) 1732–1740.

[54] T. Bai, P. Zhang, Y. Han, Y. Liu, W. Liu, X. Zhao et al., *Construction of an ultrahigh strength hydrogel with excellent fatigue resistance based on strong dipole–dipole interaction*, *Soft Matter* **7** (2011) 2825–2831.

[55] S. E. Bakarich, G. C. Pidcock, P. Balding, L. Stevens and P. Calvert, *Recovery from applied strain in interpenetrating polymer network hydrogels with ionic and covalent cross-links*, *Soft Matter* **8** (2012) 9985–9988.

[56] E. Moghimi, A. R. Jacob, N. Koumakis and G. Petekidis, *Colloidal gels tuned by oscillatory shear*, *Soft Matter* **13** (2017) 2371–2383.

[57] I. Sudreau, M. Auxois, M. Servel, E. Lécolier, S. Manneville and T. Divoux, *Residual stresses and shear-induced overaging in boehmite gels*, *Phys. Rev. Materials* **6** (2022) L042601.

[58] J. E. Verweij, F. A. M. Leermakers, J. Sprakel and J. V. D. Gucht, *Plasticity in colloidal gel strands*, *Soft Matter* **15** (2019) 6447–6454.

[59] S. Aime, L. Cipelletti and L. Ramos, *Power law viscoelasticity of a fractal colloidal gel*, *Journal of Rheology* **62** (2018) 1429–1441.

[60] R. A. L. Jones, *Soft Condensed Matter.* Oxford Univeristy Press, 2002.

[61] W. R. Schowalter, *Mechanics of non-Newtonian fluids.* Pergamon, 1978.

[62] P. Schall, D. A. Weitz and F. Spaepen, *Structural rearrangements that govern flow in colloidal glasses*, *Science* **318** (2007) 1895–1899.

[63] J. F. Ryder and J. M. Yeomans, *Shear thinning in dilute polymer solutions*, *Journal of chemical physics* **125** (2006) .

[64] R. G. Larson, *Constitutive equations for polymer melts and solutions: Butterworths series in chemical engineering.* Butterworth-Heinemann, 2013.

[65] P. E. Boukany and S. Wang, *Exploring origins of interfacial yielding and wall slip in entangled linear melts during shear or after shear cessation*, *Macromolecules* **42** (2009) 2222–2228.

[66] P. E. Boukany, S. Wang and X. Wang, *Step shear of entangled linear polymer melts: New experimental evidence for elastic yielding*, *Macromolecules* **42** (2009) 6261–6269.

[67] R. L. Moorcroft and S. M. Fielding, *Shear banding in time-dependent flows of polymers and wormlike micelles*, *Journal of Rheology* **58** (2014) 103–147.

[68] O. S. Agimelen and P. D. Olmsted, *Apparent fracture in polymeric fluids under step shear*, *Phys. Rev. Lett.* **110** (2013) 204503.

[69] J. M. Adams and P. D. Olmsted, *Nonmonotonic models are not necessary to obtain shear banding phenomena in entangled polymer solutions*, *Phys. Rev. Lett.* **102** (2009) 067801.

[70] J. O. Cochran, *Yielding transitions in amorphous materials*, Ph.D. thesis, Durham University, 2023.

[71] P. Sollich, *Rheological constitutive equation for a model of soft glassy materials*, *Phys. Rev. E* **58** (1998) .

[72] G. Brambilla, D. E. Masri, M. Pierno, L. Berthier, L. Cipelletti, G. Petekidis et al., *Probing the equilibrium dynamics of colloidal hard spheres above the mode-coupling glass transition*, *Phys. Rev. Lett.* **102** (2009) 085703.

[73] A. J. Liu and S. R. Nagel, *Jamming is not just cool any more*, *Nature* **396** (1998) 21–22.

[74] L. Ma and G. V. Barbosa-Cánovas, *Rheological characterization of mayonnaise. part ii: Flow and viscoelastic properties at different oil and xanthan gum concentrations*, *Journal of Food Engineering* **25** (1995) 409–425.

[75] G. A. V. Aken, *Aeration of emulsions by whipping*, *Colloids and Surfaces A: Physicochemical and Engineering Aspects* **190** (2001) 333–354.

[76] J. Mewis and N. J. Wagner, *Colloidal suspension rheology.* Cambridge university press, 2012.

[77] A. J. W. T. Brinke, L. Bailey, H. N. W. Lekkerkerker and G. C. Maitland, *Rheology modification in mixed shape colloidal dispersions. part i: pure components*, *Soft Matter* **3** (2007) 1145–1162.

[78] D. Kushnir, C. Ruscher, E. Bartsch, F. Thalmann and P. Hébraud, *Stress overshoot, hysteresis, and the bauschinger effect in sheared dense colloidal suspensions*, *Phys. Rev. E* **106** (2022) 034611.

[79] A. K. Bhattacharjee, *Stress–structure relation in dense colloidal melts under forward and instantaneous reversal of the shear*, *Soft Matter* **11** (2015) 5697–5704.

[80] N. Y. C. Lin, B. M. Guy, M. Hermes, C. Ness, J. Sun, W. C. K. Poon et al., *Hydrodynamic and contact contributions to continuous shear thickening in colloidal suspensions*, *Phys. Rev. Lett.* **115** (2015) 228304.

[81] S. M. Fielding, P. Sollich and M. E. Cates, *Aging and rheology in soft materials*, *Journal Of Rheology* **44** (2000) 323–369.

[82] J. P. Heller and M. S. Kuntamukkula, *Critical review of the foam rheology literature*, *Industrial and engineering chemistry research* **26** (1987) 318–325.

[83] C. Derec, G. Ducouret, A. Ajdari and F. Lequeux, *Aging and nonlinear rheology in suspensions of polyethylene oxide–protected silica particles*, *Phys. Rev. E* **67** (2003) 061403.

[84] P. D. Olmsted, *Perspectives on shear banding in complex fluids*, *Rheologica Acta* **47** (2008) 283–300.

[85] S. Manneville, *Recent experimental probes of shear banding*, *Rheologica Acta* **47** (2008) 301–318.

[86] T. Divoux, M. A. Fardin, S. Manneville and S. Lerouge, *Shear banding of complex fluids*, *Annual Review of Fluid Mechanics* **48** (2016) 81–103.

[87] R. L. Moorcroft and S. M. Fielding, *Criteria for shear banding in time-dependent flows of complex fluids*, *Phys. Rev. Lett.* **110** (2013) .

[88] V. V. Vasisht and E. D. Gado, *Computational study of transient shear banding in soft jammed solids*, *Phys. Rev. E* **102** (2020) 012603.

[89] G. Parisi, I. Procaccia, C. Rainone and M. Singh, *Shear bands as manifestation of a criticality in yielding amorphous solids*, *Proceedings of the National Academy of Sciences* **114** (2017) 5577–5582.

[90] Y. Nagas and K. Okada, *Heterogeneous behavior after yielding of solid suspensions*, *Journal of Rheology* **30** (1986) 1123–1142.

[91] H. A. Lockwood, M. P. Carrington and S. M. Fielding, *Long-term memory and delayed shear localisation in soft glassy materials*, *arXiv preprint arXiv:1907.05779* (2019) .

[92] P. Sollich, F. Lequeux, P. Hébraud and M. E. Cates, *Rheology of soft glassy materials*, *Phys. Rev. Lett.* **78** (1997) .

[93] M. Warren and J. Rottler, *Mechanical rejuvenation and overaging in the soft glassy rheology model*, *Phys. Rev. E* **78** (2008) 041502.

[94] D. Rodney, A. Tanguy and D. Vandembroucq, *Modeling the mechanics of amorphous solids at different length scale and time scale*, *Modelling and Simulation in Materials Science and Engineering* **19** (2011) 083001.

[95] G. Picard, A. Ajdari, F. Lequeux and L. Bocquet, *Slow flows of yield stress fluids: Complex spatiotemporal behavior within a simple elastoplastic model*, *Phys. Rev. E* **71** (2005) 010501.

[96] D. Fiocco, G. Foffi and S. Sastry, *Encoding of memory in sheared amorphous solids*, *Phys. Rev. Lett.* **112** (2014) 025702.

[97] E. E. Ferrero, K. Martens and J. Barrat, *Relaxation in yield stress systems through elastically interacting activated events*, *Phys. Rev. Lett.* **113** (2014) 248301.

[98] K. Chen, P. Bak and S. P. Obukhov, *Self-organized criticality in a crack-propagation model of earthquakes*, *Phys. Rev. A* **43** (1991) 625.

[99] J. Lin, A. Saade, E. Lerner, A. Rosso and M. Wyart, *On the density of shear transformations in amorphous solids*, *EPL (Europhysics Letters)* **105** (2014) 26003.

[100] K. Martens, L. Bocquet and J. Barrat, *Spontaneous formation of permanent shear bands in a mesoscopic model of flowing disordered matter*, *Soft Matter* **8** (2012) 4197–4205.

[101] A. Nicolas, K. Martens and J. Barrat, *Rheology of athermal amorphous solids: Revisiting simplified scenarios and the concept of mechanical noise temperature*, *EPL (Europhysics Letters)* **107** (2014) 44003.

[102] M. Popović, T. W. J. de Geus, W. Ji and M. Wyart, *Thermally activated flow in models of amorphous solids*, *Phys. Rev. E* **104** (2021) 025010.

[103] P. Hébraud and F. Lequeux, *Mode-coupling theory for the pasty rheology of soft glassy materials*, *Phys. Rev. Lett.* **81** (1998) 2934.

[104] V. V. Bulatov and A. S. Argon, *A stochastic model for continuum elasto-plastic behavior. i. numerical approach and strain localization*, *Modelling and Simulation in Materials Science and Engineering* **2** (1994) 167.

[105] C. Liu, S. Dutta, P. Chaudhuri and K. Martens, *Elastoplastic approach based on microscopic insights for the steady state and transient dynamics of sheared disordered solids*, *Phys. Rev. Lett.* **126** (2021) 138005.

[106] S. Pradhan, A. Hansen and B. K. Chakrabarti, *Failure processes in elastic fiber bundles*, *Rev. Mod. Phys.* **82** (2010) 499–555.

[107] K. Kovács, S. Nagy, R. C. Hidalgo, F. Kun, H. J. Herrmann and I. Pagonabarraga, *Critical ruptures in a bundle of slowly relaxing fibers*, *Phys. Rev. E* **77** (2008) 036102.

[108] E. A. Jagla, *Creep rupture of materials: Insights from a fiber bundle model with relaxation*, *Phys. Rev. E* **83** (2011) .

[109] Z. Halász, Z. Danku and F. Kun, *Competition of strength and stress disorder in creep rupture*, *Phys. Rev. E* **85** (2012) 016116.

[110] M. Leocmach, C. Perge, T. Divoux and S. Manneville, *Creep and fracture of a protein gel under stress*, *Phys. Rev. Lett.* **113** (2014) 038303.

[111] C. Liu, E. Ferrero, K. Martens and J. Barrat, *Creep dynamics of athermal amorphous materials: a mesoscopic approach*, *Soft Matter* **14** (2018) 8306–8316.

[112] S. Aime, L. Ramos and L. Cipelletti, *Microscopic dynamics and failure precursors of a gel under mechanical load*, *Proceedings of the National Academy of Sciences* **115** (2018) 3587–3592.

[113] D. F. Castellanos and M. Zaiser, *Statistical dynamics of early creep stages in disordered materials*, *Eur. Phys. J. B* **92** (2019) .

[114] H. Nechad, A. Helmstetter, R. E. Guerjouma and D. Sornette, *Creep ruptures in heterogeneous materials*, *Phys. Rev. Lett.* **94** (2005) 045501.

[115] L. Vanel, S. Ciliberto, P. Cortet and S. Santucci, *Time-dependent rupture and slow crack growth: elastic and viscoplastic dynamics*, *Journal of Physics D: Applied Physics* **42** (2009) 214007.

[116] S. Merabia and F. Detcheverry, *Thermally activated creep and fluidization in flowing disordered materials*, *EPL (Europhysics Letters)* **116** (2016) 46003.

[117] D. F. Castellanos and M. Zaiser, *Avalanche behavior in creep failure of disordered materials*, *Phys. Rev. Lett.* **121** (2018) .

[118] S. Touati, M. Naylor and I. G. Main, *Origin and nonuniversality of the earthquake interevent time distribution*, *Phys. Rev. Lett.* **102** (2009) 168501.

[119] E. G. Daub, M. L. Manning and J. M. Carlson, *Pulse-like, crack-like, and supershear earthquake ruptures with shear strain localization*, *Journal of Geophysical Research: Solid Earth* **115** (2010) .

[120] C. D. Munialo, S. R. Euston and H. H. J. de Jongh, *19 - protein gels*, in *Proteins in Food Processing (Second Edition)* (Y. Y. Rickey, ed.), Woodhead Publishing Series in Food Science, Technology and Nutrition, pp. 501–521. Woodhead Publishing, 2nd ed., 2018.

[121] A. M. Janssen, T. V. Vliet and J. M. Vereijken, *Fundamental and empirical rheological behaviour of wheat flour doughs and comparison with bread making performance*, *Journal of Cereal Science* **23** (1996) 43–54.

[122] A. H. Bloksma, *Slow creep of wheat flour doughs*, *Rheologica Acta* **2** (1962) 217–230.

[123] R. Cerbino and V. Trappe, *Introduction to viscoelasticity and plasticity, and their relation to the underlying microscopic dynamics in soft matter systems*, *Physica A: Statistical Mechanics and its Applications* (2023) 128653.

[124] W. C. Tang, H. Z. Cui and M. Wu, *Creep and creep recovery properties of polystyrene aggregate concrete*, *Construction and Building Materials* **51** (2014) 338–343.

[125] T. C. Brito-Oliveira, I. C. F. Moraes, S. C. Pinho and O. H. Campanella, *Modeling creep/recovery behavior of cold-set gels using different approaches*, *Food Hydrocolloids* **123** (2022) 107183.

[126] P. K. Singh, J. C. Lee, K. A. Patankar and S. A. Rogers, *Revisiting the basis of transient rheological material functions: Insights from recoverable strain measurements*, *Journal of Rheology* **65** (2021) 129–144.

[127] X. Zhao, *Multi-scale multi-mechanism design of tough hydrogels: building dissipation into stretchy networks*, *Soft Matter* **10** (2014) 672–687.

[128] J. Sablić, M. Praprotnik and R. Delgado-Buscalioni, *Open boundary molecular dynamics of sheared star-polymer melts*, *Soft Matter* **12** (2016) 2416–2439.

[129] K. Kamani, G. J. Donley and S. A. Rogers, *Unification of the rheological physics of yield stress fluids*, *Phys. Rev. Lett.* **126** (2021) 218002.

[130] M. Zhong, Y. Liu, X. Liu, F. Shi, L. Zhang, M. Zhu et al., *Dually cross-linked single network poly (acrylic acid) hydrogels with superior mechanical properties and water absorbency*, *Soft Matter* **12** (2016) 5420–5428.

[131] J. Hou, X. Ren, S. Guan, L. Duan, G. H. Gao, Y. Kuai et al., *Rapidly recoverable, anti-fatigue, super-tough double-network hydrogels reinforced by macromolecular microspheres*, *Soft Matter* **13** (2017) 1357–1363.

[132] A. M. Ortega, C. M. Yakacki, S. A. Dixon, R. Likos, A. R. Greenberg and K. Gall, *Effect of crosslinking and long-term storage on the shape-memory behavior of (meth) acrylate-based shape-memory polymers*, *Soft Matter* **8** (2012) 7381–7392.

[133] R. Hoeher, T. Raidt, M. Rose, F. Katzenberg and J. C. Tiller, *Recoverable strain storage capacity of shape memory polyethylene*, *Journal of Polymer Science Part B: Polymer Physics* **51** (2013) 1033–1040.

[134] K. Gall, M. L. Dunn, Y. Liu, D. Finch, M. Lake and N. A. Munshi, *Shape memory polymer nanocomposites*, *Acta Materialia* **50** (2002) 5115–5126.

[135] R. Abishera, R. Velmurugan and N. K. V. Gopal, *Reversible plasticity shape memory effect in carbon nanotubes reinforced epoxy nanocomposites*, *Composites Science and Technology* **137** (2016) 148–158.

[136] T. Lin, Z. Tang and B. Guo, *New design strategy for reversible plasticity shape memory polymers with deformable glassy aggregates*, *ACS Applied Materials & Interfaces* **6** (2014) 21060–21068.

[137] X. Zhang, Z. Tang and B. Guo, *Reversible plasticity shape memory polymers: key factors and applications*, *Journal of Polymer Science Part B: Polymer Physics* **54** (2016) 1295–1299.

[138] J. Yin, J. Hu, Y. Han, Y. Chen, J. Hu, Z. Zhang et al., *Facile fabrication of high nanofiller-content natural rubber nanocomposites for reversible plasticity shape memory polymers*, *Composites Science and Technology* **221** (2022) 109349.

[139] C. C. Hornat and M. W. Urban, *Shape memory effects in self-healing polymers*, *Progress in Polymer Science* **102** (2020) 101208.

[140] H. M. Laun and H. Münstedt, *Elongational behaviour of a low density polyethylene melt: I. strain rate and stress dependence of viscosity and*

recoverable strain in the steady-state. comparison with shear data. influence of interfacial tension, *Rheologica Acta* **17** (1978) 415–425.

[141] H. Münstedt, *Rheological measurements and structural analysis of polymeric materials*, *Polymers* **13** (2021) 1123.

[142] K. Gall, C. M. Yakacki, Y. Liu, R. Shandas, N. Willett and K. S. Anseth, *Thermomechanics of the shape memory effect in polymers for biomedical applications*, *Journal of Biomedical Materials Research Part A: An Official Journal of The Society for Biomaterials* **73** (2005) 339–348.

[143] G. J. Donley, P. K. Singh, A. Shetty and S. A. Rogers, *Elucidating the G" overshoot in soft materials with a yield transition via a time-resolved experimental strain decomposition*, *Proceedings of the National Academy of Sciences* **117** (2020) 21945–21952.

[144] J. C. Lee, K. M. Weigandt, E. G. Kelley and S. A. Rogers, *Structure-property relationships via recovery rheology in viscoelastic materials*, *Phys. Rev. Lett.* **122** (2019) 248003.

[145] E. Demir and D. Raabe, *Mechanical and microstructural single-crystal bauschinger effects: Observation of reversible plasticity in copper during bending*, *Acta Materialia* **58** (2010) 6055–6063.

[146] J. Wang, Z. Chen, X. Li, M. Liu, Y. Zhu and L. Jiang, *Plastic-like hydrogels with reversible conversion of elasticity and plasticity and tunable mechanical properties*, *ACS Applied Materials & Interfaces* **11** (2019) 41659–41667.

[147] L. K. Galloway, D. J. Jerolmack and P. E. Arratia, *Quantification of plasticity via particle dynamics above and below yield in a 2d jammed suspension*, *Soft Matter* **16** (2020) 4373–4382.

[148] A. Elgailani, D. Vandembroucq and C. Maloney, *Anomalous softness in amorphous matter in the reversible plastic regime*, *arXiv preprint arXiv:2212.10472* (2022) .

[149] M. Lundberg, K. Krishan, N. Xu, C. S. O'Hern and M. Dennin, *Reversible plastic events in amorphous materials*, *Phys. Rev. E* **77** (2008) 041505.

[150] N. C. Keim and P. E. Arratia, *Mechanical and microscopic properties of the reversible plastic regime in a 2d jammed material*, *Phys. Rev. Lett.* **112** (2014) 028302.

[151] C. Lei, Q. Li, L. Yang, F. Deng, J. Li, Z. Ye et al., *Controlled reversible buckling of polydopamine spherical microcapsules: revealing the hidden rich phenomena of post-buckling of spherical polymeric shells*, *Soft Matter* **15** (2019) 6504–6517.

[152] M. Leocmach, C. Perge, T. Divoux and S. Manneville, *Creep and fracture of a protein gel under stress: supplemental material*, .

[153] A. P. Tabatabai, D. L. Kaplan and D. L. Blair, *Rheology of reconstituted silk fibroin protein gels: the epitome of extreme mechanics*, *Soft Matter* **11** (2015) 756–761.

[154] J. Lubliner, *Plasticity theory.* Courier Corporation, 2008.

[155] W. Chen and D. Han, *Plasticity for structural engineers.* J. Ross publishing, 2007.

[156] R. C. Hibbeler, *Mechanics of materials.* MacMillan Publishing Company, 1994.

[157] V. Grenard, T. Divoux, N. Taberlet and S. Manneville, *Timescales in creep and yielding of attractive gels*, *Soft Matter* **10** (2014) 1555–1571.

[158] L. Cipelletti, K. Martens and L. Ramos, *Microscopic precursors of failure in soft matter*, *Soft Matter* **16** (2020) 82–93.

[159] F. Rouyer, S. H. R. Cohen-Addad, P. Sollich and S. M. Fielding, *The large amplitude oscillatory strain response of aqueous foam: Strain localization and full stress fourier spectrum*, *Eur. Phys. J. E* **27** (2008) 309–321.

[160] J. Pollard and S. M. Fielding, *Yielding, shear banding, and brittle failure of amorphous materials*, *Phys. Rev. Research* **4** (2022) 043037.

[161] H. J. Barlow, J. O. Cochran and S. M. Fielding, *Ductile and brittle yielding in thermal and athermal amorphous materials*, *Phys. Rev. Lett.* **125** (2020) 168003.

[162] H. A. Barnes, J. F. Hutton and K. Walters, *An introduction to rheology*, vol. 3. Elsevier, 1989.

[163] G. Böhme, *Non-Newtonian fluid mechanics*. Elsevier, 2012.

[164] E. J. Hemingway, A. Clarke, J. R. A. Pearson and S. M. Fielding, *Thickening of viscoelastic flow in a model porous medium*, *Journal of Non-Newtonian Fluid Mechanics* **251** (2018) 56–68.

[165] J. Ding, P. J. Tracey, W. Li, G. Peng, P. G. Whitten and G. G. Wallace, *Review on shear thickening fluids and applications*, *Textiles and Light Industrial Science and Technology* (2013) 161–173.

[166] T. Tian, M. Nakano and W. Li, *Applications of shear thickening fluids: a review*, *International Journal of Hydromechatronics* **1** (2018) 238–257.

[167] D. Bonn and M. M. Denn, *Yield stress fluids slowly yield to analysis*, *Science* **324** (2009) 1401–1402.

[168] M. M. Denn and D. Bonn, *Issues in the flow of yield-stress liquids*, *Rheologica Acta* **50** (2011) 307–315.

[169] P. B. Macedo and A. Napolitano, *Effects of a distribution of volume relaxation times in the annealing of bsc glass*, *Journal of Research of the National Bureau of Standards. Section A, Physics and Chemistry* **71** (1967) 231.

[170] G. Kumar, P. Neibecker, Y. H. Liu and J. Schroers, *Critical fictive temperature for plasticity in metallic glasses*, *Nature Communications* **4** (2013) 1536.

[171] M. Ozawa, L. Berthier, G. Biroli, A. Rosso and G. Tarjus, *Random critical point separates brittle and ductile yielding transitions in amorphous materials*, *Proceedings of the National Academy of Sciences* **115** (2018) 6656–6661.

[172] R. Radhakrishnan, T. Divoux, S. Manneville and S. M. Fielding, *Understanding rheological hysteresis in soft glassy materials*, *Soft Matter* **13** (2017) 1834–1852.

[173] S. Kamble, A. Pandey, S. Rastogi and A. Lele, *Ascertaining universal features of yielding of soft materials*, *Rheologica Acta* **52** (2013) 859–865.

[174] J. Bouchaud, *Weak ergodicity breaking and aging in disordered systems*, *Journal de Physique I* **2** (1992) 1705–1713.

[175] C. Monthus and J. Bouchaud, *Models of traps and glass phenomenology*, *Journal of Physics A: Mathematical and General* **29** (1996) 3847.

[176] H. Barlow, *Theory and Simulation of Shear Flow Instabilities in Complex Fluids*, Ph.D. thesis, Durham University, 2020.

[177] J. Lin, E. Lerner, A. Rosso and M. Wyart, *Scaling description of the yielding transition in soft amorphous solids at zero temperature*, *Proceedings of the National Academy of Sciences* **111** (2014) 14382–14387.

[178] P. Sollich and M. E. Cates, *Thermodynamic interpretation of soft glassy rheology models*, *Phys. Rev. E* **85** (2012) 031127.

[179] G. E. P. Box and M. E. Muller, *A Note on the Generation of Random Normal Deviates*, *The Annals of Mathematical Statistics* **29** (1958) 610–611.

[180] A. D. Fokker, *Die mittlere energie rotierender elektrischer dipole im strahlungsfeld*, *Annalen der Physik* **348** (1914) 810–820.

[181] M. Planck, *Über einen satz der statistischen dynamik und seine erweiterung in der quantentheorie, sitz*, *Preuschen AkaD. Wissen* **24** (1917) 324–341.

[182] J. M. van Doorn, J. E. Verweij, J. Sprakel and J. van der Gucht, *Strand plasticity governs fatigue in colloidal gels*, *Phys. Rev. Lett.* **120** (2018) 208005.

[183] T. van Vliet and P. Walstra, *Large deformation and fracture behaviour of gels*, *Faraday Discuss.* **101** (1995) 359–370.

[184] M. Pouzot, T. Nicolai, L. Benyahia and D. Durand, *Strain hardening and fracture of heat-set fractal globular protein gels*, *Journal of Colloid and Interface Science* **293** (2006) 376–383.

[185] V. C. Barroso and J. M. Maia, *Evaluation by means of stress relaxation (after a step strain) experiments of the viscoelastic behavior of polymer melts in uniaxial extension*, *Rheologica Acta* **41** (2002) 257–264.

[186] Y. Einaga, K. Osaki, M. Kurata, S. Kimura, N. Yamada and M. Tamura, *Stress relaxation of polymer solutions under large strain*, *Polymer Journal* **5** (1973) 91–96.

[187] Y. Fang, G. Wang, N. Tian, X. Wang, X. Zhu, P. Lin et al., *Shear inhomogeneity in poly (ethylene oxide) melts*, *Journal of Rheology* **55** (2011) 939–949.

[188] H. A. Lockwood, E. S. Carrington and S. M. Fielding, *Ultra-delayed material failure via shear banding after straining an amorphous material*, *arXiv preprint arXiv:2305.02144* (2023) .

[189] F. C. Monkman and N. J. Grant, *An empirical relationship between rupture life and minimum creep rate in creep-rupture tests*, in *Proc of the ASTM*, vol. 56, pp. 593–620, 1956.

[190] H. Liu, W. Zeiada, G. G. Al-Khateeb, A. Shanableh and M. Samarai, *Use of the multiple stress creep recovery (MSCR) test to characterize the rutting*

potential of asphalt binders: A literature review, *Construction and Building Materials* **269** (2021) 121320.

[191] T. L. J. Wasage, J. Stastna and L. Zanzotto, *Rheological analysis of multi-stress creep recovery (MSCR) test*, *International Journal of Pavement Engineering* **12** (2011) 561–568.

[192] O. Radulescu and P. D. Olmsted, *Matched asymptotic solutions for the steady banded flow of the diffusive johnson–segalman model in various geometries*, *Journal of Non-Newtonian Fluid Mechanics* **91** (2000) 143–164.

[193] D. C. Lu, P. D. Olmsted and R. C. Ball, *Effects of nonlocal stress on the determination of shear banding flow*, *Phys. Rev. Lett.* **84** (2000) 642.

[194] N. A. Spenley, X. F. Yuan and M. E. Cates, *Nonmonotonic constitutive laws and the formation of shear-banded flows*, *Journal de Physique II* **6** (1996) 551–571.

[195] A. B. Bortz, M. H. Kalos and J. L. Lebowitz, *A new algorithm for monte carlo simulation of ising spin systems*, *Journal Of Computational Physics* **17** (1975) 10–18.

[196] J. C. Spall, *Introduction to stochastic search and optimization: estimation, simulation, and control.* John Wiley & Sons, 2005.

[197] S. A. Baeurle, *Multiscale modeling of polymer materials using field-theoretic methodologies: a survey about recent developments*, *Journal of Mathematical Chemistry* **46** (2009) 363–426.

[198] X. Jia, P. Ziegenhein and S. B. Jiang, *GPU-based high-performance computing for radiation therapy*, *Physics in Medicine & Biology* **59** (2014) 151.

[199] E. Agoritsas, E. Bertin and K. Martens, *On the relevance of disorder in athermal amorphous materials under shear*, *Eur. Phys. J. E* **38** (2015) .

[200] S. Deschanel, L. Vanel, N. Godin, E. Maire, G. Vigier and S. Ciliberto, *Mechanical response and fracture dynamics of polymeric foams*, *Journal of Physics D: Applied Physics* **42** (2009) 214001.

[201] P. Leishangthem, A. D. S. Parmar and S. Sastry, *The yielding transition in amorphous solids under oscillatory shear deformation*, *Nature Communications* **8** (2017) 14653.

[202] Y. Shi and M. L. Falk, *Strain localization and percolation of stable structure in amorphous solids*, *Phys. Rev. Lett.* **95** (2005) 095502.

[203] M. Popović, T. W. J. de Geus and M. Wyart, *Elastoplastic description of sudden failure in athermal amorphous materials during quasistatic loading*, *Phys. Rev. E* **98** (2018) 040901.

[204] P. A. Stark, *Introduction to Numerical Methods.* Macmillan Publishing Co, New York, 1970.

[205] M. L. Gardel, J. H. Shin, F. C. MacKintosh, L. Mahadevan, P. Matsudaira and D. A. Weitz, *Elastic behavior of cross-linked and bundled actin networks*, *Science* **304** (2004) 1301–1305.

[206] S. Aime, L. Ramos, J. Fromental, G. Prevot, R. Jelinek and L. Cipelletti, *A stress-controlled shear cell for small-angle light scattering and microscopy*, *Review of Scientific Instruments* **87** (2016) .

[207] A. Amon, A. Mikhailovskaya and J. Crassous, *Spatially resolved measurements of micro-deformations in granular materials using diffusing wave spectroscopy*, *Review of Scientific Instruments* **88** (2017) .

[208] T. L. Anderson, *Fracture mechanics: fundamentals and applications.* CRC press, 2017.

[209] B. Saint-Michel, T. Gibaud, M. Leocmach and S. Manneville, *Local oscillatory rheology from echography*, *Phys. Rev. Applied* **5** (2016) 034014.

[210] M. Korhonen, K. Wallgren, A. Puisto, M. Alava and V. Vuorinen, *Shear localization in large amplitude oscillatory shear (LAOS) flows of particulate suspensions*, *Phys. Rev. Fluids* **6** (2021) 033302.

[211] R. Radhakrishnan and S. M. Fielding, *Shear banding in large amplitude oscillatory shear (LAOStrain and LAOStress) of soft glassy materials*, *Journal of Rheology* **62** (2018) 559–576.

[212] J. O. Cochran, G. L. Callaghan and S. M. Fielding, *Slow fatigue and highly delayed yielding via shear banding in oscillatory shear*, *arXiv preprint arXiv:2211.11677* (2022) .

[213] L. Zhou, P. A. Vasquez, P. L. Cook and G. H. McKinley, *Modeling the inhomogeneous response and formation of shear bands in steady and transient flows of entangled liquids*, *Journal of Rheology* **52** (2008) 591–623.

[214] A. Aufderhorst-Roberts, S. Cussons, D. J. Brockwell and L. Dougan, *Power law rheology of folded protein hydrogels*, *arXiv preprint arXiv:2207.13348* (2022) .

[215] J. Rault, *Ageing of glass: role of the Vogel–Fulcher–Tamman law*, *Journal of Physics: Condensed Matter* **15** (2003) S1193.

[216] N. Metatla and A. Soldera, *The Vogel-Fulcher-Tamman equation investigated by atomistic simulation with regard to the Adam-Gibbs model*, *Macromolecules* **40** (2007) 9680–9685.

[217] H. Lu and W. M. Huang, *On the origin of the Vogel–Fulcher–Tammann law in the thermo-responsive shape memory effect of amorphous polymers*, *Smart Materials and Structures* **22** (2013) 105021.

[218] D. R. Reichman and P. Charbonneau, *Mode-coupling theory*, *Journal of Statistical Mechanics: Theory and Experiment* **2005** (2005) P05013.

[219] C. Ness, Z. Xing and E. Eiser, *Oscillatory rheology of dense, athermal suspensions of nearly hard spheres below the jamming point*, *Soft Matter* **13** (2017) 3664–3674.

[220] D. Vågberg, P. Olsson and S. Teitel, *Shear banding, discontinuous shear thickening, and rheological phase transitions in athermally sheared frictionless disks*, *Phys. Rev. E* **95** (2017) 052903.

[221] J. R. Royer, D. L. Blair and S. D. Hudson, *Rheological signature of frictional interactions in shear thickening suspensions*, *Phys. Rev. Lett.* **116** (2016) 188301.

[222] L. Boltzmann, *Studien uber das gleichgewicht der lebenden kraft*, *Wissenschafiliche Abhandlungen* **1** (1868) 49–96.

[223] E. Bouchbinder, J. S. Langer and I. Procaccia, *Athermal shear-transformation-zone theory of amorphous plastic deformation. i. basic principles*, *Phys. Rev. E* **75** (2007) 036107.

[224] M. L. Falk and C. E. Maloney, *Simulating the mechanical response of amorphous solids using atomistic methods*, *Eur. Phys. J. B* **75** (2010) 405–413.

[225] H. A. Lockwood, M. Agar and S. M. Fielding, *Power law creep and delayed failure of gels and fibrous materials under stress*, *arXiv preprint arXiv:2311.16778* (2023) .

[226] R. Benzi, T. Divoux, C. Barentin, S. Manneville, M. Sbragaglia and F. Toschi, *Unified theoretical and experimental view on transient shear banding*, *Phys. Rev. Lett.* **123** (2019) 248001.

[227] F. Kun, Z. Halász, J. S. Andrade and H. J. Herrmann, *Crackling noise in sub-critical fracture of heterogeneous materials*, *Journal of Statistical Mechanics: Theory and Experiment* (2009) P01021.

[228] F. Kun, H. A. Carmona, J. S. Andrade and H. J. Herrmann, *Universality behind basquin's law of fatigue*, *Phys. Rev. Lett.* **100** (2008) 094301.

[229] J. Sprakel, S. B. Lindström, T. E. Kodger and D. A. Weitz, *Stress enhancement in the delayed yielding of colloidal gels*, *Phys. Rev. Lett.* **106** (2011) 248303.

[230] J. Bauschinger, *Über die veränderung der elasticitätsgrenze und des elasticitätsmodulus verschiedener metalle, civilingenieur*, *NF* **27** (1881) 289–348.

[231] R. Sowerby, D. K. Uko and Y. Tomita, *A review of certain aspects of the bauschinger effect in metals*, *Materials Science and Engineering* **41** (1979) 43–58.

[232] G. E. Dieter and D. Bacon, *Mechanical metallurgy*, vol. 3. McGraw-hill New York, 1976.

[233] S. Deboeuf, L. Ducloué, N. Lenoir and G. Ovarlez, *A mechanism of strain hardening and bauschinger effect: shear-history-dependent microstructure of elasto-plastic suspensions*, *Soft Matter* **18** (2022) 8756–8770.

[234] A. Y. Liu and J. Rottler, *Aging under stress in polymer glasses*, *Soft Matter* **6** (2010) 4858–4862.

[235] S. Patinet, A. Barbot, M. Lerbinger, D. Vandembroucq and A. Lemaître, *Origin of the bauschinger effect in amorphous solids*, *Phys. Rev. Lett.* **124** (2020) 205503.

[236] P. Zhu, J. Lin, R. Xiao and H. Zhou, *Unravelling physical origin of the bauschinger effect in glassy polymers*, *Journal of the Mechanics and Physics of Solids* **168** (2022) 105046.

[237] M. K. Sing, Z. Wang, G. H. McKinley and B. D. Olsen, *Celebrating soft matter's 10th anniversary: Chain configuration and rate-dependent mechanical properties in transient networks*, *Soft Matter* **11** (2015) 2085–2096.

[238] B. Florijn, C. Coulais and M. van Hecke, *Programmable mechanical metamaterials: the role of geometry*, *Soft Matter* **12** (2016) 8736–8743.

[239] M. Dietrich, H. L. Roy, D. B. Brückner, H. Engelke, R. Zantln, J. O. Rädler et al., *Guiding 3d cell migration in deformed synthetic hydrogel microstructures*, *Soft Matter* **14** (2018) 2816–2826.

[240] K. A. Murphy, J. W. Kruppe and H. M. Jaeger, *Memory in nonmonotonic stress relaxation of a granular system*, *Phys. Rev. Lett.* **124** (2020) 168002.